

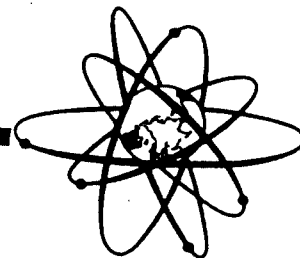
OECD
NEA

COMPARISON REPORT OF
THE OECD/CSNI INTERNATIONAL STANDARD PROBLEM 21
(PIPER-ONE EXPERIMENT PO-SB-7)

Volume 2

EVALUATION OF CODE ACCURACY
IN THE PREDICTION OF ISP 21

November 1989



UNIVERSITA' DEGLI STUDI DI PISA

DIPARTIMENTO DI COSTRUZIONI

MECCANICHE E NUCLEARI

EVALUATION OF CODE ACCURACY IN THE
PREDICTION OF OECD/CSNI ISP 21
PERFORMED IN PIPER-ONE APPARATUS

W. Ambrosini

R. Bovalini

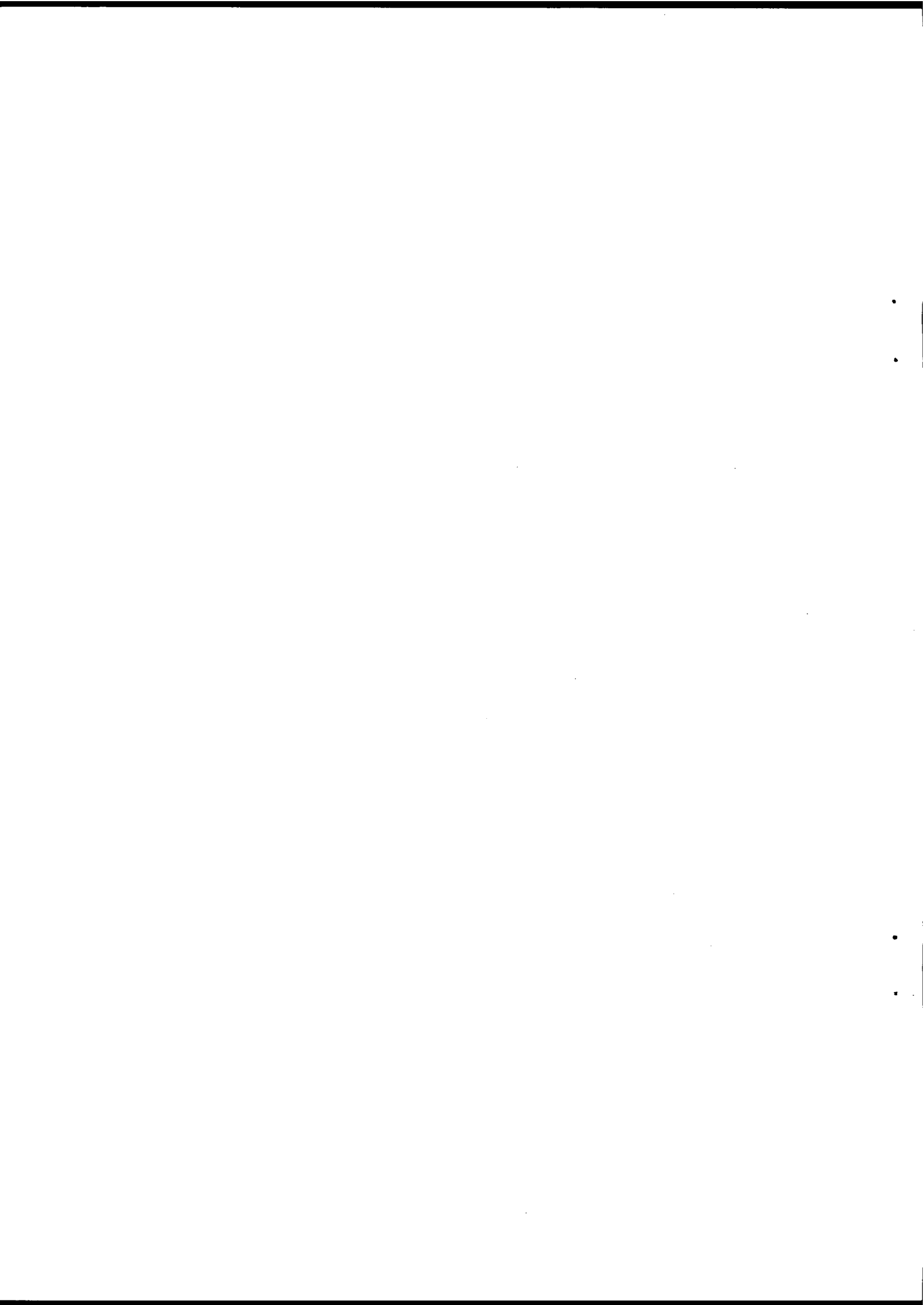
F. D'Auria

RL 389(89)

OECD/CSNI Final Workshop on ISP 21

Pisa (I), April 13-14, 1989

Work performed within the framework of the
ENEA safety research programme.



ABSTRACT

The present report shows the results of the application to ISP 21 calculations of a method developed at DCMN for the quantification of the accuracy of code predictions.

The main features of the method are described. The method is qualified through the application to relevant sample problems.

Finally, the considerations outcoming from the analysis of ISP 21 calculations are used to draw preliminary conclusions on the suitability of the method.

List of Figures

- Fig. 1 - Sample Problem 1 : considered experimental and calculated curves
- Fig. 2 - Sample Problem 2 : considered experimental and calculated curves
- Fig. 3 - Sample Problem 2 : amplitude of FFT of the experimental signal
- Fig. 4 - Sample Problem 2 : amplitude of FFT for calculated trends
- Fig. 5 - Sample Problem 2 : results for AA as a function of $1/WF$
- Fig. 6 - LOBI A2-81 (ISP 18): results for IL HL density
- Fig. 7 - LOBI A2-81 (ISP 18): results for PS mass inventory
- Fig. 8 - Sketch of PIPER-ONE Facility
- Fig. 9 - Test PO-SB-7 : System pressure and sequence of events
- Fig. 10 - Test PO-SB-7 : Rod temperature (level G)
- Fig. 11 - Double blind calculations : results for variable PA01
- Fig. 12 - Double blind calculations : results for variable TF03
- Fig. 13 - Double blind calculations : results for variable TF17
- Fig. 14 - Double blind calculations : results for variable CL70
- Fig. 15 - Double blind calculations : results for variable MF43
- Fig. 16 - Double blind calculations : results for variable MF48
- Fig. 17 - Double blind calculations : results for variable TR50
- Fig. 18 - Double blind calculations : results for variable TR52
- Fig. 19 - Double blind calculations : results for variable TR55
- Fig. 20 - Double blind calculations : results for variable RM65
- Fig. 21 - Double blind calculations : overall results
- Fig. 22 - Comparison between double blind and DCMN post-test calculations : variable PA01
- Fig. 23 - Comparison between double blind and DCMN post-test calculations : variable TF03
- Fig. 24 - Comparison between double blind and DCMN post-test calculations : variable TF17
- Fig. 25 - Comparison between double blind and DCMN post-test calculations : variable CL70
- Fig. 26 - Comparison between double blind and DCMN post-test calculations : variable MF43

- Fig. 27 - Comparison between double blind and DCMN post-test calculations : variable MF48
- Fig. 28 - Comparison between double blind and DCMN post-test calculations : variable TR50
- Fig. 29 - Comparison between double blind and DCMN post-test calculations : variable TR52
- Fig. 30 - Comparison between double blind and DCMN post-test calculations : variable TR55
- Fig. 31 - Comparison between double blind and DCMN post-test calculations : variable RM65
- Fig. 32 - Comparison between double blind and DCMN post-test calculations : overall results

List of Tables

- **Tab. 1 - List of participants and adopted codes for ISP 21 double blind calculations**
- **Tab. 2 - Results for double blind and DCMN post test calculations**

Nomenclature

Roman letters

A	Area [m^2]
AA	Average Amplitude
$D(t)$	function quantifying accuracy (eq. 2)
$E(t)$	function used to define $D(t)$ (eq. 3)
f	frequency [Hz]
F	variable
$g(t)$	function of time
m	integer constant
n	integer constant
N	integer constant
p	pressure [Pa]
t	time [s]
T	transient duration [s]
WF	Weighted Frequency
w_i	weighting factor

Greek letters

Δ	difference
$\Delta E(t)$	function defined in eq. 1

Subscripts

calc	calculated
------	------------

exp	experimental
m	used to identify the "figure of merit" in eq. 4
max	maximum
min	minimum
tot	total
var	variable

Commonly used symbols

$\hat{\cdot}$	Fourier Transform
$ \cdot $	amplitude of a complex number

Abbreviations

ABB	Asea Brown Boveri
BWR	Boiling Water Reactor
CBRV	Calculation Behaviour Reference Value
CRTN	Centro Ricerche Termiche e Nucleari
CSNI	Committee on the Safety of Nuclear Installations
DCMN	Dipartimento di Costruzioni Meccaniche e Nucleari
ECCS	Emergency Core Cooling System
ENEL	Ente Nazionale per l'Energia Elettrica
FFT	Fast Fourier Transform
HL	Hot Leg
ICAP	International Code Assessment Program
IL	Intact Loop
ISP	International Standard Problem
JAERI	Japan Atomic Energy Research Institute

<i>LOCA</i>	Loss Of Coolant Accident
<i>OECD</i>	Organization for Economic Cooperation and Development
<i>MSIV</i>	Main Steam Isolation Valve
<i>NPP</i>	Nuclear Power Plant
<i>PC</i>	Personal Computer
<i>PCT</i>	Peak Cladding Temperature
<i>PS</i>	Primary System
<i>SB – LOCA</i>	Small Break LOCA
<i>SRV</i>	Safety Relief Valve
<i>VTT</i>	Valtion Teknillinen Tutkimuskeskus

Table of Contents

1. INTRODUCTION	1
2. PREVIOUSLY DEVELOPED METHODS FOR THE QUANTIFICATION OF CODES ACCURACY ...	3
3. DESCRIPTION OF THE ADOPTED METHOD	6
3.1 Method development	6
3.2 Method qualification	9
4. APPLICATION TO PO-SB-7 ISP 21	11
4.1 Test description	11
4.2 Variables selected for the analysis	12
4.3 Application to blind calculations	13
4.4 Application to the DCMN post-test calculation	17
5. CONCLUSIONS	19
REFERENCES	21
Tables and Figures	23
APPENDIX A - Figures concerning double blind calculations	43
APPENDIX B - Figures concerning DCMN post-test calculation	64

1. INTRODUCTION

The reliability of the predictions obtained by thermalhydraulic system codes, adopted for safety analyses of Nuclear Power Plants (NPP), is the result of many factors involving code features and user experience. The most important items are the number and the type of balance equations, the constitutive models, the numerical method, the characteristics of the nodalization developed to describe a complex geometrical system.

The main objective of the code qualification process, including the developmental assessment and the application to tests performed in separate effects and integral facilities, is the definition of the acceptability of the code itself. This requires the solution of two main problems :

- the first one concerns the evaluation of the "accuracy" of a code in the prediction of the scenario of tests performed in scaled facilities;
- the second is related to the definition of the "uncertainty" in the evaluation of the behaviour of the full scale NPP.

The reactors are characterized by geometrical dimensions much larger than those of the experimental facilities; limited information is available from measurements in NPP. So, scaling problems must be solved in going from accuracy to uncertainty.

Large efforts are in progress in the international framework in order to develop objective criteria to be used in the code qualification process (CSNI, ICAP, national activities). Difficulties occur in this context, even due to the lack of an accepted approach to the problem, mainly concerning the following aspects :

1. the uncertainties present in the experimental measurements of physical quantities taken as reference for code calculations;
2. the effect of the user experience in the selection of code options and in the development of nodalizations for complex facilities;

3. the need of engineering judgement in the definition of variables to be considered of great importance for safety of NPP, i.e. to be calculated by codes;
4. the lack of an objective basis to extrapolate phenomena measured or foreseen considering small scale facilities in order to achieve information about full scale plants.

The present work is concerned with the evaluation of the accuracy of the blind calculations of the PO-SB-7 test /1/, performed at the University of Pisa on the PIPER-ONE experimental apparatus and selected as CSNI International Standard Problem 21 (ISP 21) /2/. The study has been performed adopting a method, developed at DCMN and previously applied to ISP 18 calculations /3/, which is claimed to have some capabilities in quantifying the errors in code predictions with respect to the measured experimental signal. The method uses the Fast Fourier Transform in order to have an integral representation of code discrepancies in the frequency domain.

The objective of the present document is to describe the above methodology and to present the main conclusions obtained in the application to ISP 21 calculations.

2. PREVIOUSLY DEVELOPED METHODS FOR THE QUANTIFICATION OF CODES ACCURACY

In the period 1985-1986 several proposals were presented at CSNI aiming at the quantification of code accuracy and uncertainty. References /3-6/ report some of the proposed techniques, that are briefly described hereafter.

The integral approach suggested by Pochard and Porracchia /6/ is based on the definition of an "error function" defined by

$$\Delta E(t) = \frac{1}{\Delta t} \int_{t_0}^{t_0 + \Delta t} |F_{calc} - F_{exp}| dt \quad (1)$$

in which t is the time, Δt is the selected time interval and F_{calc} and F_{exp} are the calculated and the experimental values of the addressed variable F

Although the proposed error function gives an integral representation of the behaviour of a code in the calculation of a variable, it seems that the definition adopted is too conservative because of the absolute value. This limitation can lead to misleading information, especially in the case of oscillating functions. Moreover, engineering skill is required in fixing Δt .

In the attempt to overcome these problems, a new error function was proposed at DCMN /3/ on the basis of the relationship :

$$D(t) = \frac{E(t)}{F_{exp}(t)} \quad (2)$$

where

$$E(t) = \frac{1}{t} \int_0^t (F_{calc} - F_{exp}) dt \quad (3)$$

The instantaneous values of $D(t)$ give an idea of the percentage error of the calculation; maximum and minimum values can be used to quantify the accuracy of the code in the calculation of the addressed variable. Besides, by defining the value :

$$D_m = \max\{|D_{max}|, |D_{min}|\} \quad (4)$$

for each considered variable, it is possible to obtain an unique value characterizing the code calculation (Calculation Behaviour Reference Value, CBRV), defined by the following relationship :

$$CBRV = \frac{1}{N_{var}} \sum_{j=1}^{N_{var}} (D_m)_j \quad (5)$$

It can be noted that the use of the new error function $D(t)$ is restricted to variables which do not assume the zero value; therefore, a number of interesting variables, e.g. flowrates and levels, cannot be dealt with by this approach.

Both the methodologies were applied to some sample problems and to selected blind calculations of ISP 18 (LOBI A2-81) /3-4/. The two approaches were not considered completely satisfactory. In particular, the definition of the $D(t)$ appears not to have a rigorous mathematical basis and has no absolute value in order to judge code performance.

Further attempts were performed to give a more sound basis to the definition of the error function. These attempts involved :

- the study and the application of other two error functions based on the relationships :

$$D_1(t) = \frac{E(t)}{\frac{1}{t} \int_0^t F_{exp} dt} \quad (5)$$

$$D_p^*(t) = \left[\frac{\int_0^t |F_{calc} - F_{exp}|^p dt}{\int_0^t |F_{exp}|^p dt} \right]^{1/p} \quad (6)$$

in which $E(t)$ is defined by eq. (3) and $p = 1, 2, 3, 4$;

- the adoption of some techniques used in assessing air pollution models /7-9/.

These activities led to improvements in the evaluation of accuracy /3/. Notwithstanding this, the used procedures still involved empiricism and were judged not completely satisfactory. Therefore,

a new approach has been studied. Its most important features are described in the following section.

3. DESCRIPTION OF THE ADOPTED METHOD

3.1 Method development

The need was felt for a more complete representation of the discrepancies between the experimental and the calculated trends. In principle, the original information about the accuracy of a given calculation is obtained by the curve of the difference

$$\Delta F(t) = F_{calc}(t) - F_{exp}(t) \quad (7)$$

In the definition of one or more "figures of merit" giving a synthesis of this instantaneous information, it is necessary not to lose interesting details, in order to avoid misleading conclusions. The ideal definition should be capable of identifying uniquely a given difference curve allowing, as far as possible, to distinguish it from all different trends. Of course, it is very difficult to find a procedure satisfying this requirement, especially when searching for functions expressing all the information through a single value; therefore, it is worthful to consider procedures leading to more than one value to characterize the code calculation.

In this respect, integral formulations as those outlined in the previous section preserve only part of the information required to properly compare experimental and calculated trends. As an example, there are several possible curves giving a same values of D_m .

Trying to overcome these problems, the suitability of the Fourier analysis for the definition of one or more values characterizing the accuracy of code calculations was investigated. It is well known that the Fourier Transform can translate a given function of time, $g(t)$, in a corresponding complex function defined, in the frequency domain, by the relationship :

$$\tilde{g}(f) = \int_{-\infty}^{+\infty} g(t) e^{-i2\pi ft} dt \quad (8)$$

In the following, it is assumed that the experimental and calculated trends to which the Fourier Transform is applied satisfy the analytical conditions required by this application; i.e., it is assumed that they are continuous in the considered time intervals (or discontinuous only in a finite number

of points) with their first derivatives and their absolute value can be integrated in the interval $(-\infty, +\infty)$. This last requirement, can be easily fulfilled in our case, since the addressed functions assume values different from zero only in intervals $(0, T)$. Therefore

$$\tilde{g}(f) = \int_0^T g(t) e^{-i2\pi ft} dt \quad (9)$$

When using functions sampled in digital form, the Fast Fourier Transform (FFT) can be used. The FFT is an algorithm which allows a fast evaluation of Fourier Transform of functions identified in digital form by a number of values which is a power of 2. Thus, if the number of points defining the function in the time domain is

$$N = 2^{m+1} \quad (10)$$

the algorithm gives the transformed function defined in the frequency domain by $2^m + 1$ values corresponding to the frequencies

$$f_n = \frac{n}{T} \quad (n = 0, \dots, 2^m) \quad (11)$$

in which T is the time duration of the sampled signal.

Taking into account that the adopted subroutine packages evaluate the FFT normalized to the time duration T , from eqs. (9) and (11) it can be easily seen that $|\tilde{g}(0)|$ represents the mean value of the function $g(t)$ in the interval $(0, T)$; $|\tilde{g}(f_n)|$ represents the amplitude of the n -th term of the Fourier polynomial expansion for the function $g(t)$.

The method developed to quantify the accuracy of code calculations is based on the amplitude of the FFT of the experimental signal and of the difference between the experimental signal and the calculated trend. In particular, the method defines two values which are characteristic of every calculation :

- a dimensionless average amplitude

$$AA = \frac{\sum_{n=0}^{2^m} |\tilde{\Delta F}(f_n)|}{\sum_{n=0}^{2^m} |\tilde{F}_{\text{exp}}(f_n)|} \quad (12)$$

- a weighted frequency

$$WF = \frac{\sum_{n=0}^{2^m} |\tilde{\Delta F}(f_n)| \cdot f_n}{\sum_{n=0}^{2^m} |\tilde{\Delta F}(f_n)|} \quad (13)$$

The average amplitude, represents a sort of "average fractional error" of the addressed calculation, while the weighted frequency gives an idea of the frequencies which give the greatest contribution to the inaccuracy.

The two obtained values can be used to evaluate the accuracy of a code calculation by representing the discrepancies with respect to the experimental data through a point in the AA-WF plane. Of course, the most interesting information is given by AA, which represents the relative magnitude of these discrepancies; WF adds a further information allowing to better identify the character of accuracy. As an example, oscillations of the calculated values around an average trend can be readily identified by the method. Moreover, this information could be used, in principle, in the quantification of accuracy. In fact, depending on the transient and on the variable considered, low frequency errors can be more important than high frequency ones, or vice versa. Acceptability curves could be traced.

Although some criticism can be raised about the above definitions, especially because the use of AA and WF involves the loss of some information concerning the calculated values (e.g., the phase spectrum of $\tilde{\Delta F}$ plays no role in the present formulations), it can be recognized that the new approach constitutes an improvement with respect to previously developed techniques.

3.2 Method qualification

The curves shown in Fig. 1 have been used to assess the capabilities of the adopted method. The experimental signal is a constant while two possible calculated curves are considered. The first one (Curve 1) is a constant with a value different from the experimental one; in this case the average amplitude, AA , is equal to the ratio between the absolute value of the difference on the experimental value. Curve 2 has a sinoidal shape, the amplitude of the oscillation being equal to the difference between Curve 1 and the experimental value; it can be verified that AA has in this case the same value as for Curve 1.

Despite of this, the two cases are characterized by a different value of WF . In fact, for Curve 1 is $WF = 0$, while for Curve 2 it is $WF = 1/T$. This demonstrates that the selected method allows to distinguish between discrepancies of the same magnitude at different frequencies.

More realistic sample curves to which the selected procedure has been applied are presented in Fig. 2. These curves may represent virtual calculated and experimental trends of cladding temperature during a transient in which core dry-out occurs. It can be noted that Calc. 1 has a substantial agreement with the sample experimental curve, although systematic oscillations are present. Calc. 2 and Calc. 3 depict qualitatively well the heat up of the rod surface, but show some problems in predicting the real temperature values or the timing of dry-out and quenching. Calculations 4 and 5 behave similarly, showing greater discrepancies with respect to the experimental curve. Calc. 6 is characterized by the absence of any dry-out phenomenon and presents a typical trend with a constant temperature decrease.

Figs. 3 and 4 show the amplitude of the FFT of the sample experimental signal and of the difference between the experimental and the six calculated curves. In particular, in Fig. 4 it can be noted that Calc. 1-3 and Calc. 6 present similar amplitude spectra, mainly characterized by low frequency components, while Calculations 4 and 5 have greater amplitudes in the high frequency region.

The results of the application of the developed method are reported in Fig. 5. Qualitative acceptability curves were also drawn assuming that high frequency discrepancies can be considered

more acceptable than low frequency ones. In this connection it should be noted that for some variables it may be preferable to have a good mean value throughout the transient tolerating some instantaneous deviations (e.g., it can be so for thermal flux from structures); in other cases, high frequency discrepancies could point out an abnormal behaviour of the code (e.g., instabilities of the calculation).

Therefore, in the application of the method to real calculations it is advisable to take the average amplitude, *AA*, as the real quantitative index defining the accuracy, leaving to the weighted frequency, *WF*, the role of an additional qualitative information. The possibility to give a better definite role to *WF* is still matter of study.

The present method was applied to some ISP 18 calculations /3/. The results of this applications are shown in Figs. 6-7 concerning IL HL density and PS mass inventory. It can be seen that among the considered calculations the best results were obtained by the RELAP4/MOD6 code for both quantities. These results are in good agreement with qualitative considerations which can be drawn from the observation of the corresponding curves.

4. APPLICATION TO PO-SB-7 ISP 21

4.1 Test description

The PIPER-ONE apparatus (Fig. 8) is a roughly 1/2000 volumetrically scaled simulator of the Caorso BWR 4 plant. The similarity in vessel dimensions makes it possible to refer the PIPER-ONE facility to a BWR 6 plant on a slightly different volume scale. The heights of the various zones, which determine natural circulation inside the vessel and then the system response to a SB-LOCA, are fully reproduced.

PIPER-ONE mainly consists of a primary loop and of a series of circuits with different interfaces with the main one. The one-dimensionality as well as the overall simplicity of the system are evident characteristics. Nine zones can be identified in the primary loop : lower plenum, core, core bypass, upper plenum, region of separators and dryers, upper downcomer, lower downcomer and jet pumps region.

An indirectly heated bundle, reproducing 1/4 of the BWR fuel element, is installed inside the core. The available power is 250 KW, enough to simulate the nuclear fuel decay curve.

Almost 250 measurement points are provided including thermocouples, differential and absolute pressure transducers, turbines, a γ -densitometer, distributed thermoresistances. A digital data acquisition system is provided and the automatic control of the facility is achieved by means of a PC.

PIPER-ONE test PO-SB-7 /1/ is the counterpart of the tests ROSA 984 and FIST 6SB2C performed, respectively, in the ROSA-III (Japan) and the FIST (USA) facilities, both representing General Electric BWR 6 plants /10/. The experiment simulates a typical SB-LOCA sequence in BWR plants.

The experiment is originated by a break in one of the two recirculation lines of the BWR. The break area is equal to 2.6% of the recirculation line cross section of the reference BWR 6; if related to a BWR 4, the same break area corresponds to 1.6% of A_{max} due to the larger recirculation lines in this plant.

The sequence of occurring events is depicted in Fig. 9, in which it can be seen that the test scenario is characterized by three main phases. During the first period, the vessel pressure is maintained nearly constant by the operation of MSIV and SRV. The low fluid mass inventory in the core simulator is the main cause of a dry-out occurring in the highest part of the heating rods (Fig.10).

The second phase of the transient begins with the ADS intervention, 120. s after the achievement of the specified set-point for liquid level in the downcomer. This period is characterized by a fast depressurization of the system and by an increased rate of coolant loss. The consequent core flashing causes the quenching or stops this dry-out, but a new dry-out situation occurs in the upper part of the rods; the lower plenum flashing quenches completely the rods. The corresponding PCT is 660 °K and is reached in the highest rod location.

Phase three is started by the intervention of ECCS which refills the core. During this phase the heat release from the structures leads to a small increase in the system pressure at about 400.s. The ECCS water brings, finally, to the recovery of total mass inventory.

4.2 Variables selected for the analysis

The experimental variables identified for the quantification of the accuracy of codes calculations are listed below :

- Variable PA01 : lower plenum pressure;
- Variable TF03 : lower plenum temperature;
- Variable TF17 : steam dome temperature;
- Variable CL70 : collapsed liquid level in the downcomer;¹
- Variable MF43 : break mass flow rate;
- Variable MF48 : LPCS mass flow rate;

¹ This experimental variable was compared with the calculated values for CL23.

- Variable TR50 : rod temperature (level B);
- Variable TR52 : rod temperature (level D);
- Variable TR55 : rod temperature (level G);
- Variable RM65 : fluid mass in the loop.

The choice of these variables has been made in the aim to identify the most representative quantities characterizing the transient. In particular :

- the lower plenum pressure (PA01) is representative of the overall energy balance in the loop;
- the fluid temperatures (TF03 and TF17) are representative of the fluid conditions in two different parts of the apparatus;
- the collapsed liquid level in the downcomer (CL23 or CL70), the break mass flow rate (MF43), the LPCS mass flow rate (MF48) and the residual mass in the whole loop (RM65) are representative of the overall mass balance and distribution in the apparatus;
- the rod temperatures distribution (TR50, TR52 and TR55) has the greatest interest in safety analysis, being the parameter defining the safe or unsafe conditions along the whole accidental transient.

4.3 Application to blind calculations

Six code calculations of ISP 21 were submitted to DCMN before the specified deadline; they were performed by five different organizations, adopting five different codes (Tab. 1).

An outline of the code models and of the adopted nodalizations for PIPER-ONE apparatus is given in ref. /2/. Here, it is only recalled that the two calculations by VTT differ only because of the heat transfer options of the SMABRE code.

Since the six calculations have different durations, the analysis was restricted to the time period common to all of them (see Tab.1). Therefore, a time duration of 350. s was selected as common basis for the comparison.

The application of the method described in the previous sections, required the linear interpolation of the submitted calculated values in order to have a set of 1024 points equally spaced in time to be processed by the FFT algorithm. Although the application of the FFT to this set of values gives amplitude spectra for frequencies ranging up to 1.4 Hz , a "cut frequency" of 1. Hz was considered in the definition of AA and WF, since the original sampling period was 1. s.

For each considered variable, Appendix A reports the curves of the experimental and the calculated trends, of the differences $\Delta F = F_{calc} - F_{exp}$ and the amplitude spectra of the FFT of the experimental signal and of the differences.

Figs. 11-20 summarize the results obtained by the described approach in terms of AA as a function of $1/WF$. The main observations drawn from these figures are presented below.

a) Variable PA01 : lower plenum pressure

The obtained values of AA range from 0.084 for the ABB calculation to about 0.266 of the two VTT ones. The spread in the weighted frequencies is limited, the greatest values being achieved by the JAERI curve. The two calculations by ABB and ANSALDO give the best pressure trends.

b) Variable TF03 : lower plenum temperature

In this case higher values of AA are present. Still, the ABB calculation gives the best trend; a good trend is shown also by JAERI. All the other calculations show larger discrepancies.

c) Variable TF17 : steam dome temperature

In this case the two VTT calculations present the best agreement with the data, while the other codes give large discrepancies. As it is explained in the Comparison Report /2/, this is probably due to the fact that all the participants submitted only liquid temperatures, while in this case the thermocouples indicate the presence of superheated steam. Then, the overprediction of liquid

temperature by the VTT calculations result in a better agreement with experimental thermocouple measurements. Noticeable differences between the values of the weighted frequency of the two VTT calculations and of the other participants point out different trends of the corresponding difference curves (see Appendix A).

d) Variable CL70 : collapsed liquid level in the downcomer

A large spread in the averaged amplitude is present for this variable. A value greater than 1 for AA is calculated for the ENEL-CRTN curve, while the other participants gave better results. The best collapsed level trend is calculated by ANSALDO.

e) Variable MF43 : break mass flow rate

The values of the average amplitude calculated for this variable belong to the range (0.6 – 0.8). The lowest ones are given by ANSALDO and JAERI, the highest by VTT and ENEL.

f) Variable MF48 : LPCS mass flow rate

The majority of participants predict fairly well this variable, the best calculation being obtained by ENEL. Large discrepancies with the experiment are present in the calculations by VTT.

g) Variables TR50, TR52 and TR55: rod temperatures (levels B, D, G)

For these variables the lowest values of AA are calculated for ABB, ANSALDO and JAERI, while the other calculations show far higher discrepancies. Differences appear in the weighted frequencies.²

h) Variable RM65 : fluid mass in the loop

Also in this case the best calculations are those by ABB, ANSALDO and JAERI, the lowest value of AA being given by the ABB residual mass curve.

Fig. 21 summarizes the results obtained giving average values of AA and WF for the ten considered variables. In principle, these average values should be defined on the basis of a set of weighting factors representing the relevance for safety of each variable, using formulations like those reported below:

$$(AA)_{tot} = \sum_{j=1}^{N_{var}} (AA)_j \cdot (w_j) \quad (14)$$

$$(WF)_{tot} = \sum_{j=1}^{N_{var}} (WF)_j \cdot (w_j) \quad (15)$$

in which N_{var} is the number of considered variables, while the weighting factors w_j satisfy the obvious condition

$$\sum_{j=1}^{N_{var}} (w_j) = 1 \quad (16)$$

² It has to be noted that the experimental trends for these variables comprise initial time intervals of not significant values. This situation was neglected in the present analysis since the width of these intervals is very small (less than 20. s) compared with the whole transient duration.

The definition of the weighting factors involves at present the use of engineering judgement, because no objective procedure is available for this purpose. Therefore, in the present application it was decided to put $(w_i)_j = 1/10$ ($j = 1, \dots, 10$) giving the same weight to each variable.

From Fig. 21 it can be noted that the present quantitative evaluation of accuracy agrees with the conclusions reached in the Comparison Report /2/ on the basis of qualitative observation of the submitted curves. In particular, two groups of calculations can be identified in Fig. 21 : the first group comprises calculations obtained by a second generation code (RELAP5/MOD2) and codes specifically developed for safety analysis of BWR plants (GOBLIN-EM and THYDE-B1/MOD2); the second group consists of calculations obtained by a first generation code (RELAP4/MOD6) and a code developed with main reference to PWR plants analysis (SMABRE).

4.4 Application to the DCMN post-test calculation

Figs. 22-31 show the comparison between the values obtained for *AA* and *WF* in the application of the method to the double blind calculations and the corresponding values concerning the post-test analysis of ISP 21 performed at DCMN using the RELAP5/MOD2 code /11/.

Several calculations have been performed at DCMN in order to obtain the best agreement with experimental data. The main parameters which have been "tuned" in order to achieve this objective were the pressure loss coefficients and the break flow rate multipliers.

As it was expected, in all cases the values of *AA* determined for the DCMN calculation are smaller than for the other calculations, except for variable TF17. In particular, very low values of the average amplitude are calculated for pressure in the lower plenum (PA01) and residual mass (RM65), showing considerable improvements in the overall energy and mass balances with respect to pre-test calculations.

Similar improvements were obtained for rod temperatures (Variables TR50, TR52 and TR55). In this connection it has to be noted also that the temperature values considered for the post-test calculation were calculated in the exact location of thermocouples, which is internal to the rod body, while participants submitted only rod surface temperatures.

Fig. 32 and Tab. 2 summarize the results obtained by pre-test and post-test calculations, quantifying this improvement in the description of the overall transient.

5. CONCLUSIONS

In this work a method developed at DCMN in order to quantify the accuracy of code calculations has been applied to ISP 21 pre-test and post-test analyses. The results obtained gave objective indications about the behaviour of the addressed codes in the prediction of the main variables characterizing the first 350 s of the transient.

The procedure adopted, based on the Fast Fourier Transform, can be considered an improvement with respect to previously proposed approaches and is suitable to quantify the discrepancies existing between an experimental trend and calculated ones. In particular, unlike the previous integral techniques, the method appears to include in the final "figure of merit" a great part of the original information concerning discrepancies in the time domain.

In particular, the average amplitude defined by the method, AA , makes it possible to quantify the existing discrepancies between the experimental and the calculated trends, while the weighted frequency, WF , gives an additional qualitative parameter which can be used to judge the acceptability of the calculation.

Possible improvements of the presented method may concern :

- the use of frequency information; in fact, in the application of the method the need was felt for a better definite role of the weighted frequency, WF , in the quantification of accuracy;
- the development of a procedure taking into account the information represented by the phase spectrum of the FFT in the evaluation of code accuracy;
- the development of an objective procedure in order to identify the experimental variables to be considered in the quantification of accuracy and to define the weighting factors for the calculation of $(AA)_{tot}$ and $(WF)_{tot}$.

Despite of this, reliable information could be drawn by its application to pre-test and post-test analyses of ISP 21. Concerning pre-test calculations, the obtained results have shown to be in agreement with the conclusions reached in the Comparison Report by qualitative observations.

The application of the method to the post-test calculation performed at DCMN by RELAP5/MOD2 code shows the quantitative improvements which can be obtained by the "tuning" of relevant parameters.

The present method constitutes a new approach for the solution of the problems related to the quantification of codes accuracy. However, in depth studies are needed to achieve more powerful techniques in order to solve this fundamental safety issue.

REFERENCES

1. R.Bovalini, F. D'Auria, L. Giannini, M. Mazzini, P. Vigni "PIPER-ONE Research: Experimental Data Report of Test PO-SB-7 (2.6% break at DC bottom)", Universita' degli Studi di Pisa, DCMN RL 381(89), OECD/CSNI Final Workshop on ISP 21, Pisa, April 13-14, 1989
2. F. D'Auria, M. Mazzini, S. Paci, F. Oriolo "Comparison Report of OECD/CSNI International Standard Problem 21 (PIPER-ONE Experiment PO-SB-7)" Universita' degli Studi di Pisa, OECD/CSNI Final Workshop on ISP 21, Pisa, April 13-14, 1989
3. W. Ambrosini, R. Bovalini, F. D'Auria, P. Petrini "Advancements in Evaluating the Accuracy of Thermalhydraulic Codes Calculations", Meeting of the CSNI PWG-2 Task Group on the Status and Assessment of Codes for Transients and ECCS, Paris, June 1-3 1987
4. F. D'Auria, P. Petrini "Quantification of uncertainties in thermalhydraulic codes calculation", SACTE Task Group Meeting, Dec. 15-17, 1986, Paris
5. W. Riebold "Minutes of the CSNI SACTE Task Group Meeting of Dec. 15-17 1986", SEN/SIN (87) 13, Paris, 1987
6. R. Pochard, A. Porracchia "Assessment closure proposals", SACTE Task Group Meeting, Dec. 16-18 1985, Paris
7. C.J. Willmott "Some comments on the evaluation of model performance" Bull.Am.Metl.Soc. 63, 1309-1303, 1982
8. Jia-Yeong Ku, S.T. Rao, K.S. Rao "Numerical simulation of air pollution in urban areas: model performance", Atmospheric Environment 21, 213-232, 1987
9. T.W. Tesche, J.L. Haney, R.E. Morris "Performance evaluation of four grid-based dispersion models in complex terrain", Atmospheric Environment 21, 233-256, 1987
10. R.Bovalini, F. D'Auria, A. De Varti, P. Maugeri, M. Mazzini "Analysis of Counterpart Tests Performed in BWR Experimental Simulators", Universita' degli Studi di Pisa, DCMN RL 387(89), OECD/CSNI Final Workshop on ISP 21, Pisa, April 13-14, 1989

11. F. D'Auria, G. Fruttuoso "OECD/CSNI ISP 21, PIPER-ONE Test PO-SB-7: Post Test Analysis performed at Pisa University by RELAP5/MOD2 Code", Università degli Studi di Pisa, RL 386 (89), OECD/CSNI Final Workshop on ISP 21, Pisa, April 13-14, 1989

Tables and Figures

ORGANIZATION	ADOPTED CODE	TRANSIENT DURATION (s)
ASEA Brown Boveri (Sweden)	GOBLIN-EM	395.
ANSALDO (Italy)	RELAP5/MOD2	409.
ENEL-CRTN (Italy)	RELAP4/MOD6	600.
JAERI (Japan)	THYDE-B1/MOD2	359.6
VTT (Finland)	SMABRE (1)	898.
VTT (Finland)	SMABRE (2)	898.

Tab. 1 - List of participants and adopted codes for ISP 21 double blind calculations

W. FACT.	ABB	ANSALDO	ENEL	JAERI	VTTI	VTT2	DCMN PT
PA01	0.1000000D+01	0.6276971D-01	0.7123344D-01	0.5328340D-01	0.8061045D-01	0.8091211D-01	0.9421590D-01
		0.1091256D+00	0.1964301D+00	0.1490956D+00	0.2656756D+00	0.2661751D+00	0.3760800D-01
TF03	0.1000000D+01	0.1488172D+00	0.1300668D+00	0.1397521D+00	0.1367035D+00	0.1367661D+00	0.1591113D+00
		0.3821255D+00	0.4803367D+00	0.1446455D+00	0.3137098D+00	0.3148677D+00	0.7681714D-01
TF17	0.1000000D+01	0.1386989D+00	0.1479294D+00	0.1503887D+00	0.4024657D-01	0.4200505D-01	0.1557500D+00
		0.6259462D+00	0.6185949D+00	0.4437697D+00	0.1491488D+00	0.1496208D+00	0.3922347D+00
CL70	0.1000000D+01	0.1309870D+00	0.1403638D+00	0.8389895D-01	0.6307282D-01	0.6307604D-01	0.1708251D+00
		0.1076190D+00	0.1102471D+01	0.1939774D+00	0.2533511D+00	0.2533277D+00	0.7698164D-01
MF43	0.1000000D+01	0.1150771D+00	0.1244622D+00	0.1086374D+00	0.1164044D+00	0.1164029D+00	0.1474490D+00
		0.5877414D+00	0.7723447D+00	0.6671047D+00	0.7896157D+00	0.7896082D+00	0.5339250D+00
MF48	0.1000000D+01	0.1329332D+00	0.1182990D+00	0.6509069D-01	0.1215906D+00	0.1218493D+00	0.1404001D+00
		0.3513778D+00	0.2740903D+00	0.4322201D+00	0.8757740D+00	0.8802166D+00	0.1063865D+00
TR50	0.1000000D+01	0.6142193D-01	0.9369920D-01	0.1078478D+00	0.1102778D+00	0.1102876D+00	0.6879784D-01
		0.8480531D-01	0.3319286D+00	0.1024547D+00	0.2865956D+00	0.2875309D+00	0.6628932D-01
TR52	0.1000000D+01	0.1263902D+00	0.6048147D-01	0.8664738D-01	0.1109290D+00	0.1070975D+00	0.1131158D+00
		0.1325810D+00	0.6252527D+00	0.1672991D+00	0.1575233D+01	0.1473269D+01	0.1166813D+00
TR55	0.1000000D+01	0.8730582D-01	0.6184969D-01	0.7713020D-01	0.9544307D-01	0.8731748D-01	0.7688842D-01
		0.4554510D+00	0.7401395D+00	0.4849668D+00	0.1105890D+01	0.1037988D+01	0.3139871D+00
RM65	0.1000000D+01	0.1571730D+00	0.1572950D+00	0.1502551D+00	0.1620627D+00	0.1621453D+00	0.1018500D+00
		0.2815366D+00	0.6004845D+00	0.2848888D+00	0.6464538D+00	0.6471037D+00	0.2927307D-01
MFTOT	0.1154131D+00	0.1163778D+00	0.1105680D+00	0.1022932D+00	0.1037341D+00	0.1027859D+00	0.1228403D+00
AATOT	0.2890390D+00	0.3118369D+00	0.5742073D+00	0.3070422D+00	0.6261447D+00	0.6099708D+00	0.1750184D+00

Tab. 2 - Results for double blind and DCMN post-test calculations

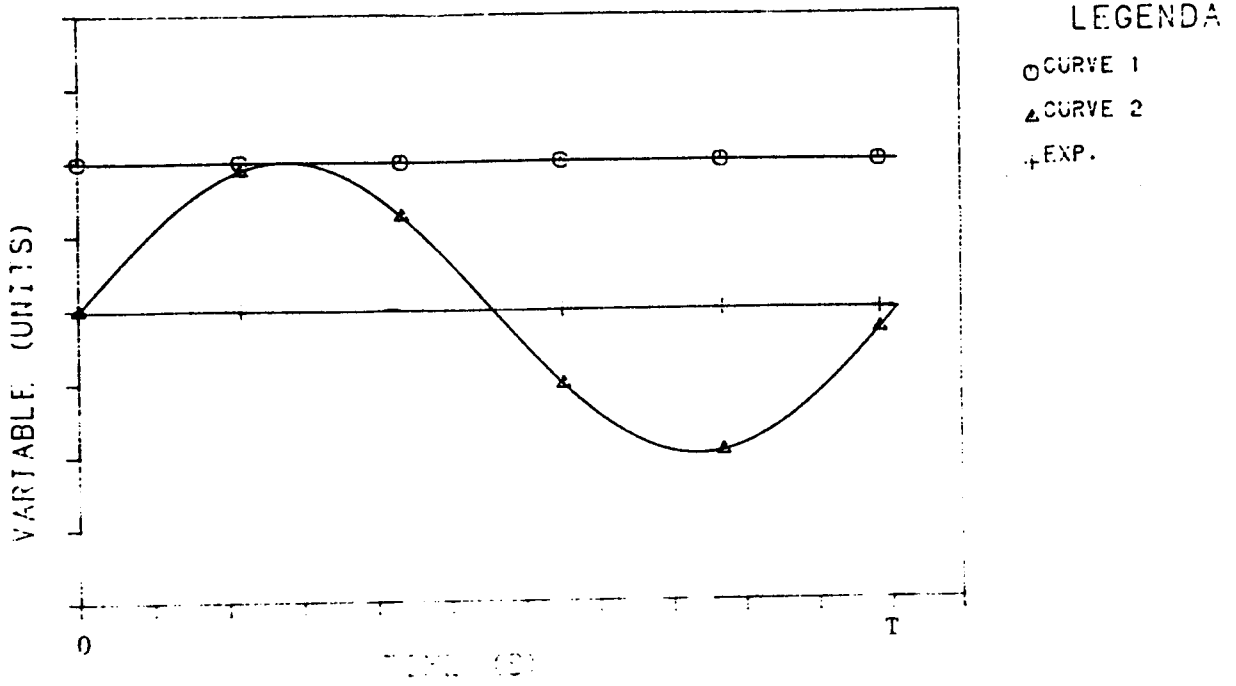


Fig. 1 - Sample Problem 1 : considered experimental and calculated curves

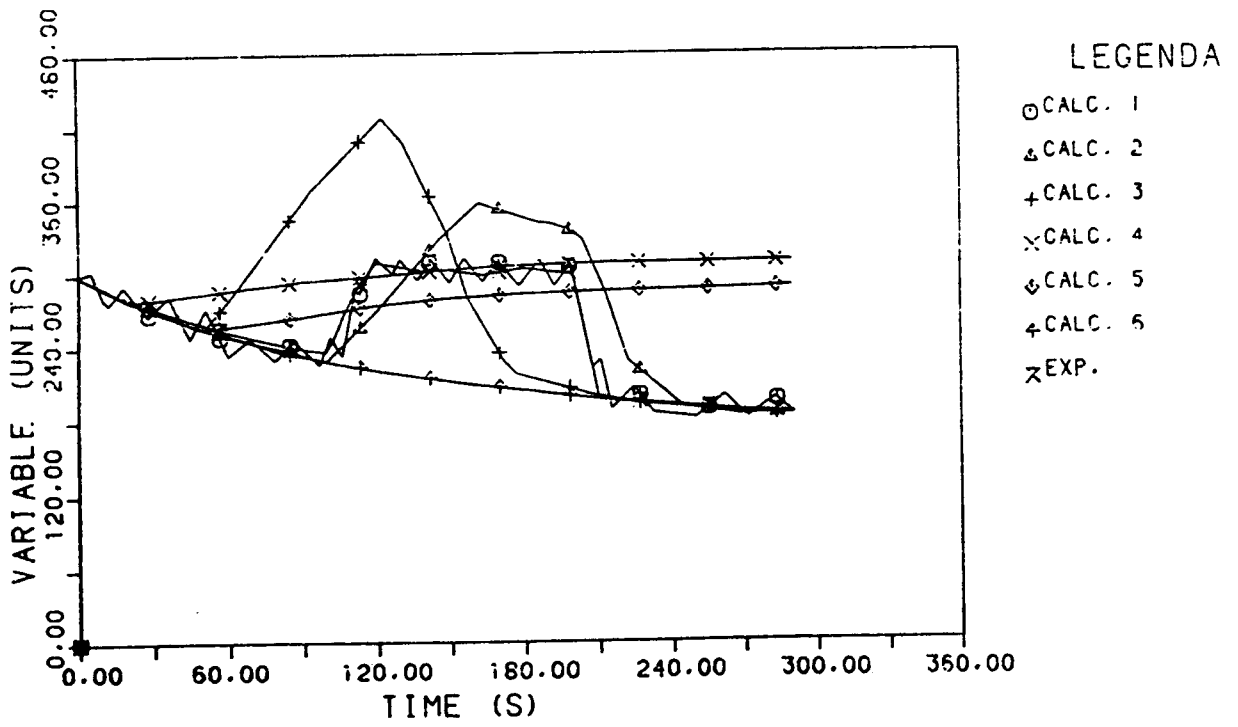


Fig. 2 - Sample Problem 2 : considered experimental and calculated curves

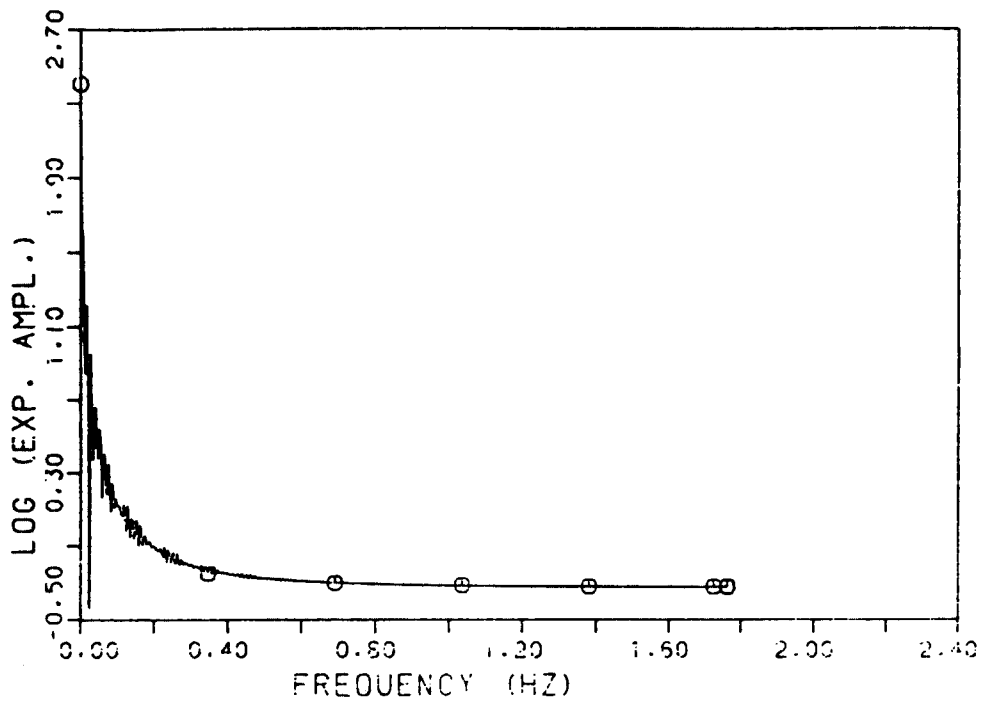
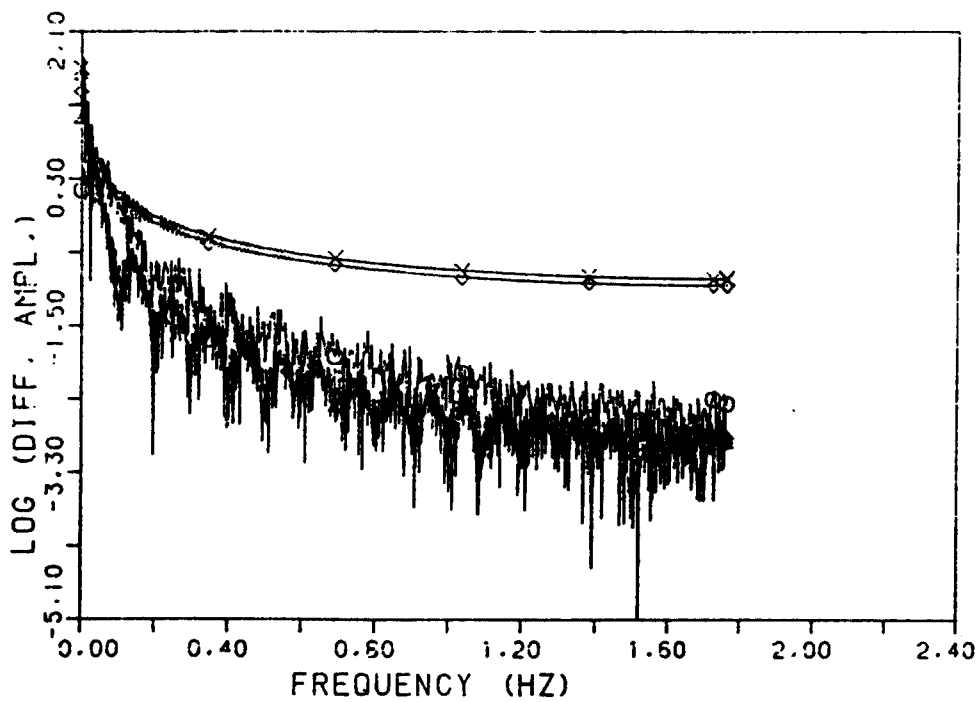


Fig. 3 - Sample Problem 2 : amplitude of FFT of the experimental signal



- LEGENDA
- CALC. 1
 - △ CALC. 2
 - + CALC. 3
 - × CALC. 4
 - ◇ CALC. 5
 - ⊕ CALC. 6

Fig. 4 - Sample Problem 2 : amplitude of FFT for calculated trends

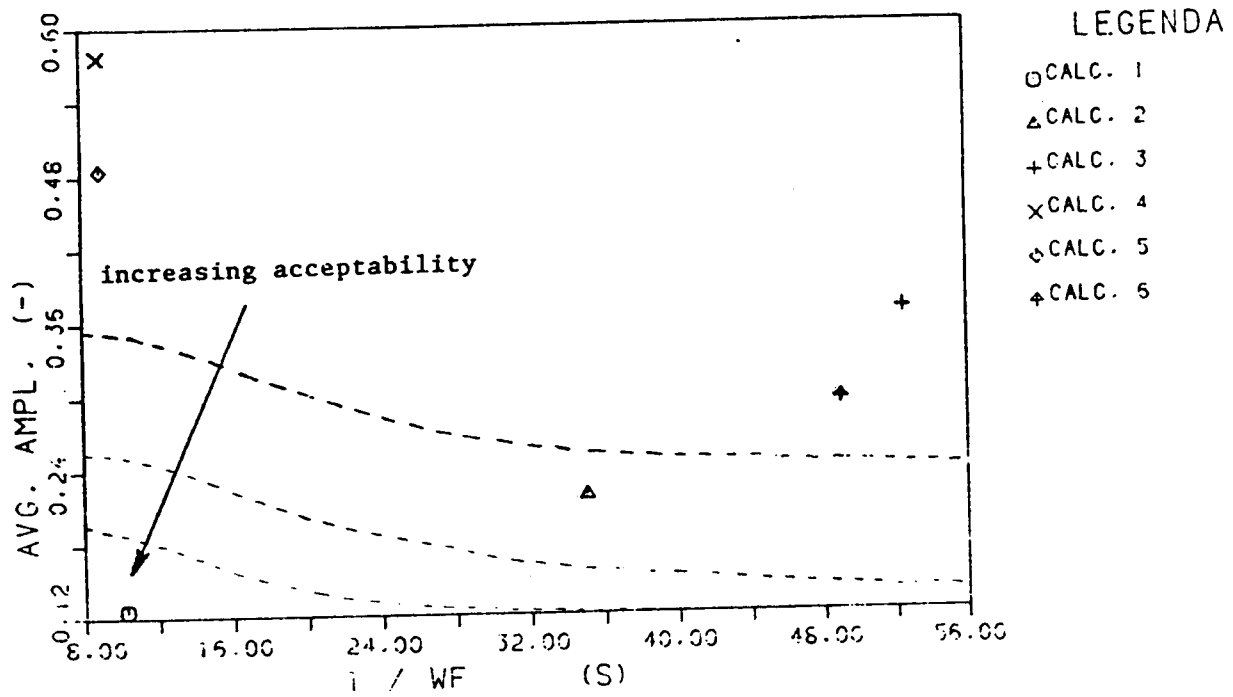


Fig. 5 - Sample Problem 2 : results for AA as a function of 1/WF

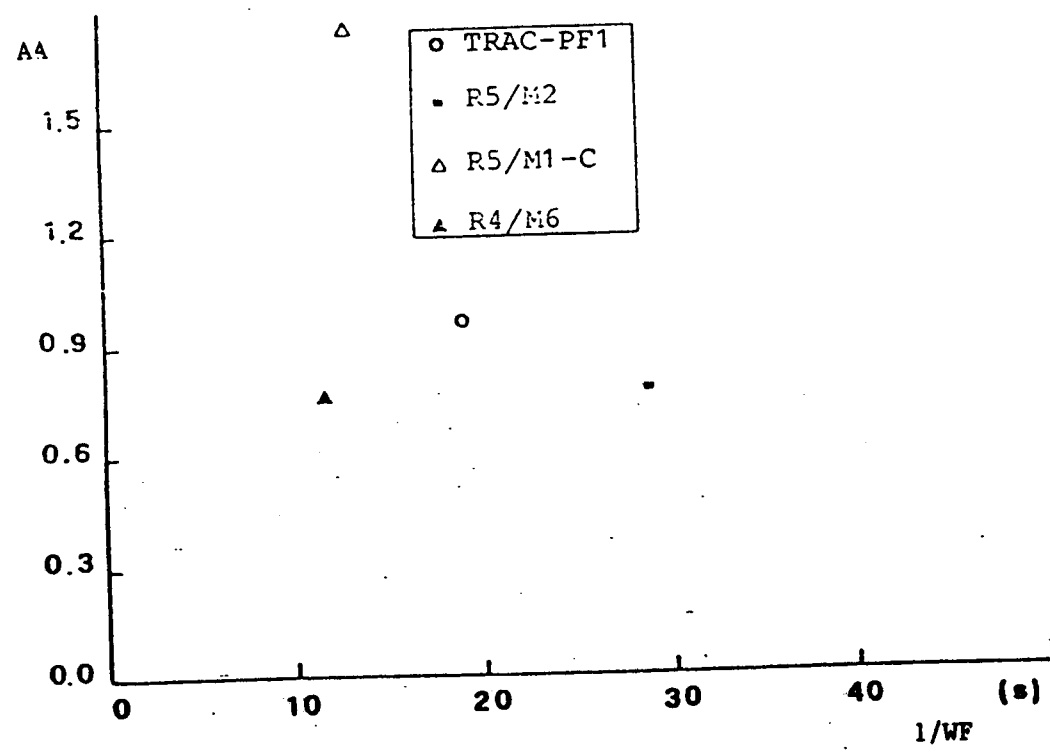


Fig. 6 - LOBI A2-81 (ISP 18): results for IL HL density

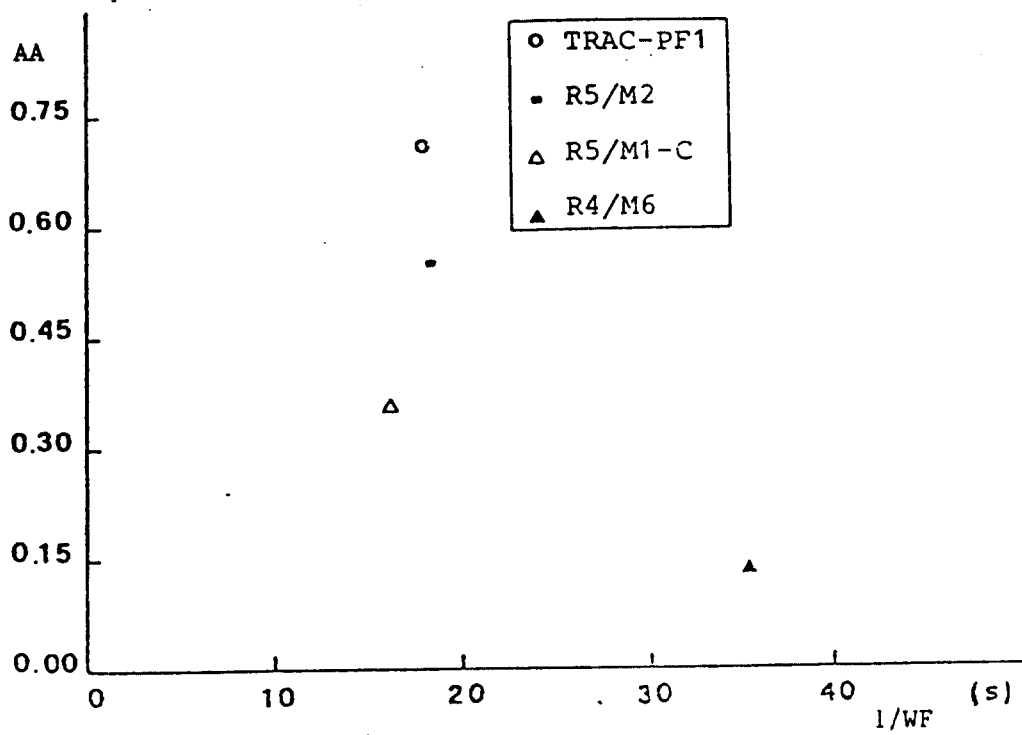


Fig. 7 - LOBI A2-81 (ISP 18): results for PS mass inventory

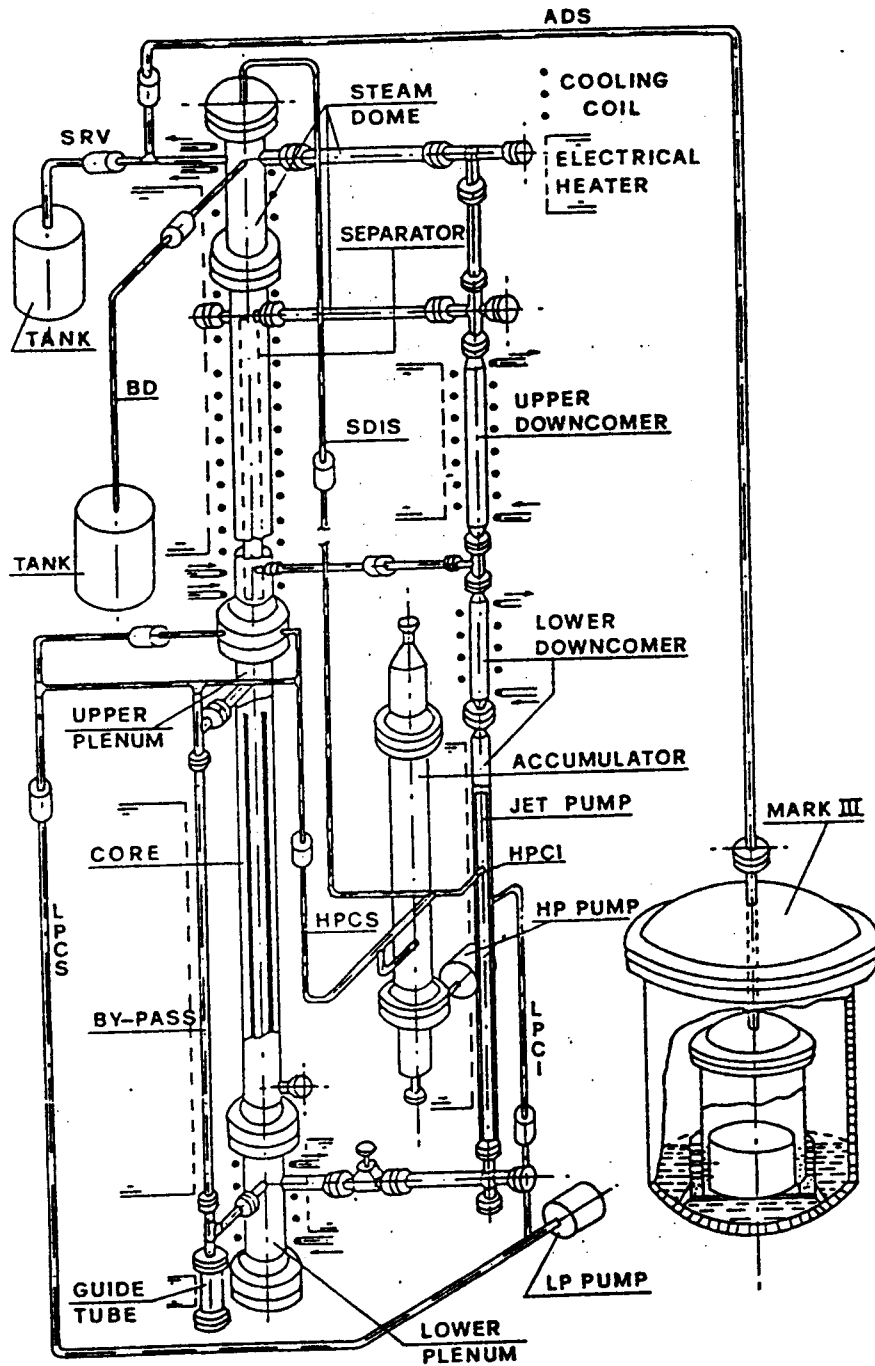


Fig. 8 - Sketch of PIPER-ONE Facility

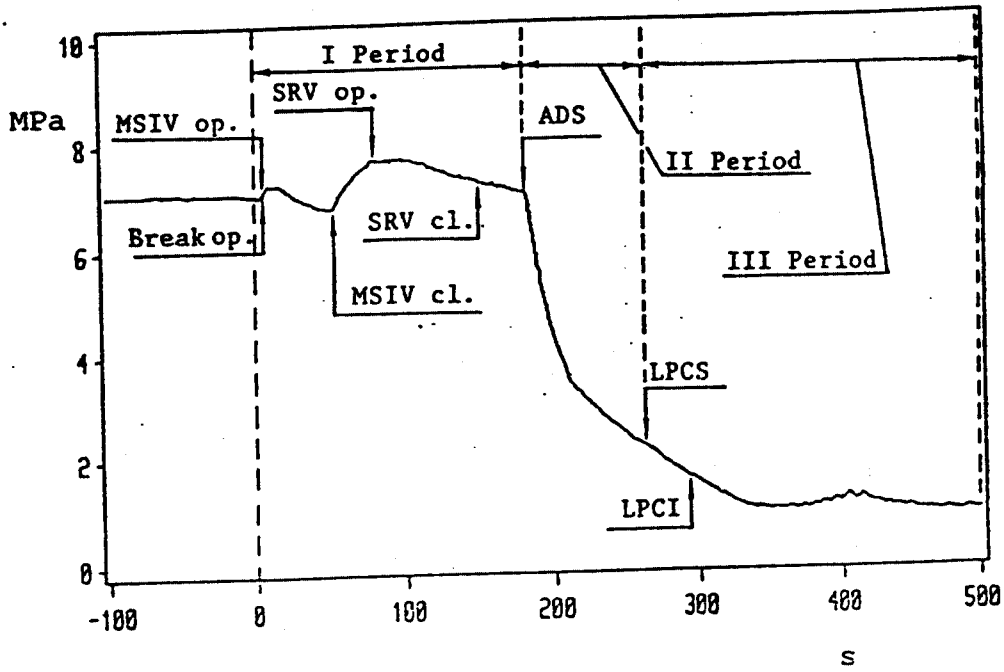


Fig. 9 - Test PO-SB-7 : System pressure and sequence of events

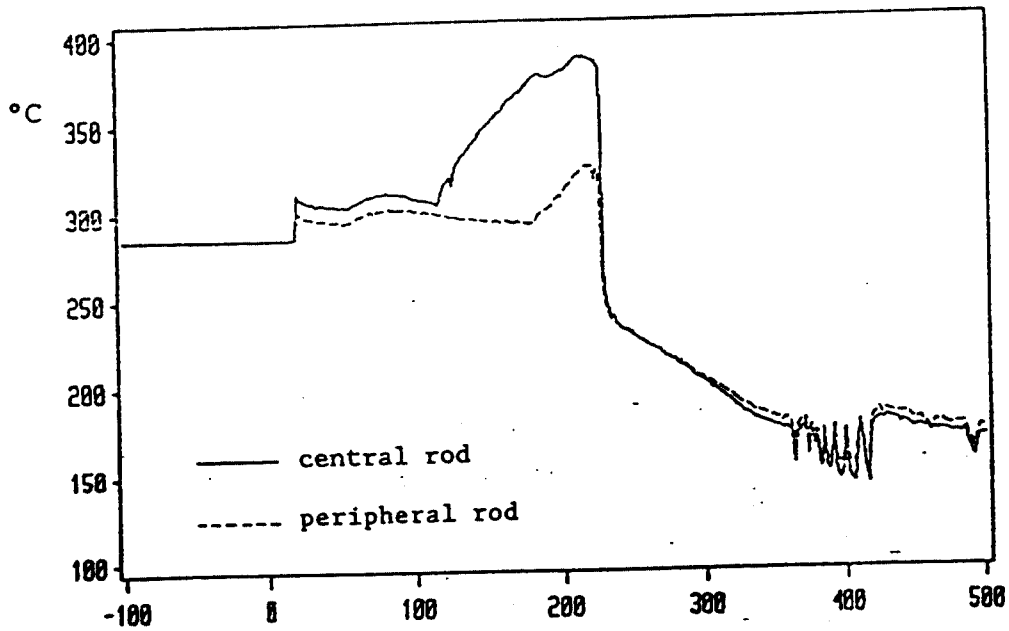


Fig. 10 - Test PO-SB-7 : Rod temperature (level G)

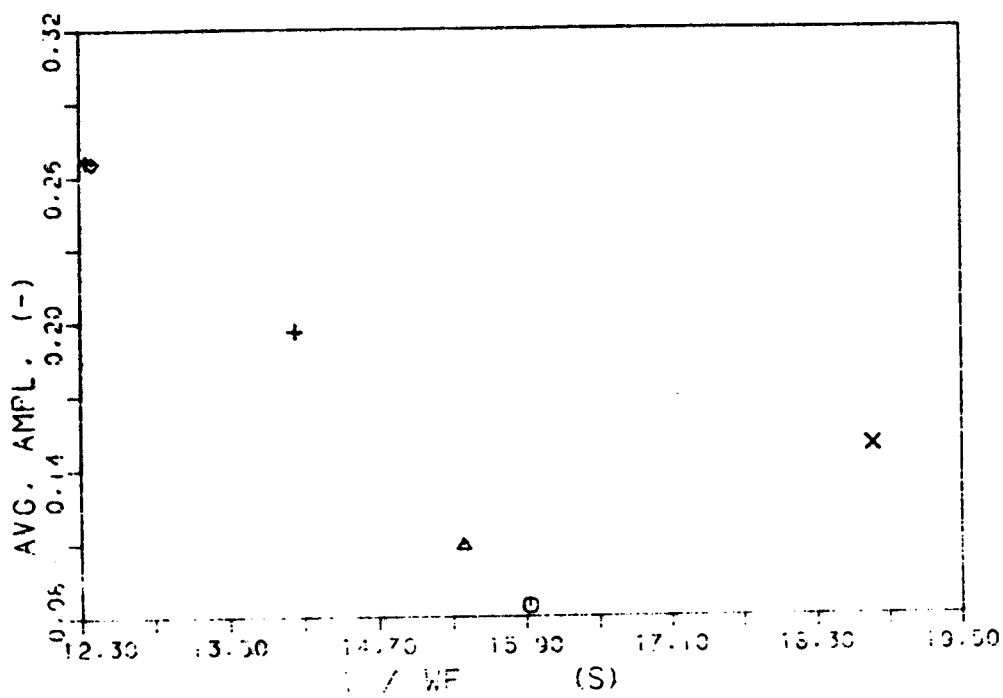


Fig. 11 - Double blind calculations : results for variable PA01

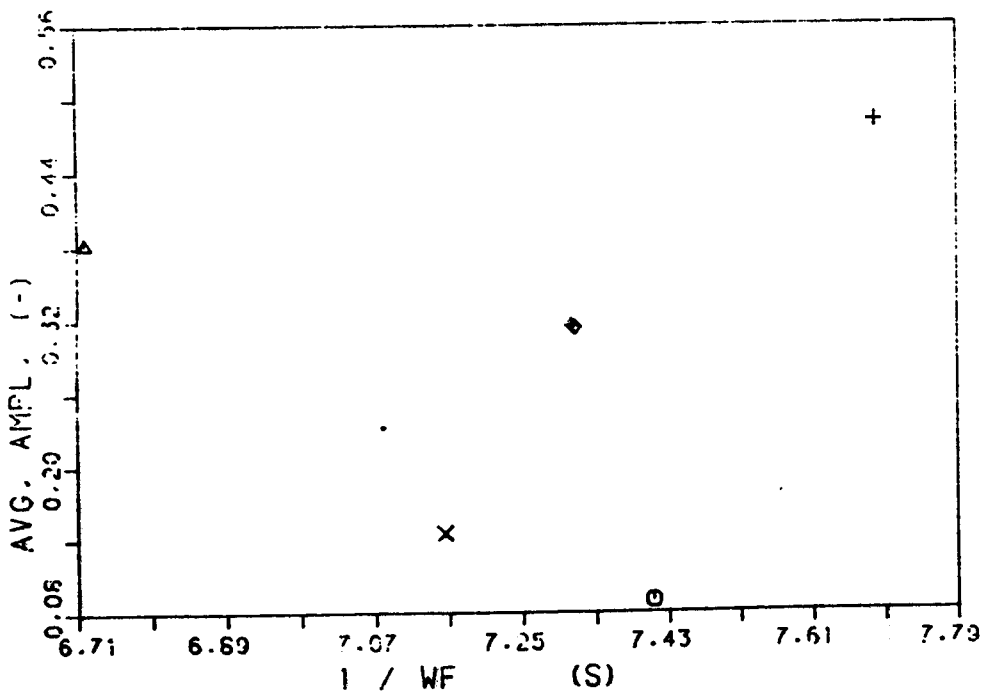
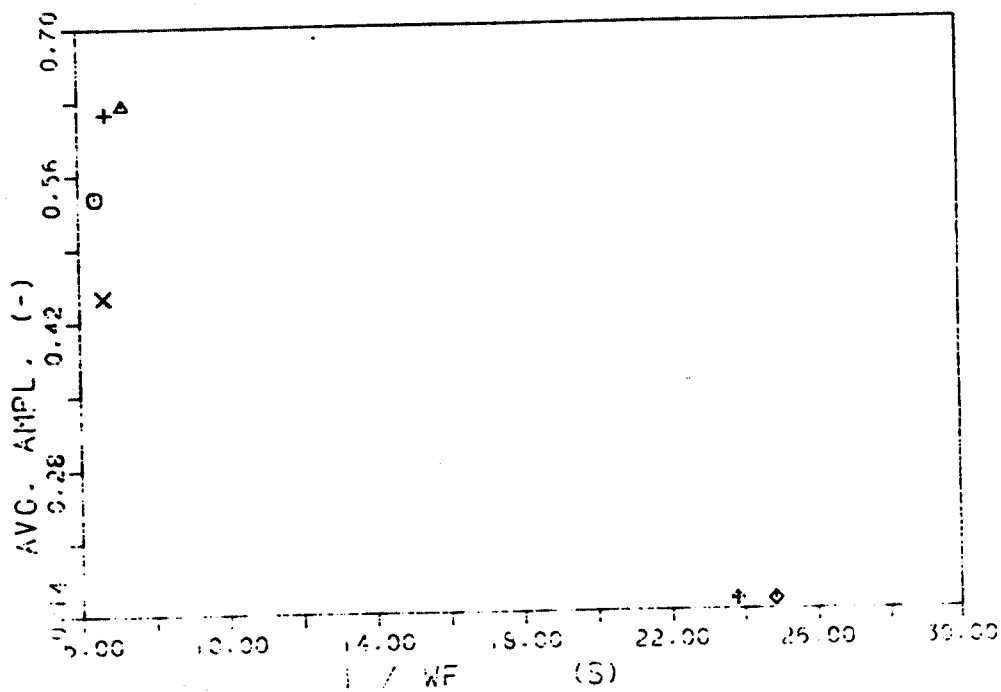
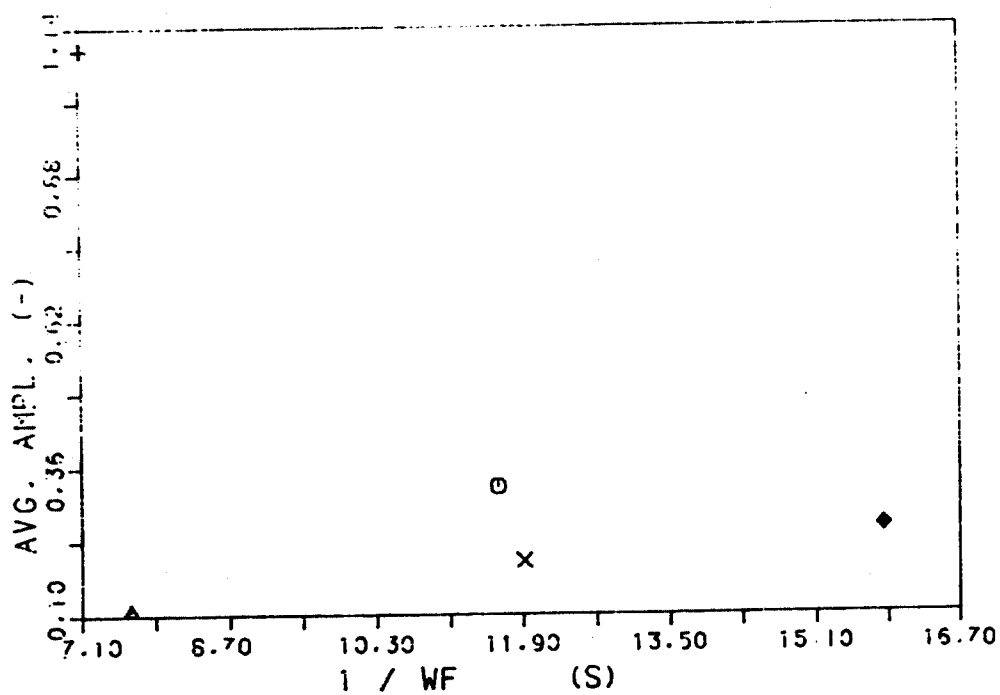


Fig. 12 - Double blind calculations : results for variable TF03



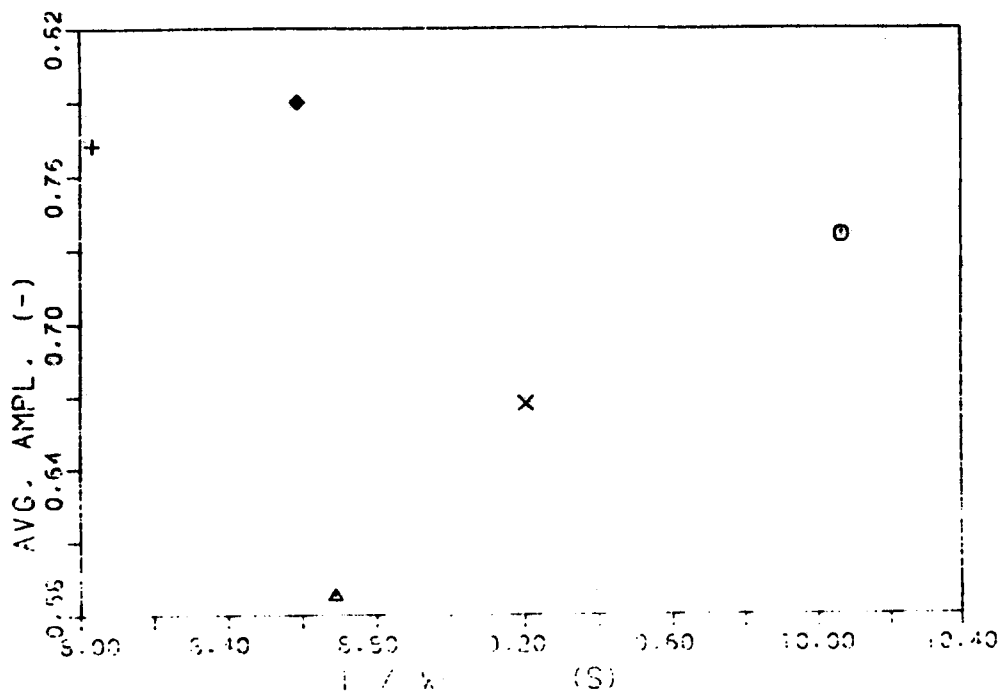
- LEGENDA
- ABB GOBLIN-FM
 - △ ANSALDO RELAP5/MOD2
 - + ENEL RELAP4/MOD6
 - × JAERI THYDE-B1/MOD2
 - ◇ VTT SMADRE (1)
 - ⋄ VTT SMADRE (2)

Fig. 13 - Double blind calculations : results for variable TF17



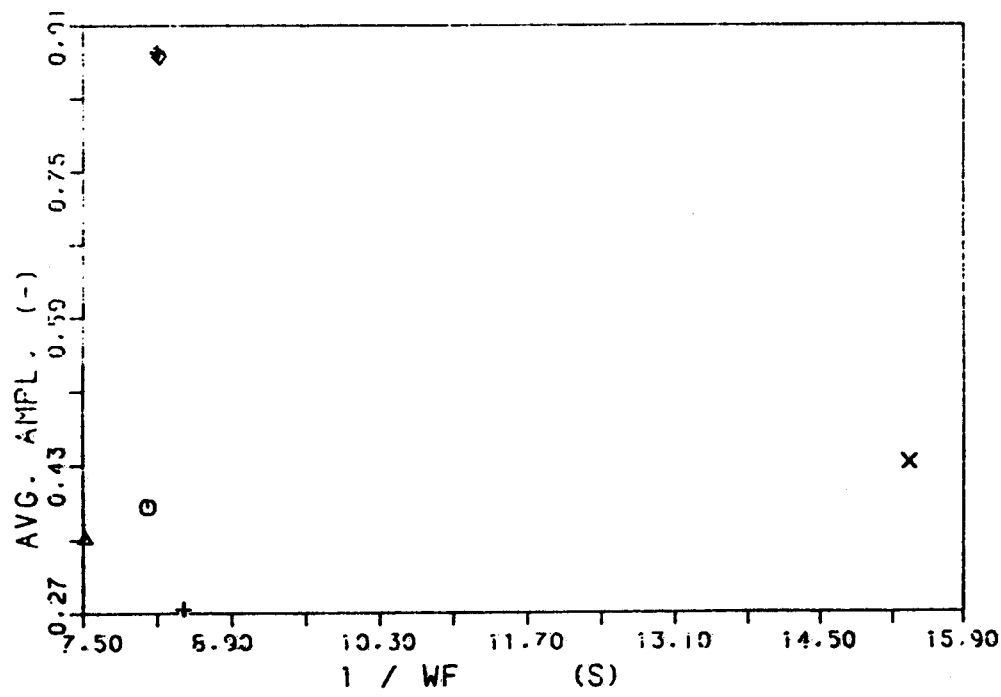
- LEGENDA
- ABB GOBLIN-FM
 - △ ANSALDO RELAP5/MOD2
 - + ENEL RELAP4/MOD6
 - × JAERI THYDE-B1/MOD2
 - ◇ VTT SMADRE (1)
 - ⋄ VTT SMADRE (2)

Fig. 14 - Double blind calculations : results for variable CL70



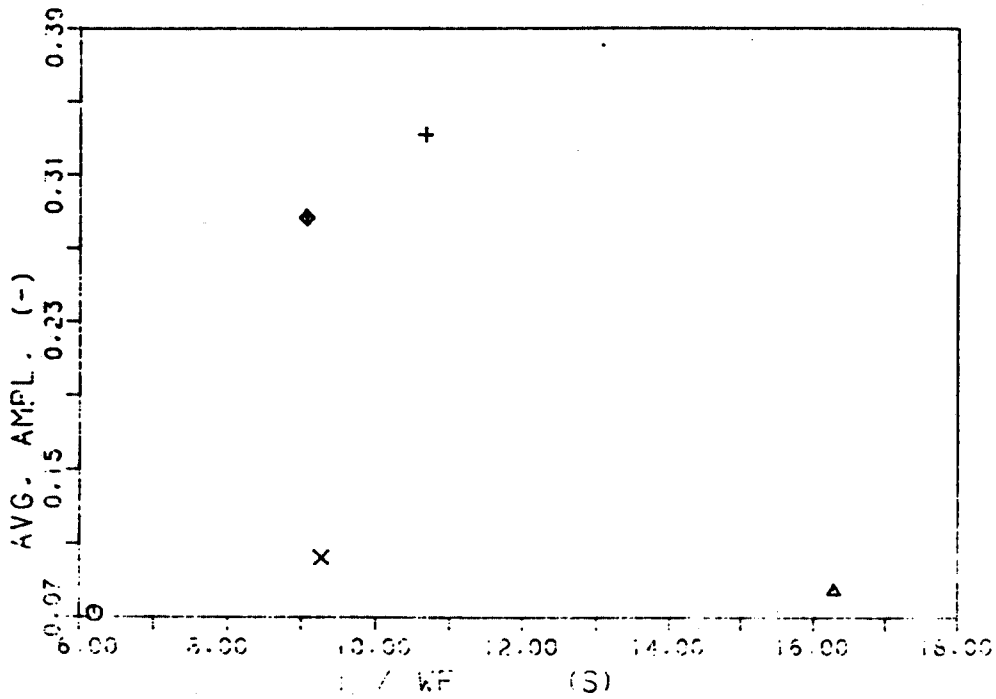
- LEGENDA
- ABB GOBLIN-EM
 - △ ANSALDO RELAP5/MOD2
 - + ENEL RELAP4/MOD6
 - × JAERI THYDE-B1/MOD2
 - ◇ VTT SMABRE (1)
 - ↑ VTT SMABRE (2)

Fig. 15 - Double blind calculations : results for variable MF43



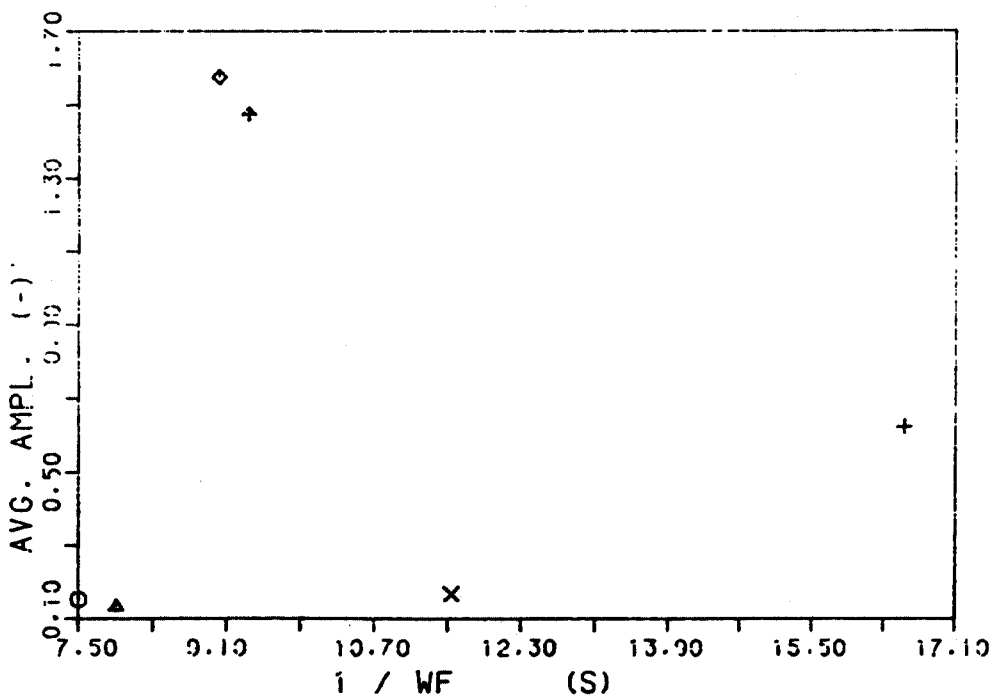
- LEGENDA
- ABB GOBLIN-EM
 - △ ANSALDO RELAP5/MOD2
 - + ENEL RELAP4/MOD6
 - × JAERI THYDE-B1/MOD2
 - ◇ VTT SMABRE (1)
 - ↑ VTT SMABRE (2)

Fig. 16 - Double blind calculations : results for variable MF48



- LEGENDA
- ABB COBLIN-EM
 - △ ANSALDO RELAP5/MOD2
 - + ENEL RELAP4/MOD6
 - × JAERI THYDE-B1/MOD2
 - ◇ VTT SMABRE (1)
 - ‡ VTT SMABRE (2)

Fig. 17 - Double blind calculations : results for variable TR50



- LEGENDA
- ABB COBLIN-EM
 - △ ANSALDO RELAP5/MOD2
 - + ENEL RELAP4/MOD6
 - × JAERI THYDE-B1/MOD2
 - ◇ VTT SMABRE (1)
 - ‡ VTT SMABRE (2)

Fig. 18 - Double blind calculations : results for variable TR52

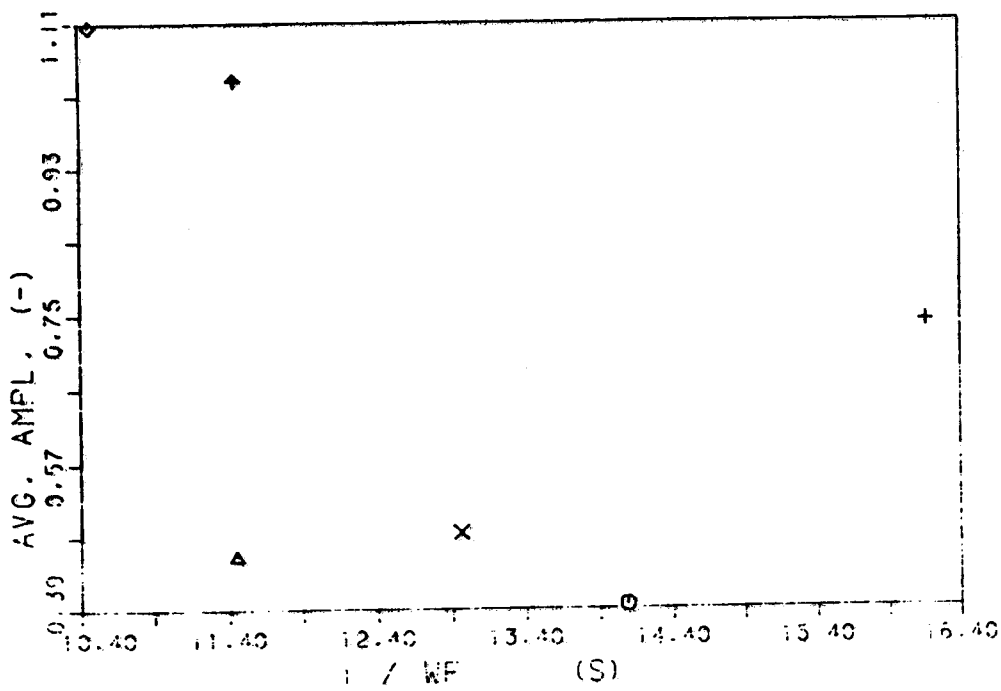


Fig. 19 - Double blind calculations : results for variable TR55

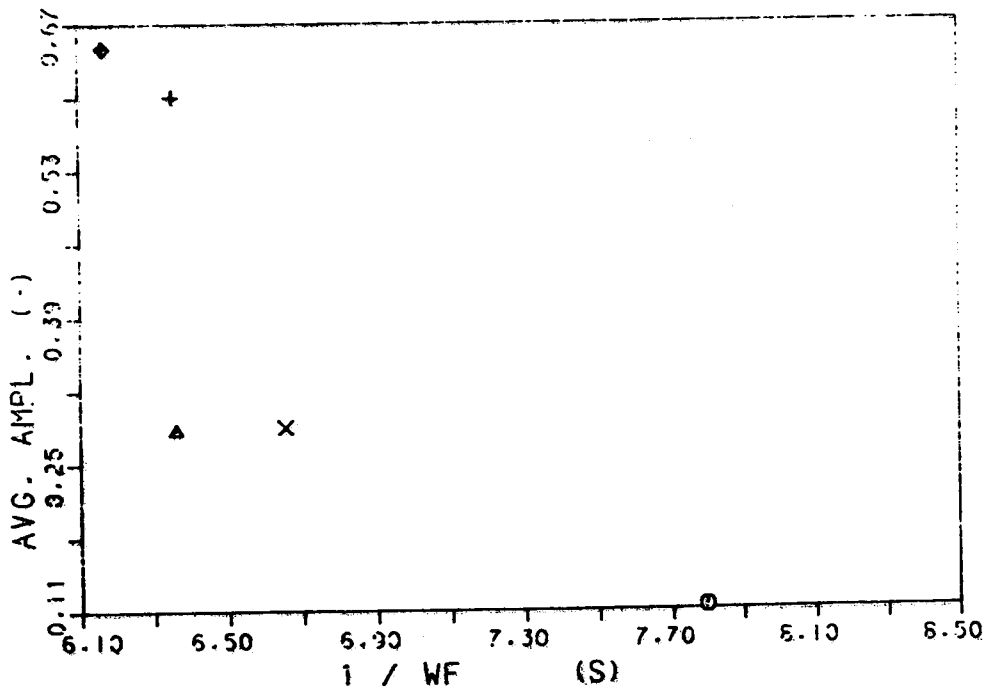
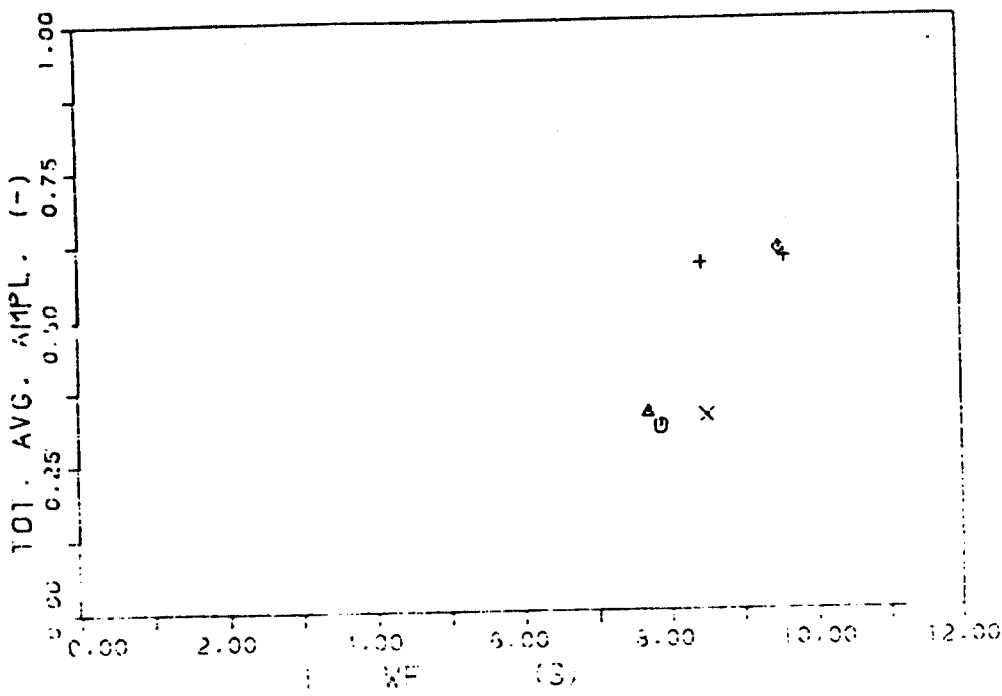
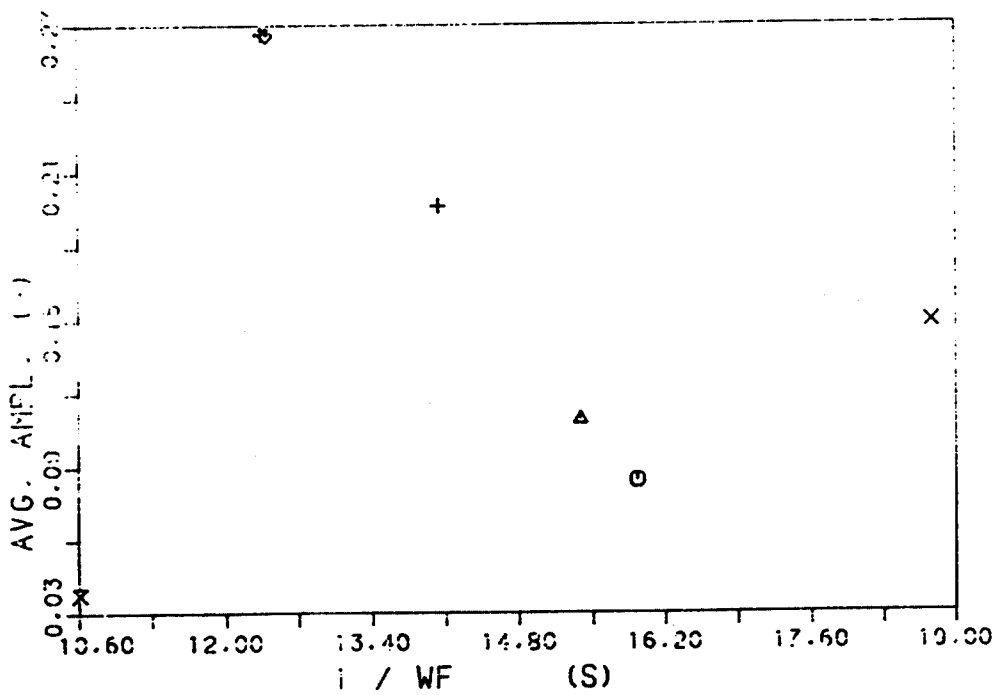


Fig. 20 - Double blind calculations : results for variable RM65



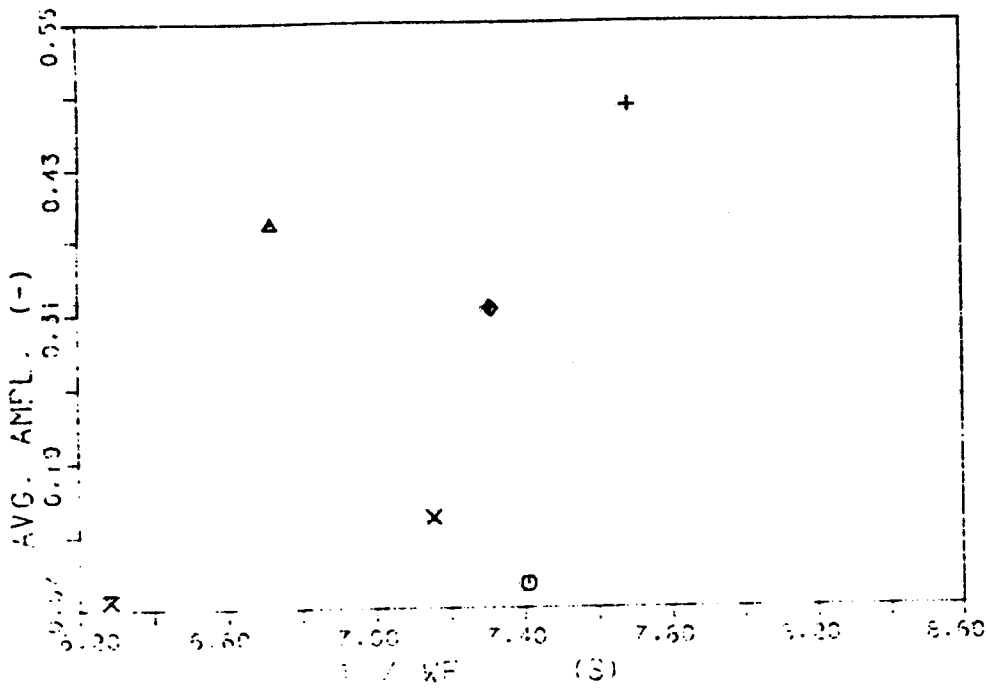
- LEGENDA
- ABB COBLIN-EM
 - △ ANSALDO RELAP5/MOD2
 - + ENEL RELAP4/MOD6
 - × JAERI THYDE-B1
 - ◊ VTT SMABRE (1)
 - ◊ VTT SMABRE (2)

Fig. 21 - Double blind calculations : overall results



- LEGENDA
- ABB COBLIN-EM
 - △ ANSALDO RELAP5/MOD2
 - + ENEL RELAP4/MOD6
 - × JAERI THYDE-B1/MOD2
 - ◊ VTT SMABRE (1)
 - ◊ VTT SMABRE (2)
 - × DCMN RELAP5/MOD2 (PA01)

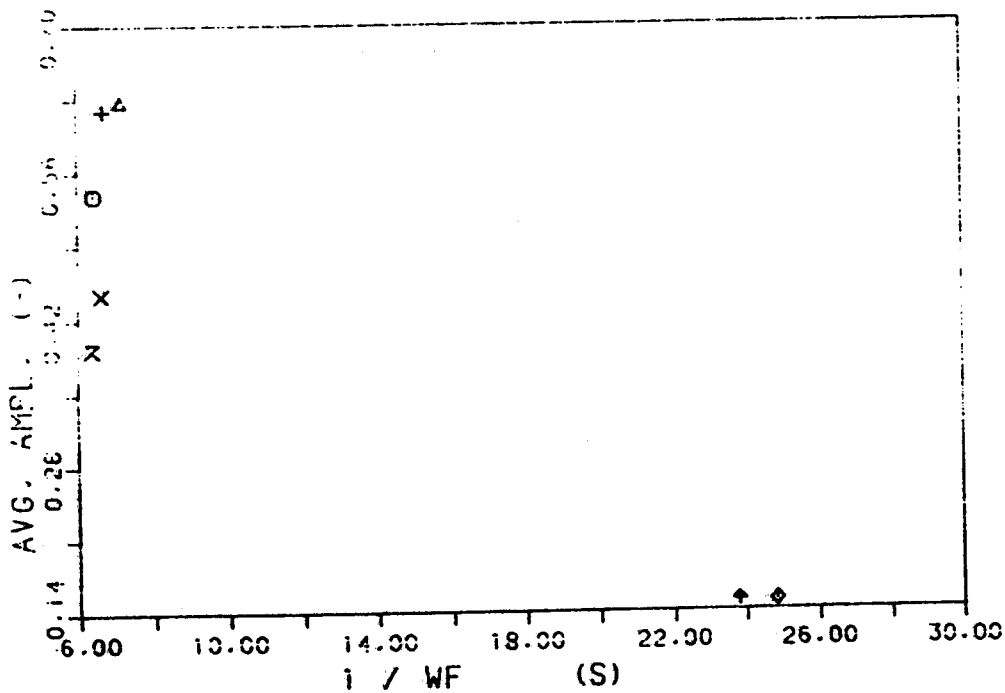
Fig. 22 - Comparison between double blind and DCMN post-test calculations : variable PA01



LEGENDA

- ABB GOBLIN-EM
- △ ANSALDO RELAP5/MOD2
- + ENEL RELAP4/MOD6
- x JAERI THYDE-B1/MOD2
- ◇ VTT SMABRE (1)
- + VTT SMABRE (2)
- x DCMN RELAP5/MOD2 (P. 1.1)

Fig. 23 - Comparison between double blind and DCMN post-test calculations : variable TF03



LEGENDA

- ABB GOBLIN-EM
- △ ANSALDO RELAP5/MOD2
- + ENEL RELAP4/MOD6
- x JAERI THYDE-B1/MOD2
- ◇ VTT SMABRE (1)
- + VTT SMABRE (2)
- x DCMN RELAP5/MOD2 (P. 1.1)

Fig. 24 - Comparison between double blind and DCMN post-test calculations : variable TF17

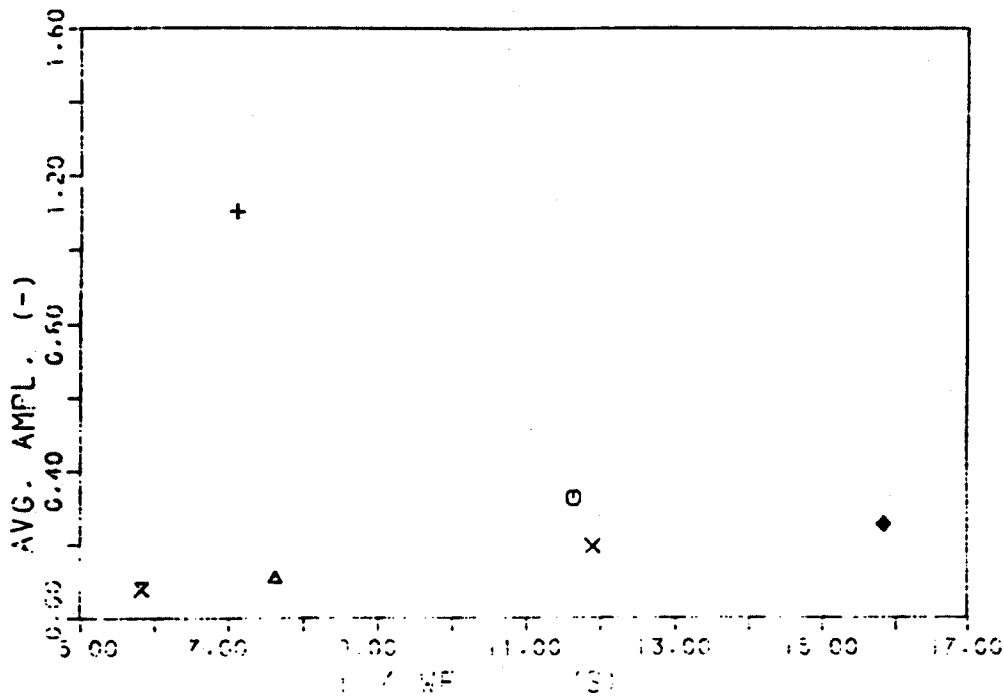


Fig. 25 - Comparison between double blind and DCMN post-test calculations : variable CL70

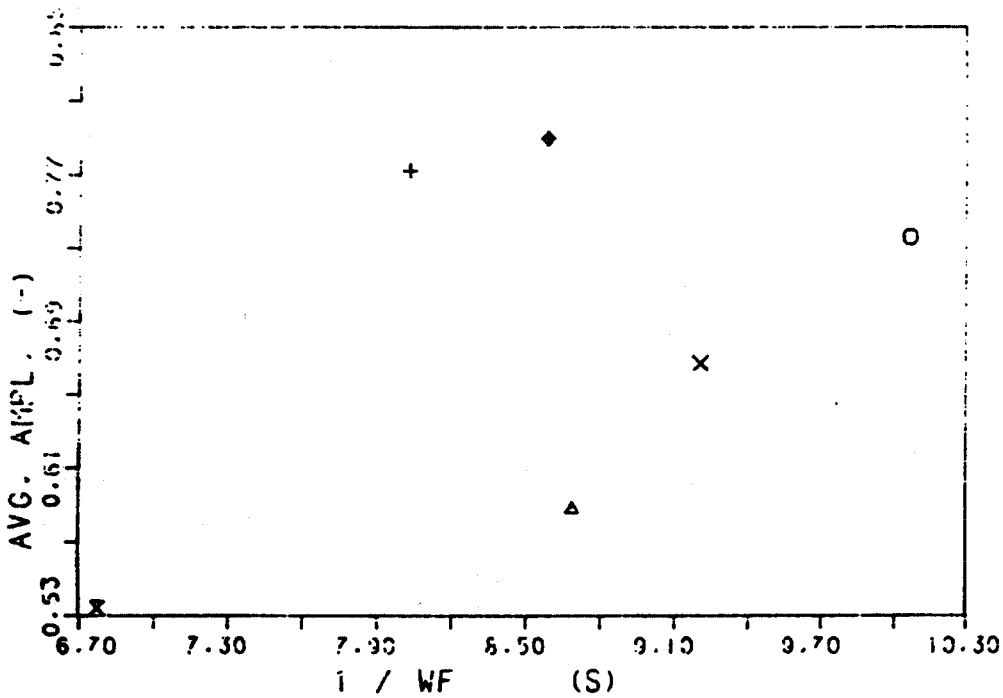
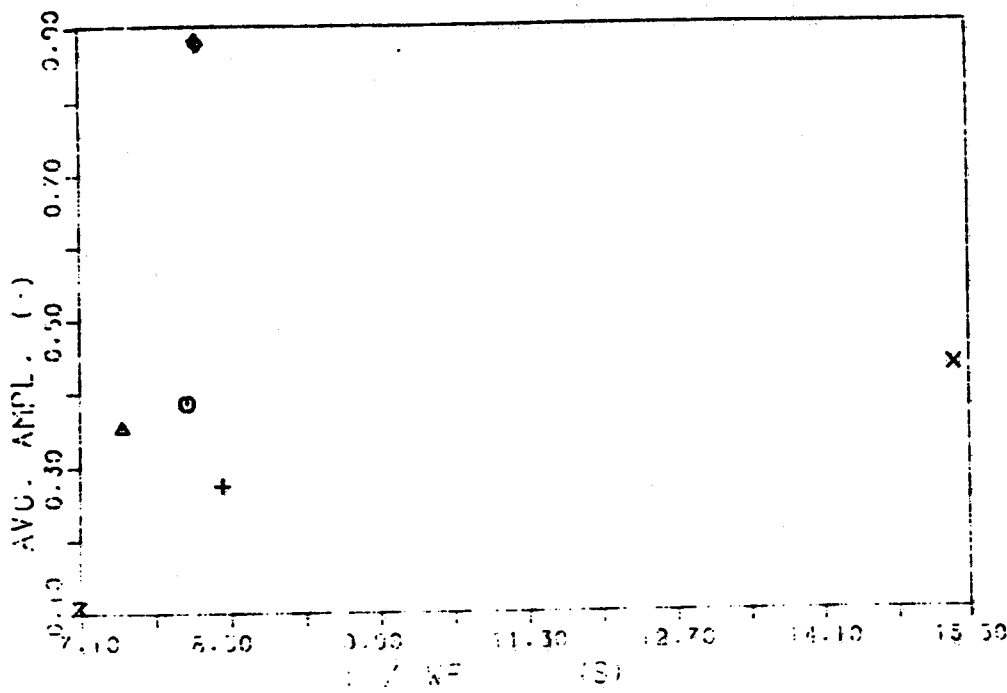
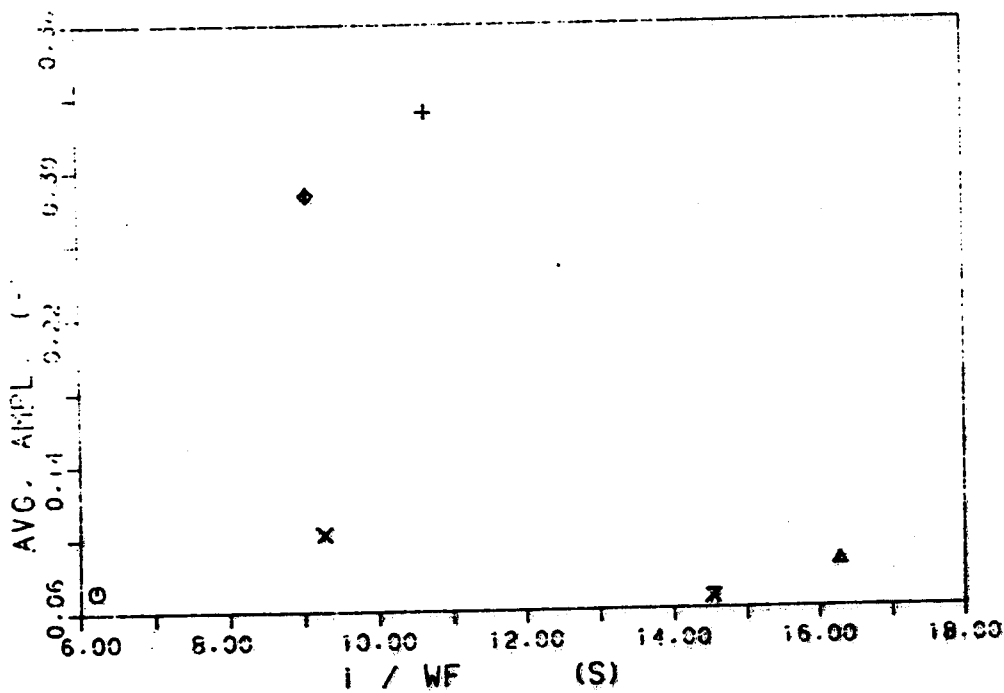


Fig. 26 - Comparison between double blind and DCMN post-test calculations : variable MF43



- LEGENDA
- ABB GOSLIN-EM
 - △ ANGALDO RELAP5/MOD2
 - + ENEL RELAP4/MOD6
 - × JAERI THYDE-B1/MOD2
 - ◇ VTT SMABRE (1)
 - ♣ VTT SMABRE (2)
 - ⊗ DCMN RELAP5/MOD2 (P.1)

Fig. 27 - Comparison between double blind and DCMN post-test calculations : variable MF48



- LEGENDA
- ABB GOSLIN-EM
 - △ ANGALDO RELAP5/MOD2
 - + ENEL RELAP4/MOD6
 - × JAERI THYDE-B1/MOD2
 - ◇ VTT SMABRE (1)
 - ♣ VTT SMABRE (2)
 - ⊗ DCMN RELAP5/MOD2 (P.1)

Fig. 28 - Comparison between double blind and DCMN post-test calculations : variable TR50

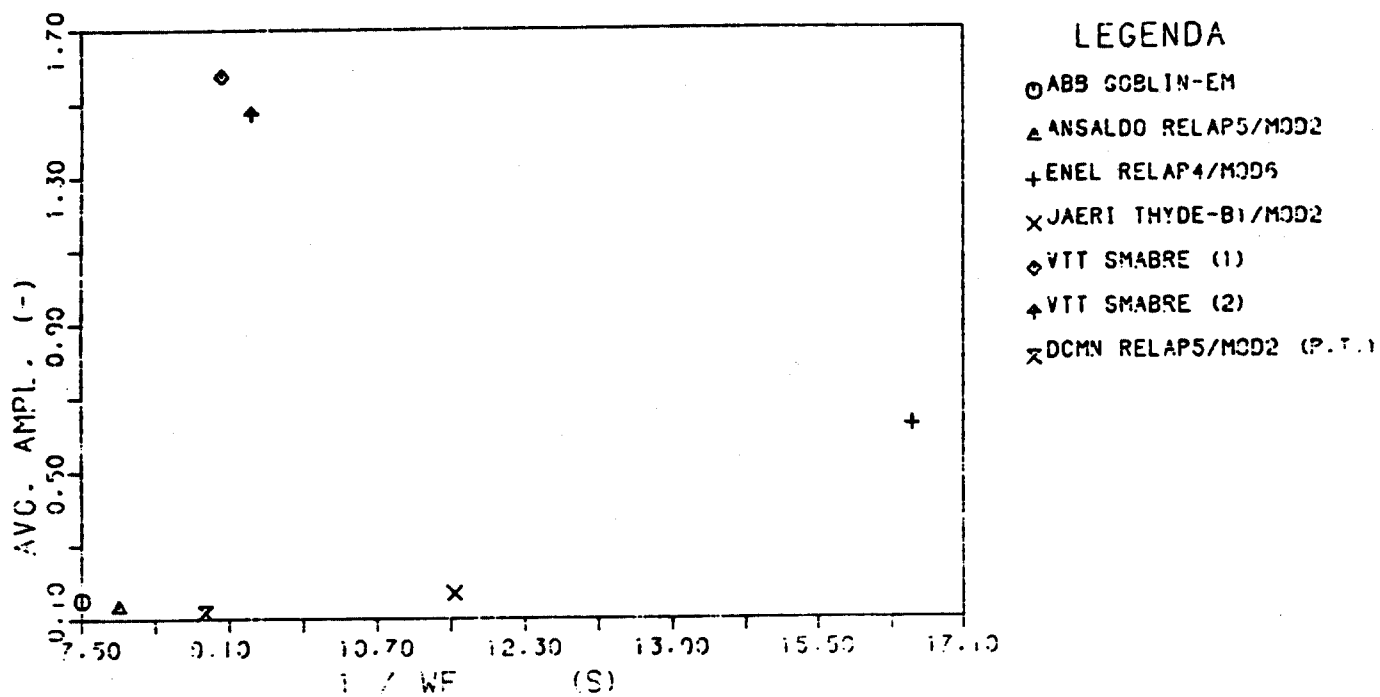


Fig. 29 - Comparison between double blind and DCMN post-test calculations : variable TR52

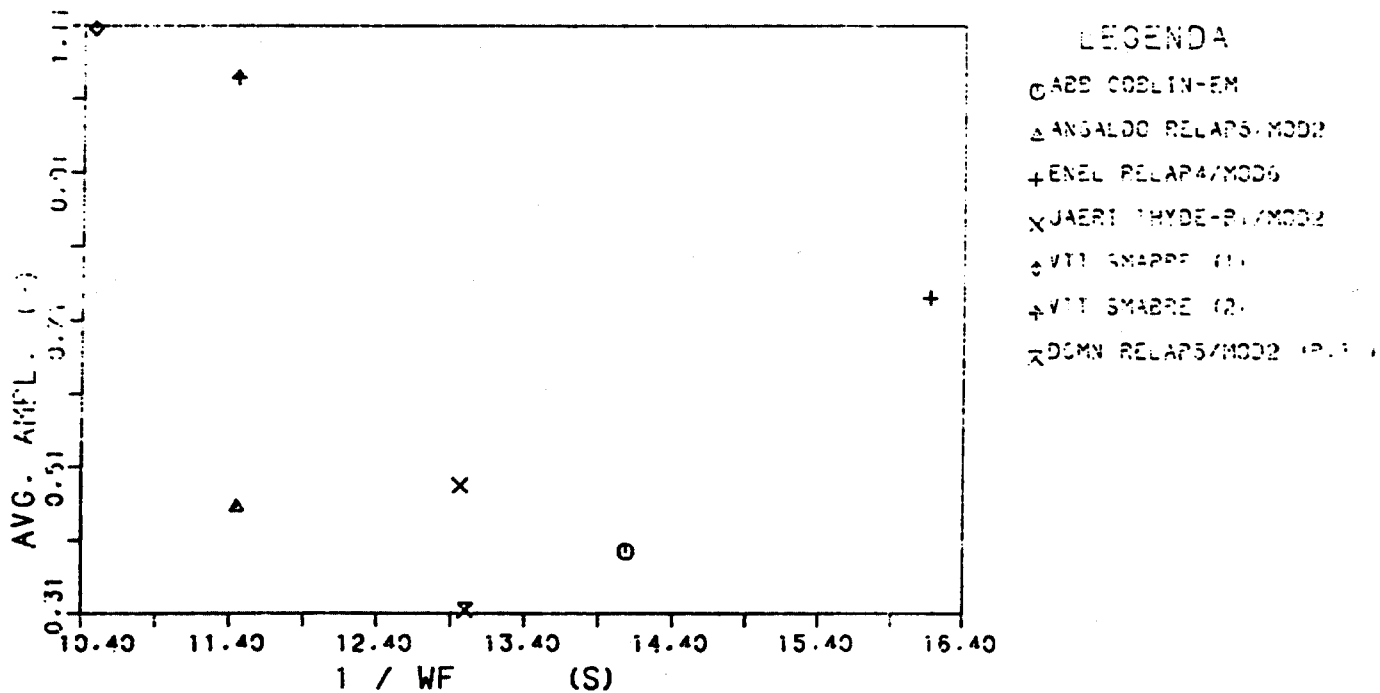
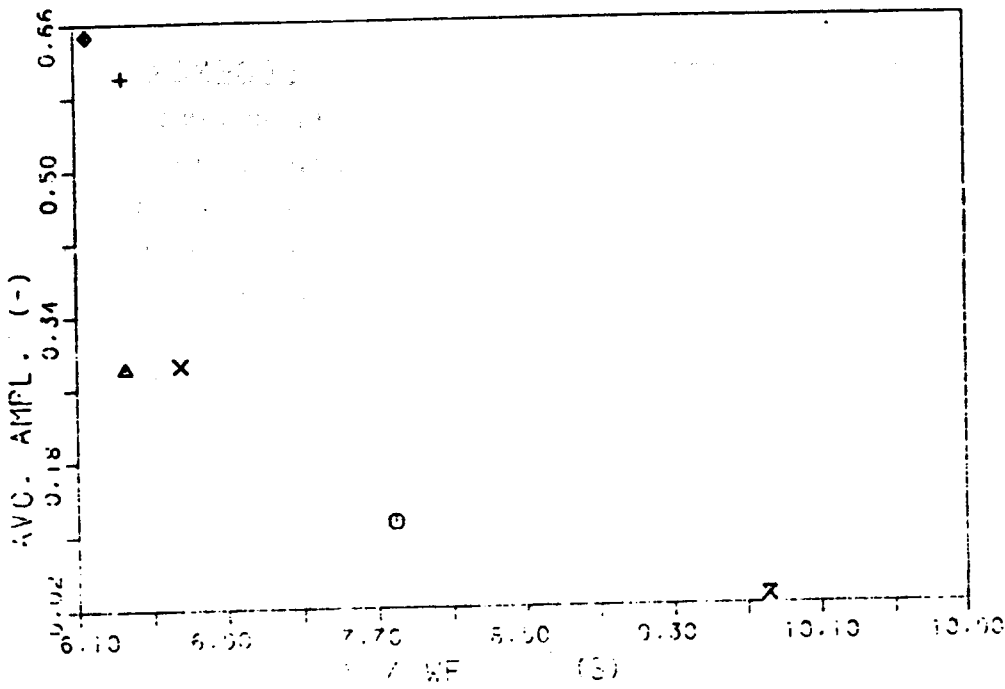
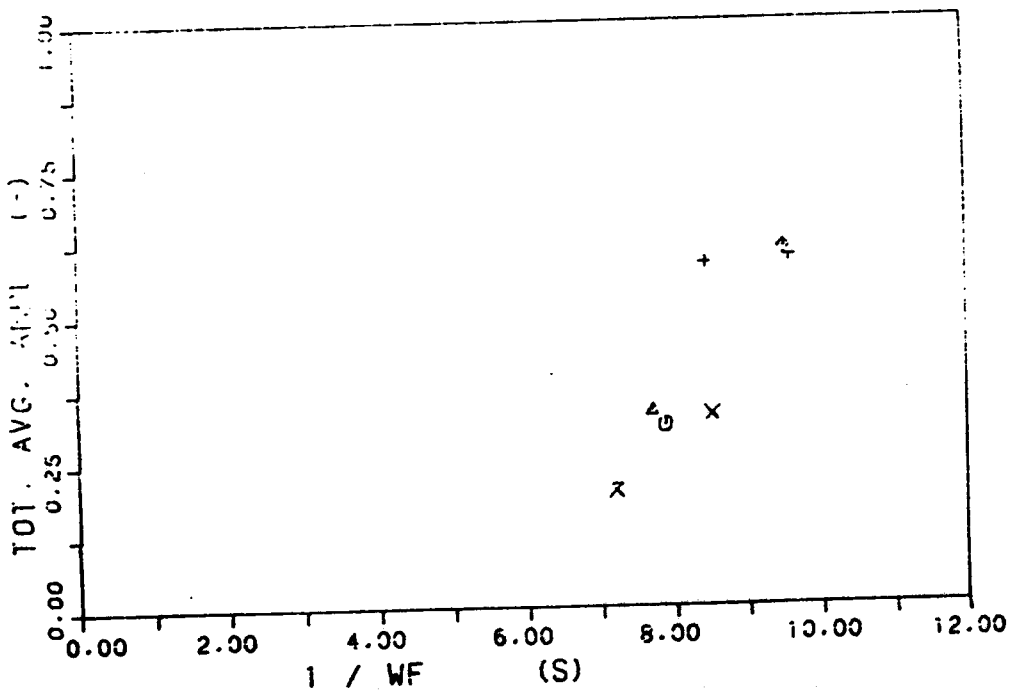


Fig. 30 - Comparison between double blind and DCMN post-test calculations : variable TR55



- LEGENDA
- ABB GOBLIN-EM
 - △ ANSALDO RELAPS/MOD2
 - + ENEL RELAP4/MOD6
 - × JAERI THYDE-B1/MOD2
 - ◇ VTT SMABRE (1)
 - ↑ VTT SMABRE (2)
 - ⊗ DCMN RELAPS/MOD2 (P.T.)

Fig. 31 - Comparison between double blind and DCMN post-test calculations : variable RM65



- LEGENDA
- ABB GOBLIN-EM
 - △ ANSALDO RELAPS/MOD2
 - + ENEL RELAP4/MOD6
 - × JAERI THYDE-B1
 - ◇ VTT SMABRE (1)
 - ↑ VTT SMABRE (2)
 - ⊗ DCMN RELAPS/MOD2 (P.T.)

Fig. 32 - Comparison between double blind and DCMN post-test calculations : overall results

APPENDIX A - Figures concerning double blind calculations

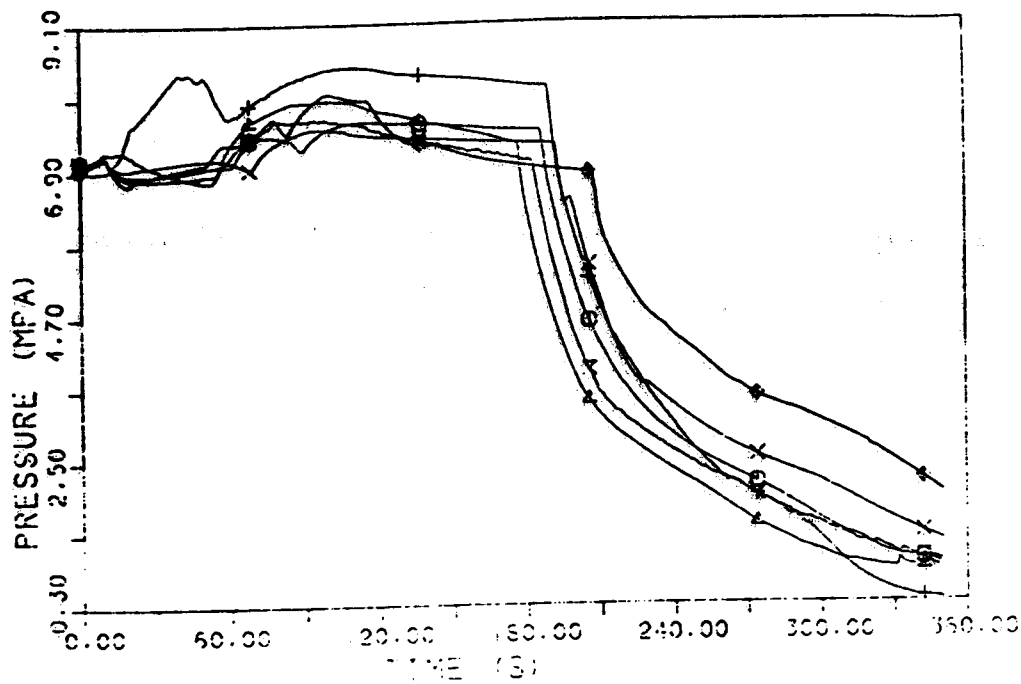


Fig. A.1 - Variable PA01 : experimental and calculated trends

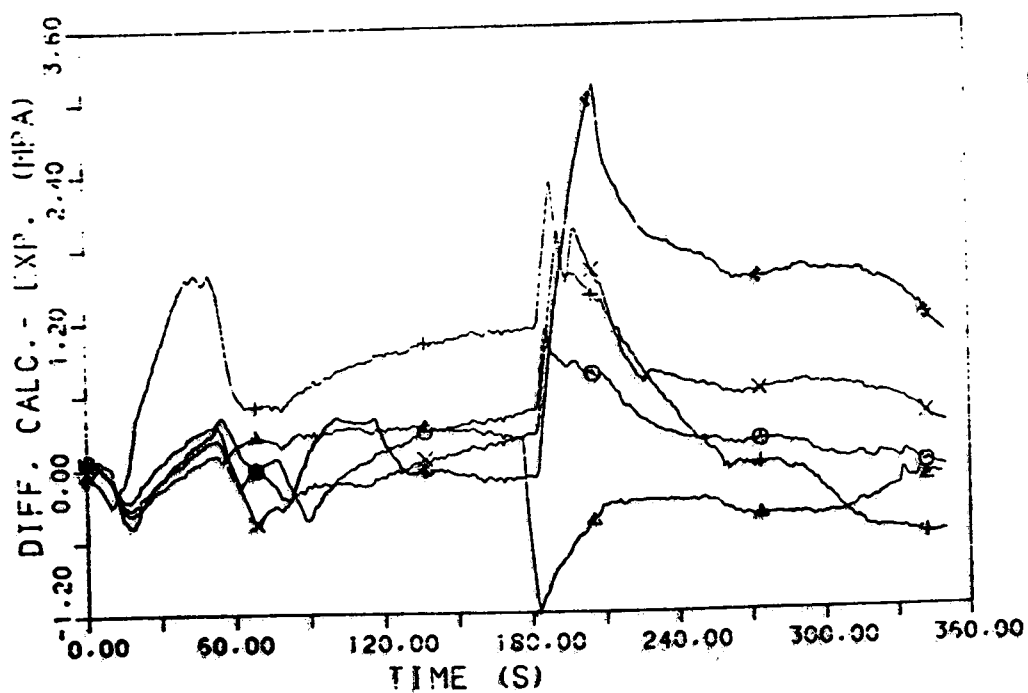


Fig. A.2 - Variable PA01 : difference between calculated and experimental trends

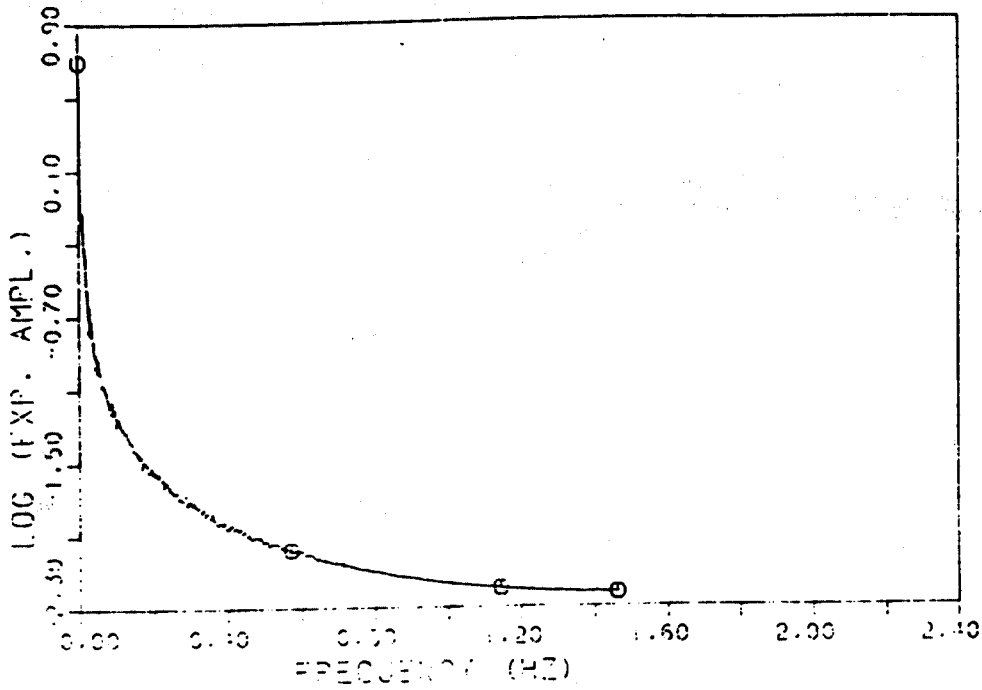
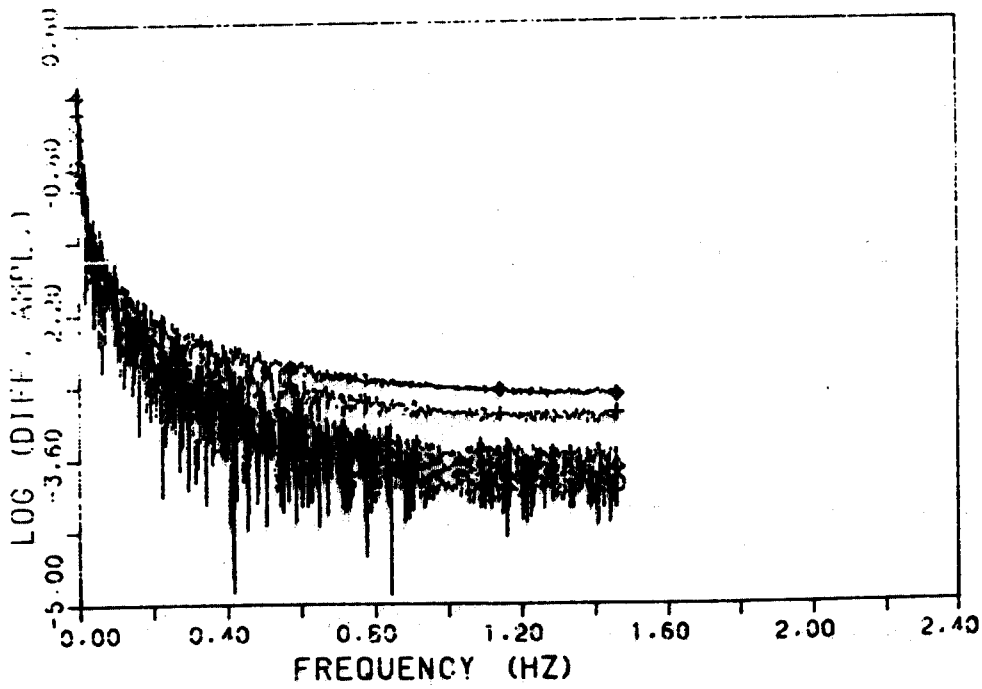
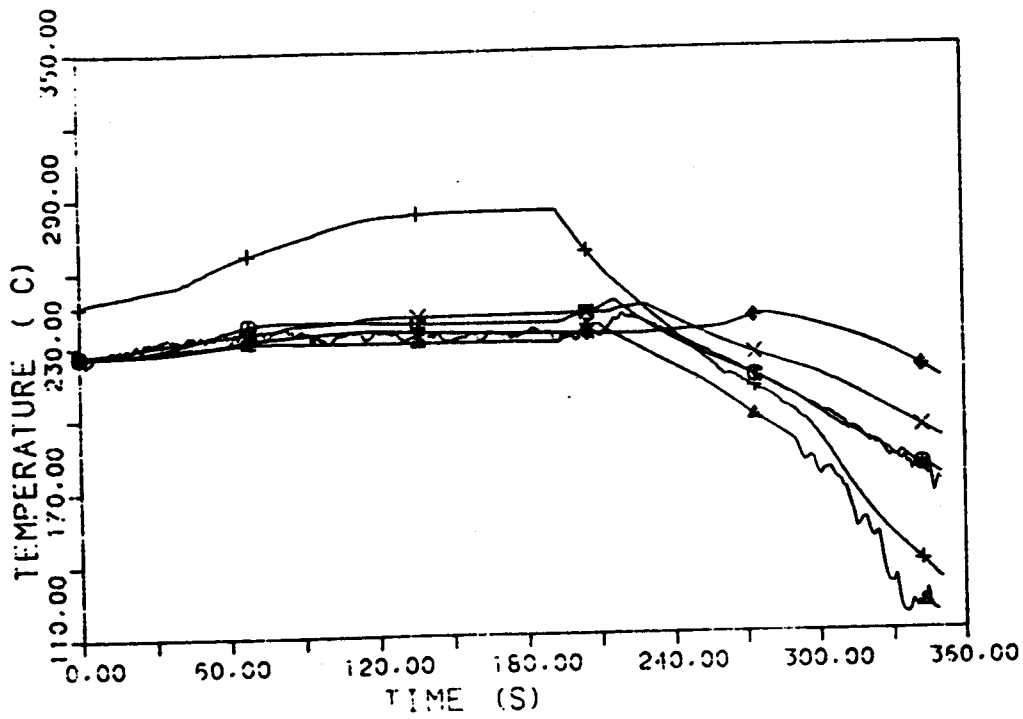


Fig. A.3 - Variable PA01 : amplitude of the FFT of the experimental trend



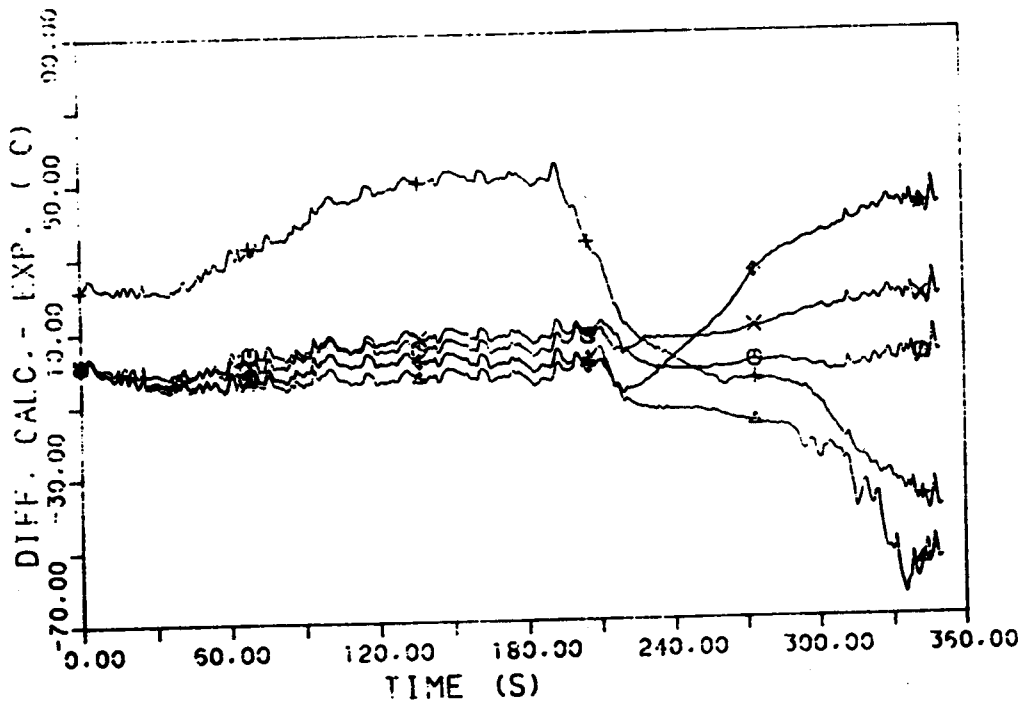
- LEGENDA
- ABB COBLIN-EM
 - △ ANSALDO RELAP5/MOD2
 - + ENEL RELAP4/MOD6
 - x JAERI THYDE-BI/MOD2
 - ◇ VIT SMABRE (1)
 - ⊕ VIT SMABRE (2)

Fig. A.4 - Variable PA01 : amplitude of the FFT of the difference between calculated and experimental trends



- LEGENDA
- ABB COSLIN-EM
 - △ ANSALDO RELAP5/MOD2
 - + ENEL RELAP4/MOD6
 - × JAERI THYDE-B1/MOD2
 - ◊ VTT SMABRE (1)
 - + VTT SMABRE (2)
 - × EXP.

Fig. A.5 - Variable TF03 : experimental and calculated trends



- LEGENDA
- ABB COSLIN-EM
 - △ ANSALDO RELAP5/MOD2
 - + ENEL RELAP4/MOD6
 - × JAERI THYDE-B1/MOD2
 - ◊ VTT SMABRE (1)
 - + VTT SMABRE (2)

Fig. A.6 - Variable TF03 : difference between calculated and experimental trends

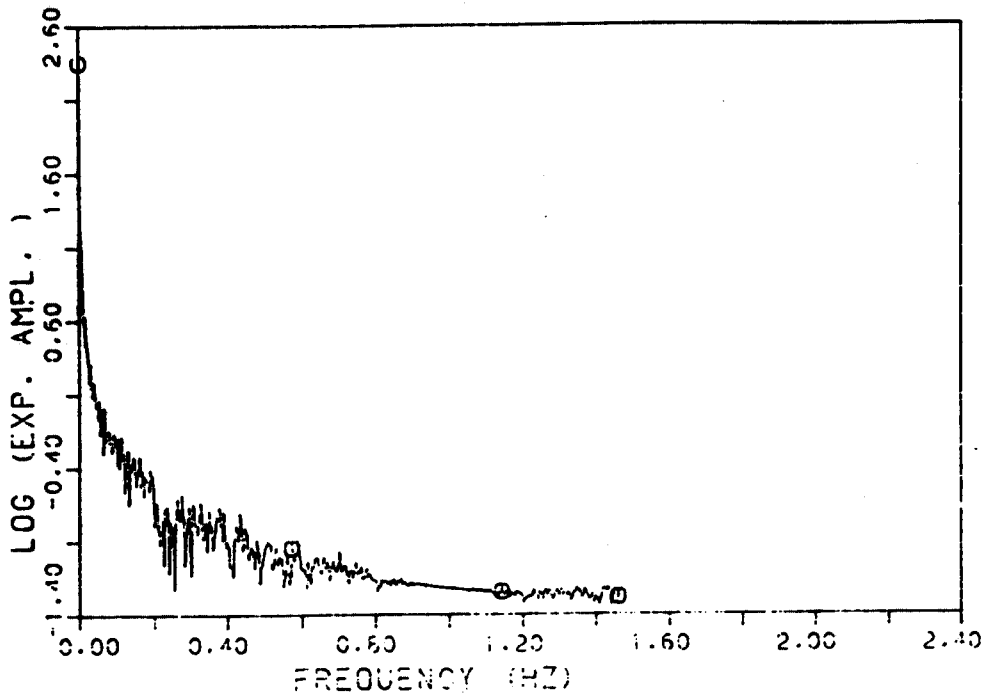
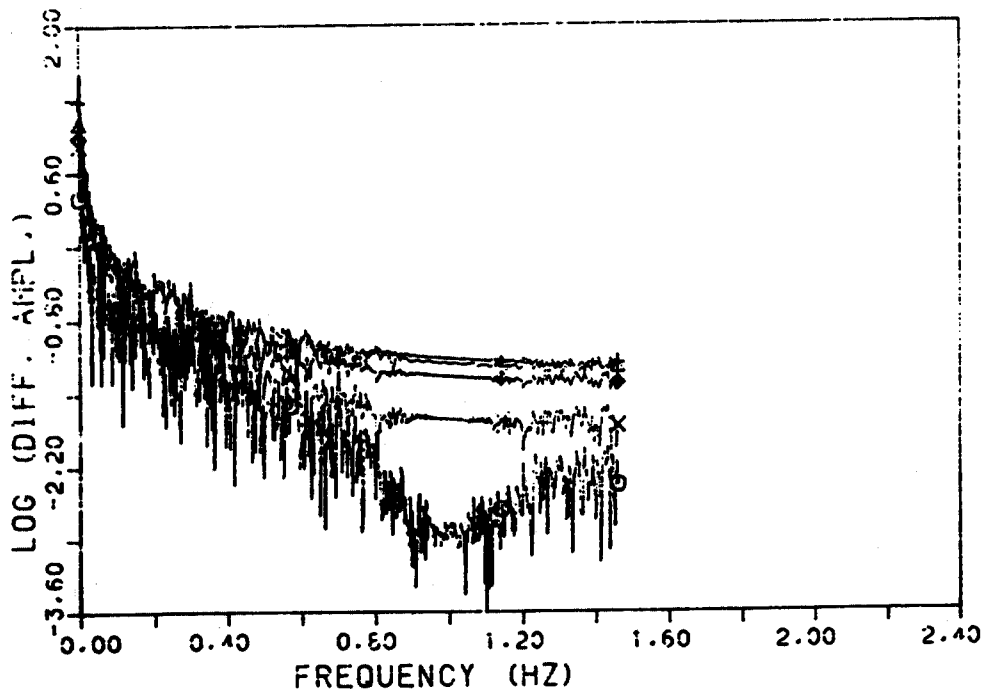


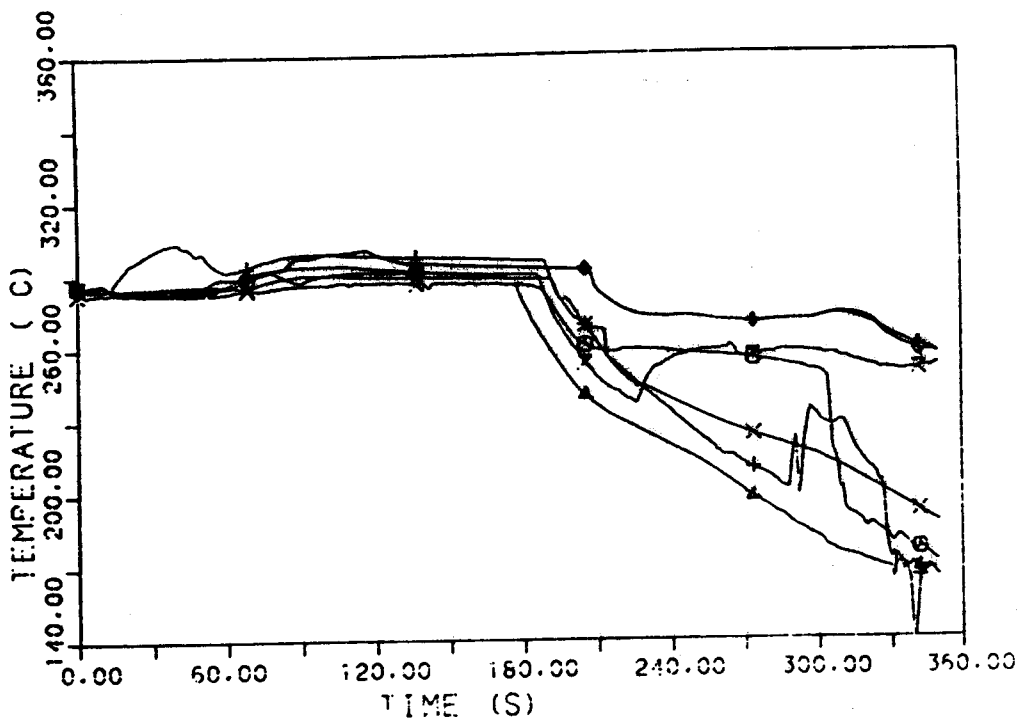
Fig. A.7 - Variable TF03 : amplitude of the FFT of the experimental trend



LEGENDA

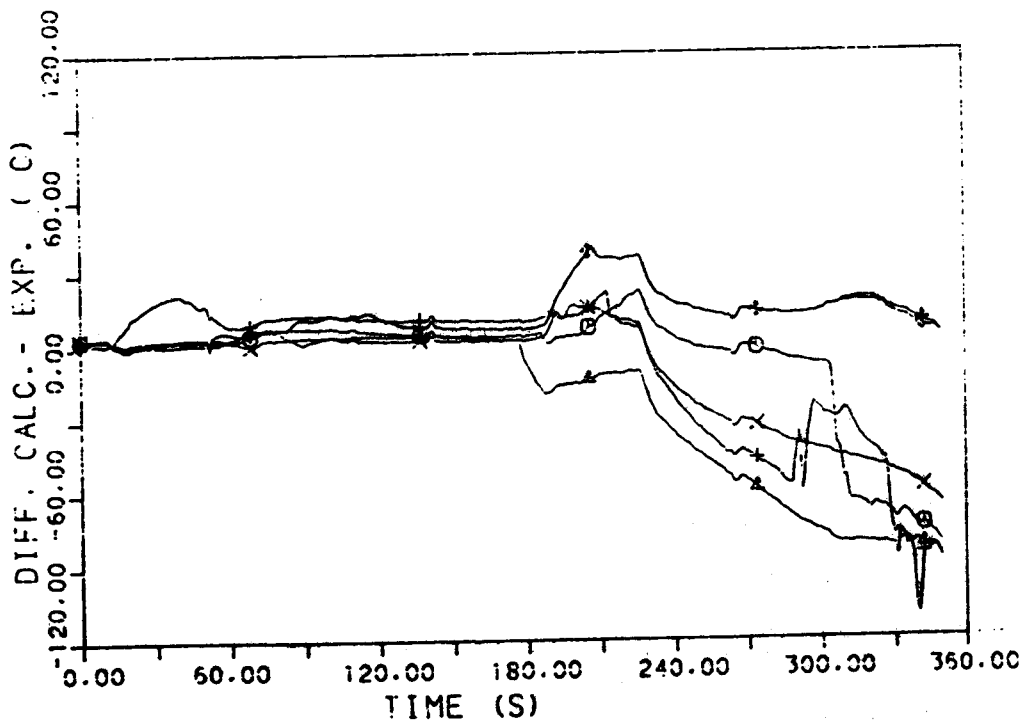
- ABB COBLIN-EM
- △ ANSALDO RELAP5/MOD2
- + ENEL RELAP4/MOD6
- × JAERI THYDE-B1/MOD2
- ◇ VIT SMABRE (1)
- + VIT SMABRE (1)

Fig. A.8 - Variable TF03 : amplitude of the FFT of the difference between calculated and experimental trends



- LEGENDA
- ABB COBLIN-EM
 - △ ANSALDO RELAP5/MOD2
 - + ENEL RELAP4/MOD5
 - × JAERI THYDE-B1/MOD2
 - ◇ VTT SMABRE (1)
 - + VTT SMABRE (2)
 - × EXP.

Fig. A.9 - Variable TF17 : experimental and calculated trends



- LEGENDA
- ABB COBLIN-EM
 - △ ANSALDO RELAP5/MOD2
 - + ENEL RELAP4/MOD5
 - × JAERI THYDE-B1/MOD2
 - ◇ VTT SMABRE (1)
 - + VTT SMABRE (2)

Fig. A.10 - Variable TF17 : difference between calculated and experimental trends

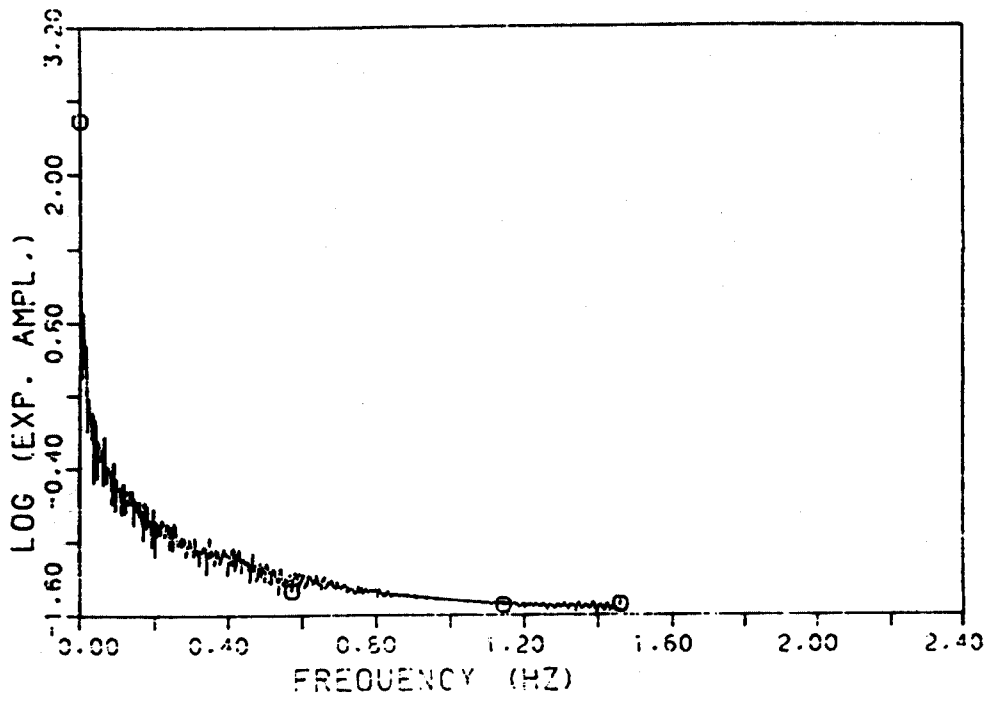
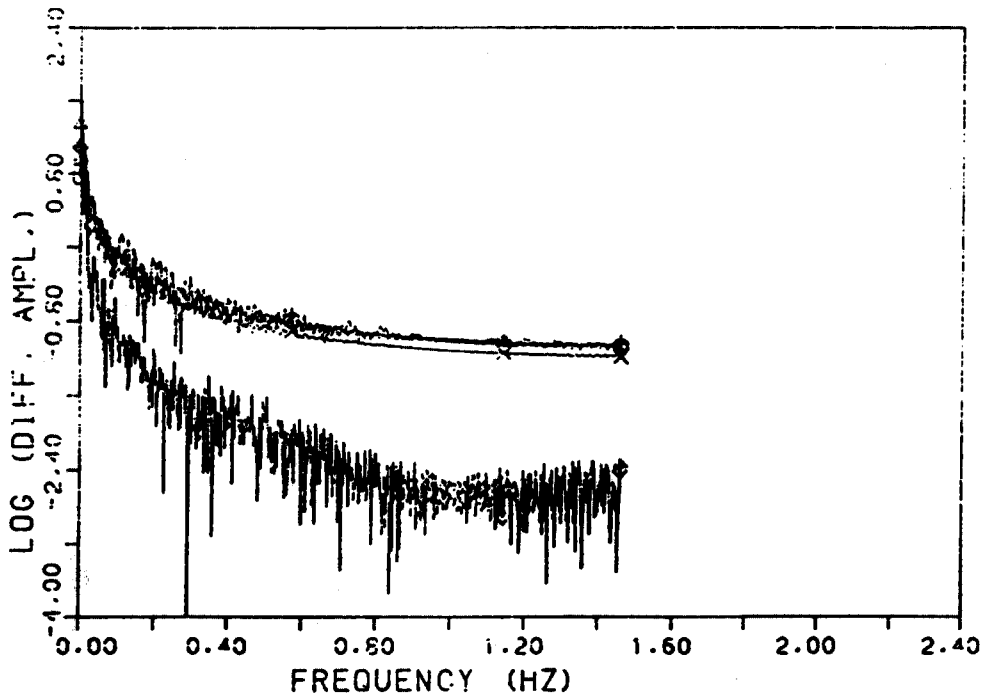
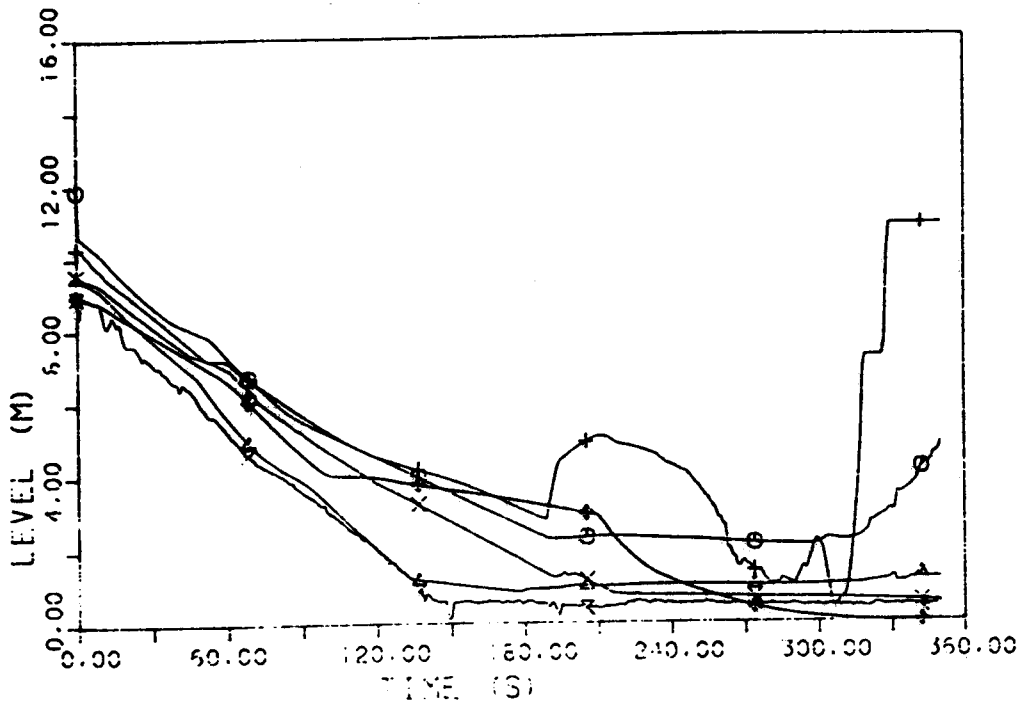


Fig. A.11 - Variable TF17 : amplitude of the FFT of the experimental trend



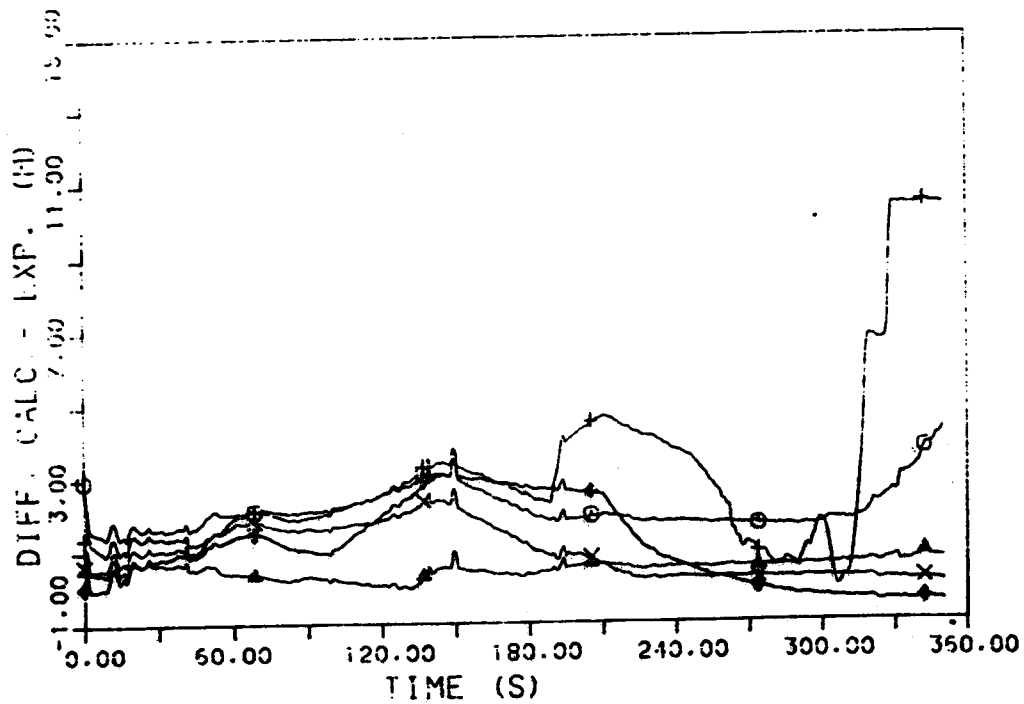
- LEGENDA
- ABB COELIN-EM
 - △ ANSALDO RELAP5/MOD2
 - + ENEL RELAP4/MOD6
 - × JAERI THYDE-B1/MOD2
 - ◇ VTT SMABRE (I)
 - ± VTT SMABRE (II)

Fig. A.12 - Variable TF17 : amplitude of the FFT of the difference between calculated and experimental trends



- LEGENDA
- ABB COBLIN-EM
 - △ ANSALDO RELAP5/MOD2
 - + ENEL RELAP4/MOD6
 - × JAERI THYDE-B1/MOD2
 - ◊ VTT SMABRE (1)
 - + VTT SMABRE (2)
 - × EXP.

Fig. A.13 - Variable CL70 : experimental and calculated trends



- LEGENDA
- ABB COBLIN-EM
 - △ ANSALDO RELAP5/MOD2
 - + ENEL RELAP4/MOD6
 - × JAERI THYDE-B1/MOD2
 - ◊ VTT SMABRE (1)
 - + VTT SMABRE (2)

Fig. A.14 - Variable CL70 : difference between calculated and experimental trends

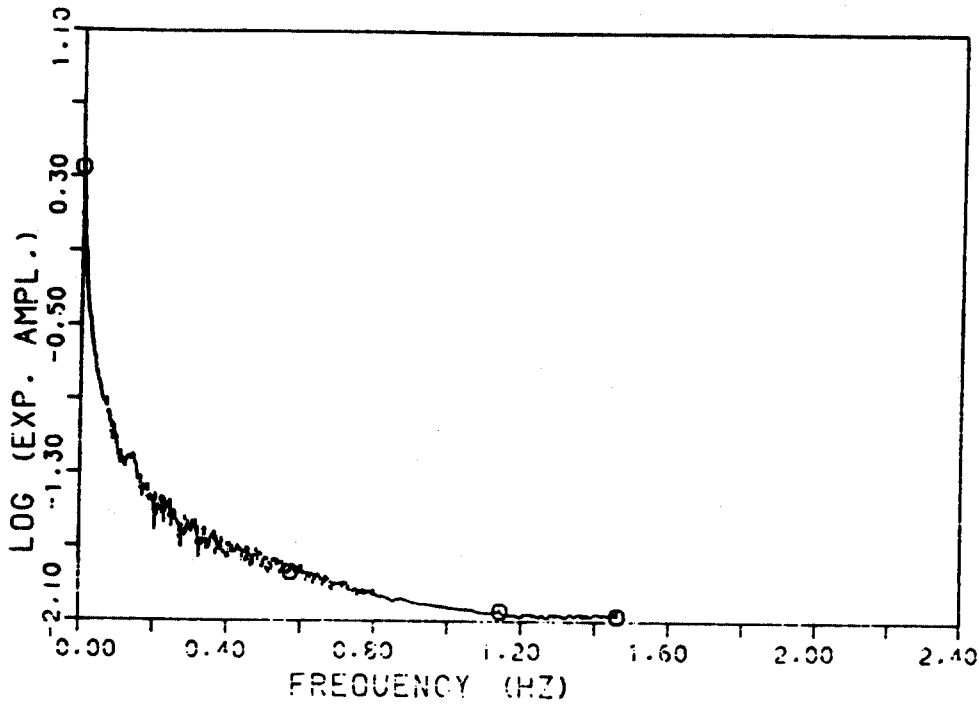
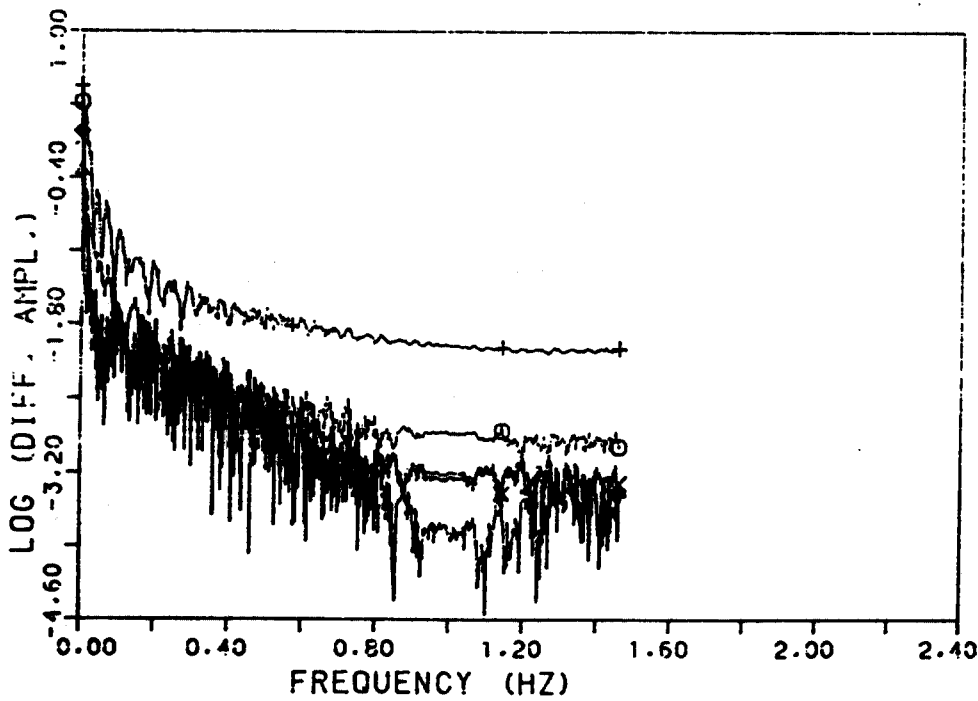


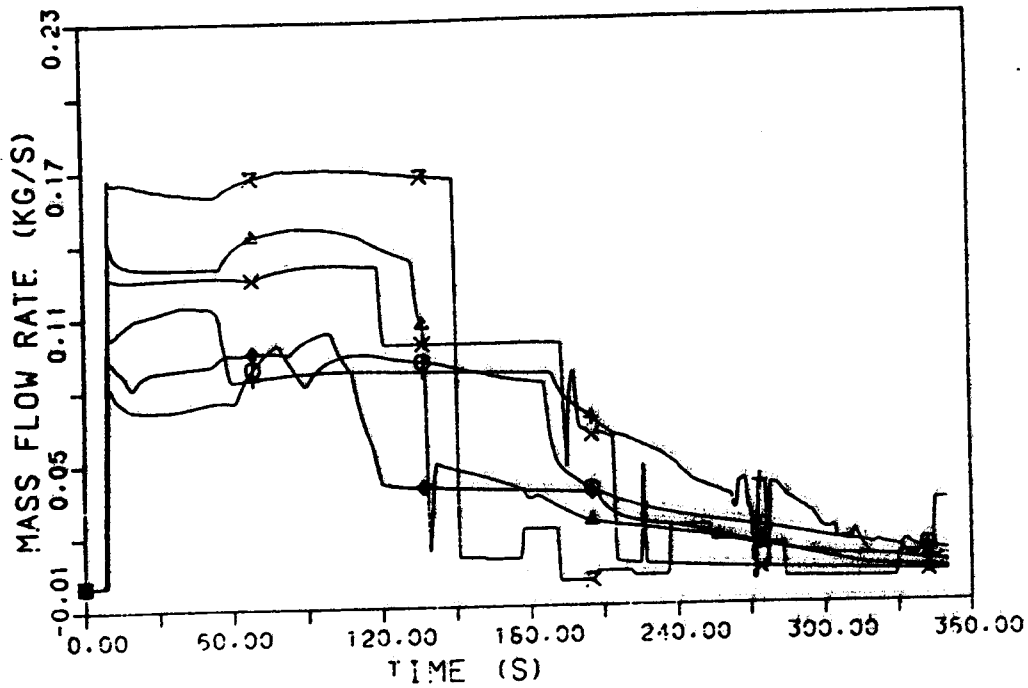
Fig. A.15 - Variable CL70 : amplitude of the FFT of the experimental trend



LEGENDA

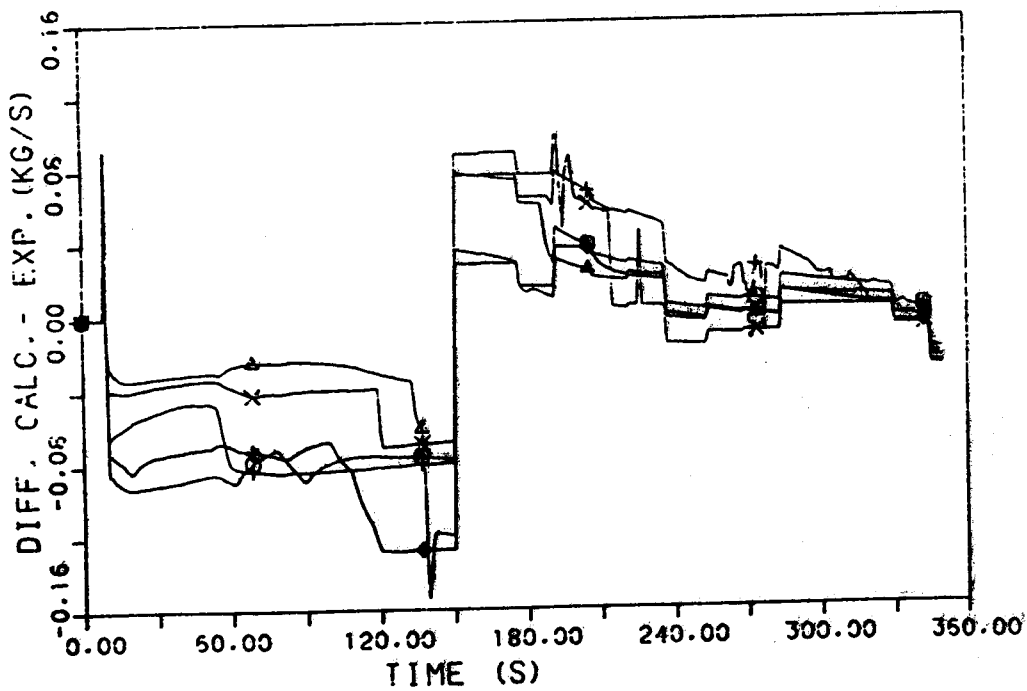
- ⊙ ABB GOBLIN-EM
- △ ANSALDO RELAP5/MOD2
- + ENEL RELAP4/MOD6
- × JAERI THYDE-B1/MOD2
- ◇ VIT SMABRE (1)
- ⊕ VIT SMABRE (1)

Fig. A.16 - Variable CL70 : amplitude of the FFT of the difference between calculated and experimental trends



- LEGENDA
- ABB GOBLIN-EM
 - △ ANSALDO RELAP5/MOD2
 - + ENEL RELAP4/MOD5
 - × JAERI THYDE-B1/MOD2
 - ◇ VTT SMABRE (1)
 - ↑ VTT SMABRE (2)
 - × EXP.

Fig. A.17 - Variable MF43 : experimental and calculated trends



- LEGENDA
- ABB GOBLIN-EM
 - △ ANSALDO RELAP5/MOD2
 - + ENEL RELAP4/MOD5
 - × JAERI THYDE-B1/MOD2
 - ◇ VTT SMABRE (1)
 - ↑ VTT SMABRE (2)

Fig. A.18 - Variable MF43 : difference between calculated and experimental trends

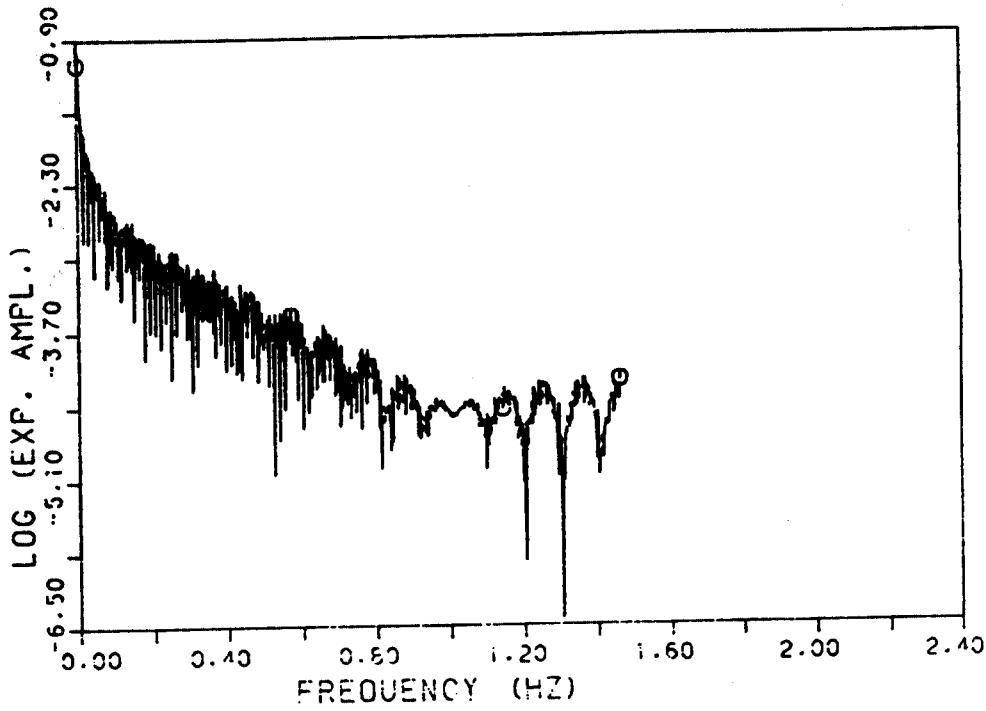


Fig. A.19 - Variable MF43 : amplitude of the FFT of the experimental trend

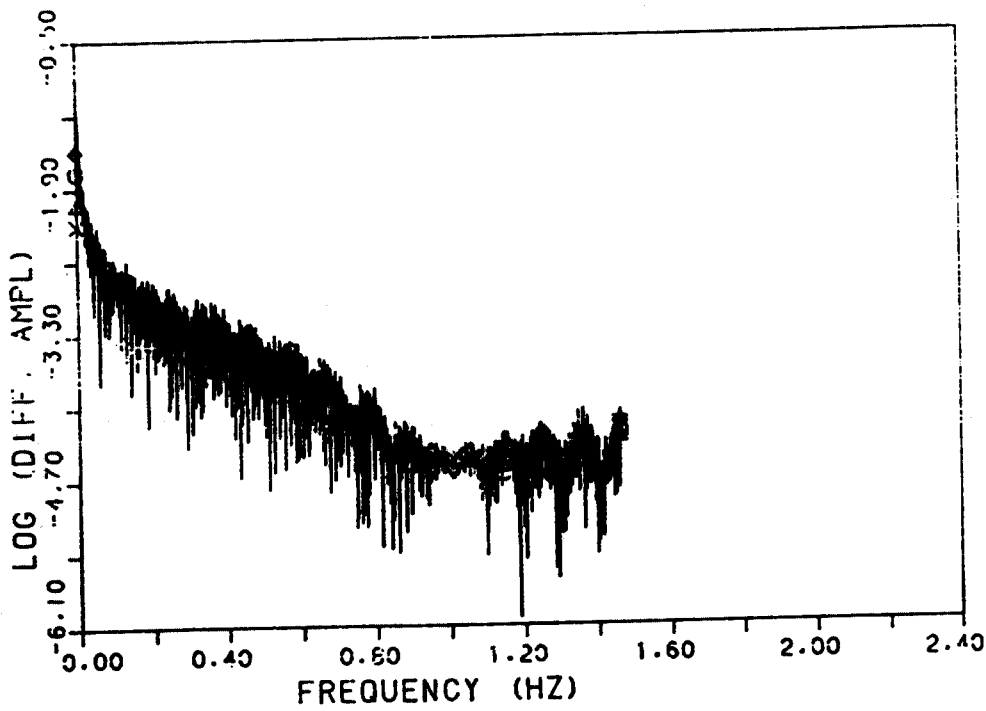
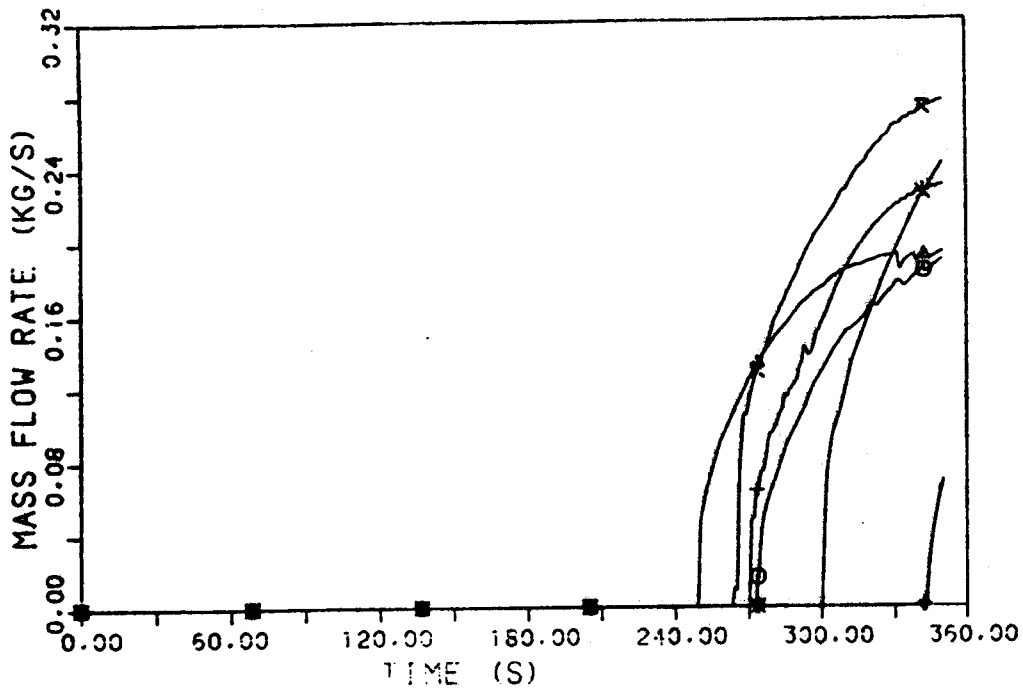


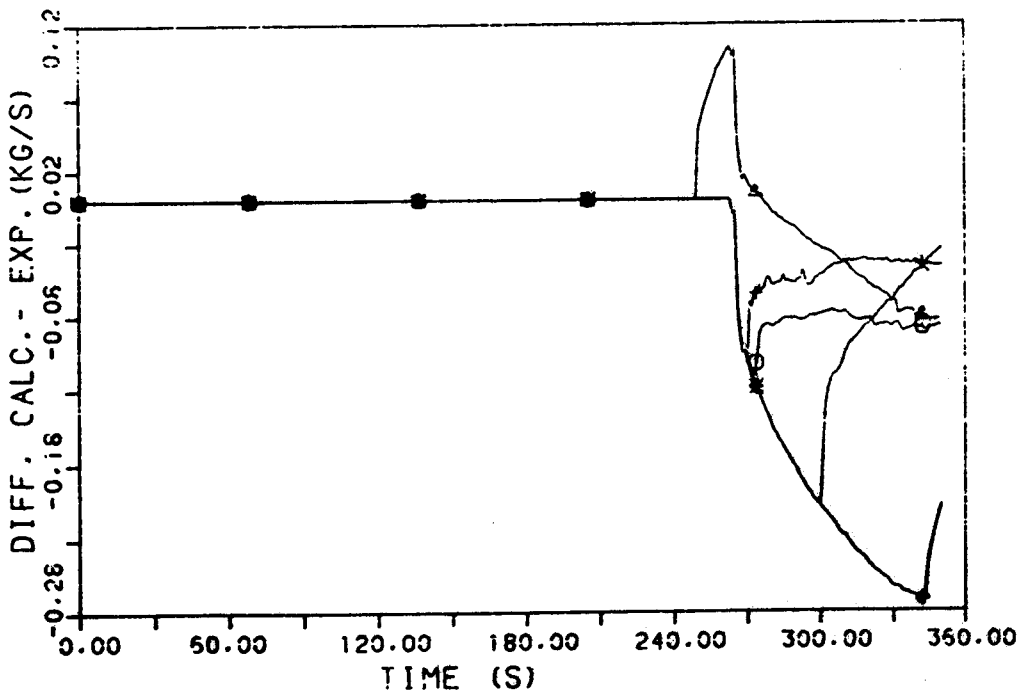
Fig. A.20 - Variable MF43 : amplitude of the FFT of the difference between calculated and experimental trends

- LEGENDA
- ⊙ ABS COBLIN-EM
 - △ ANSALDO RELAP5/MOD2
 - + ENEL RELAP4/MOD5
 - × JAERI THYDE-B1/MOD2
 - ◇ VTT SMABRE (1)
 - ⇨ VTT SMABRE (1)



- LEGENDA
- ABS GOBLIN-EM
 - △ ANSALDO RELAP5/MOD2
 - + ENEL RELAP4/MOD5
 - × JAERI THYDE-B1/MOD2
 - ◇ VTT SMABRE (1)
 - ↑ VTT SMABRE (2)
 - × EXP.

Fig. A.21 - Variable MF48 : experimental and calculated trends



- LEGENDA
- ABS GOBLIN-EM
 - △ ANSALDO RELAP5/MOD2
 - + ENEL RELAP4/MOD5
 - × JAERI THYDE-B1/MOD2
 - ◇ VTT SMABRE (1)
 - ↑ VTT SMABRE (2)

Fig. A.22 - Variable MF48 : difference between calculated and experimental trends

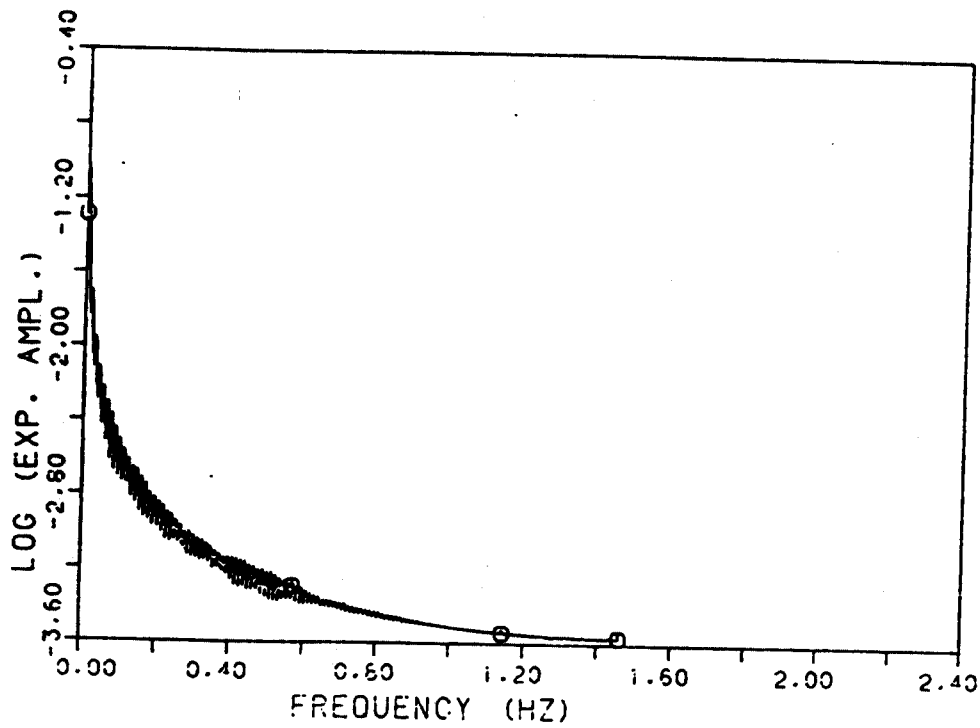
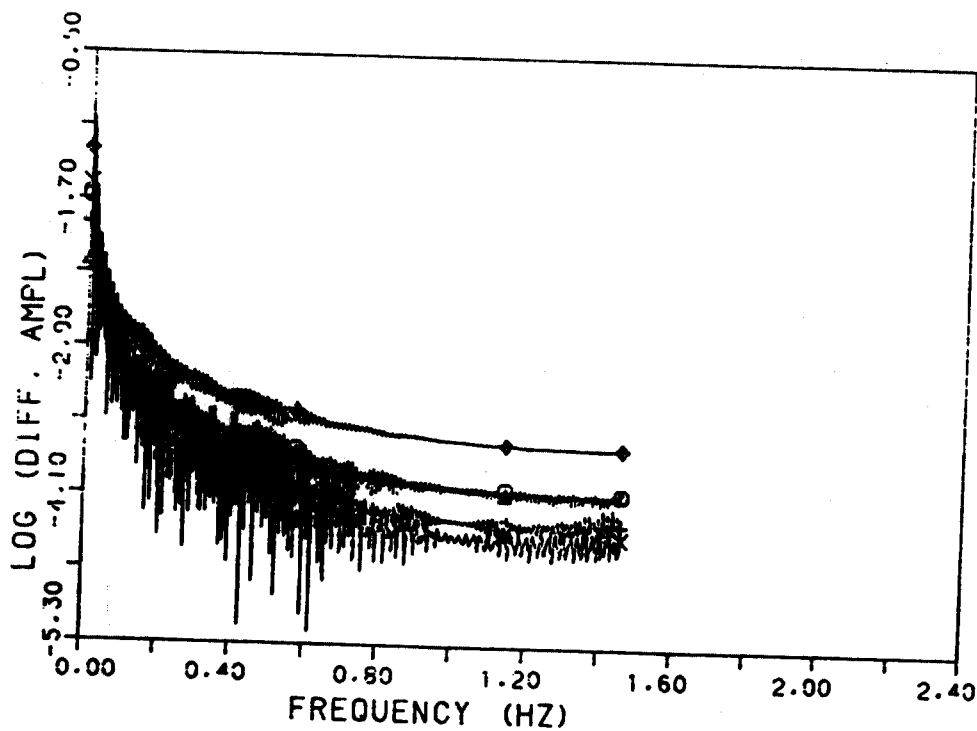


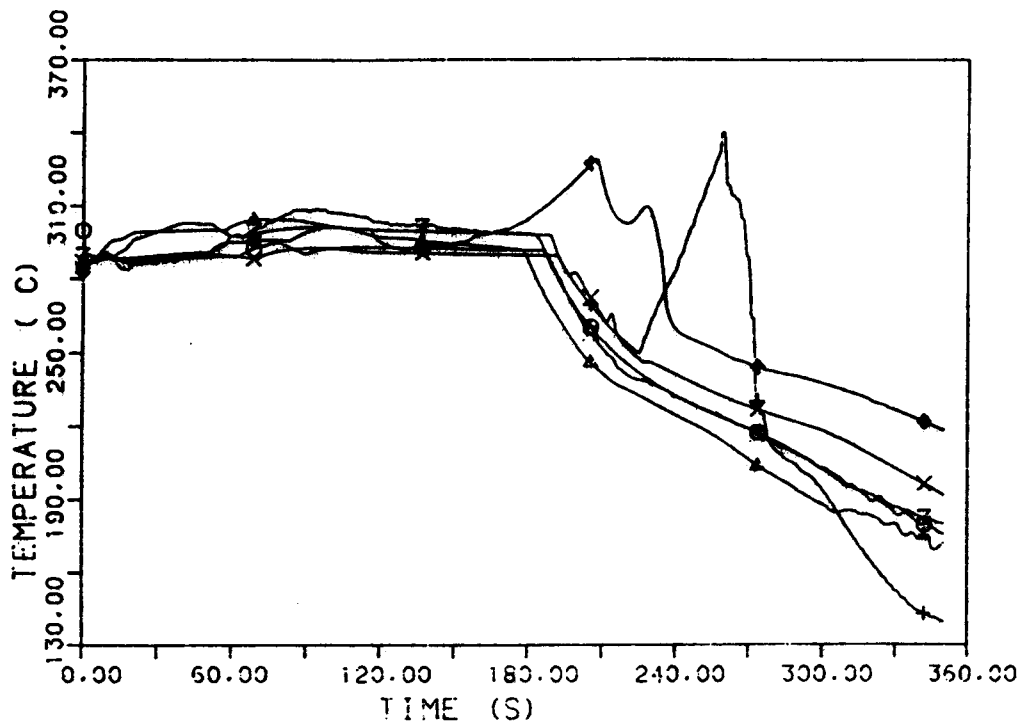
Fig. A.23 - Variable MF48 : amplitude of the FFT of the experimental trend



LEGENDA

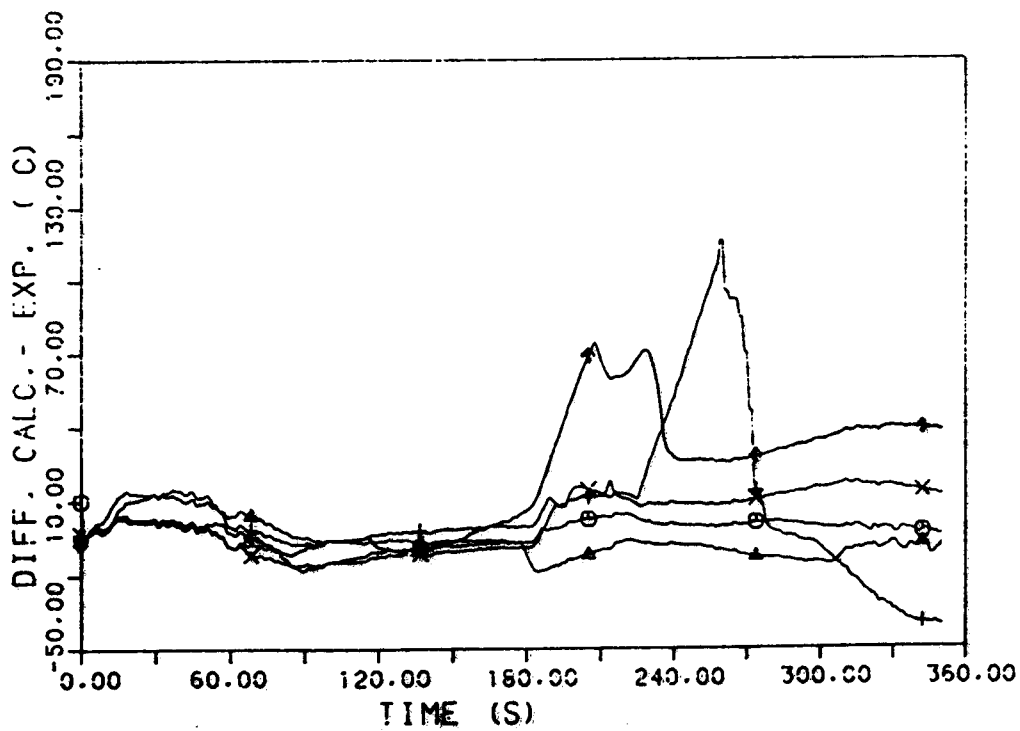
- ABS COSLIN-EM
- △ ANSALDO RELAP5/MOD2
- + ENEL RELAP4/MOD6
- × JAERT THYDE-B1/MOD2
- ◇ VTI SMABRE (1)
- ⊕ VTI SMABRE (1)

Fig. A.24 - Variable MF48 : amplitude of the FFT of the difference between calculated and experimental trends



- LEGENDA
- ABB GOBLIN-EM
 - △ ANSALDO RELAP5/MOD2
 - + ENEL RELAP4/MOD6
 - × JAERI THYDE-B1/MOD2
 - ◇ VTT SMABRE (1)
 - ↑ VTT SMABRE (2)
 - × EXP.

Fig. A.25 - Variable TR50 : experimental and calculated trends



- LEGENDA
- ABB GOBLIN-EM
 - △ ANSALDO RELAP5/MOD2
 - + ENEL RELAP4/MOD6
 - × JAERI THYDE-B1/MOD2
 - ◇ VTT SMABRE (1)
 - ↑ VTT SMABRE (2)

Fig. A.26 - Variable TR50 : difference between calculated and experimental trends

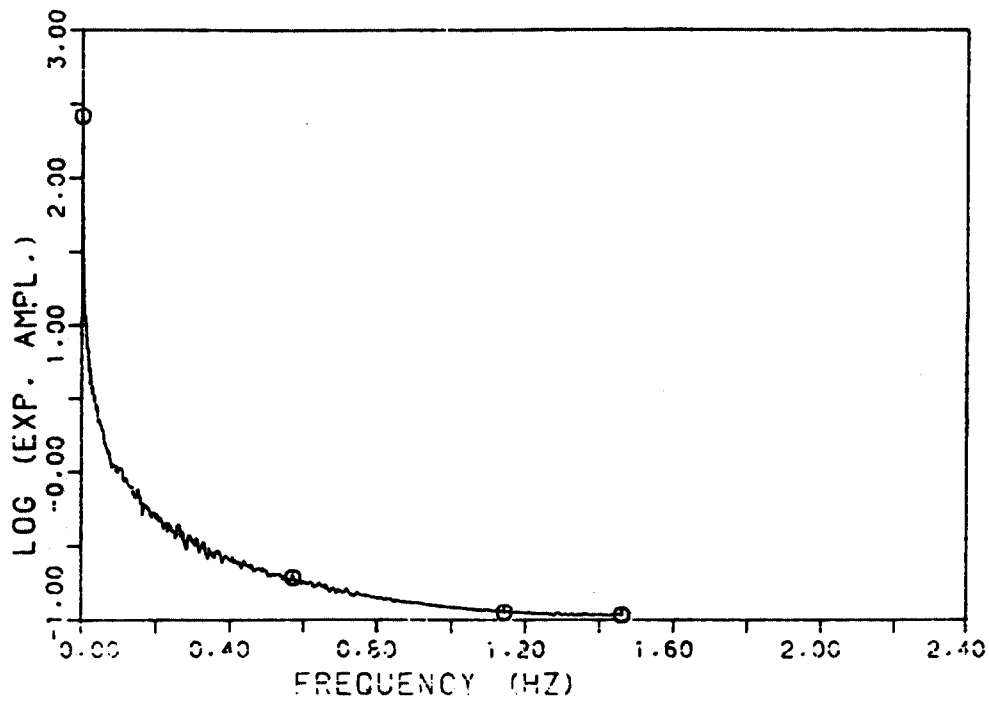
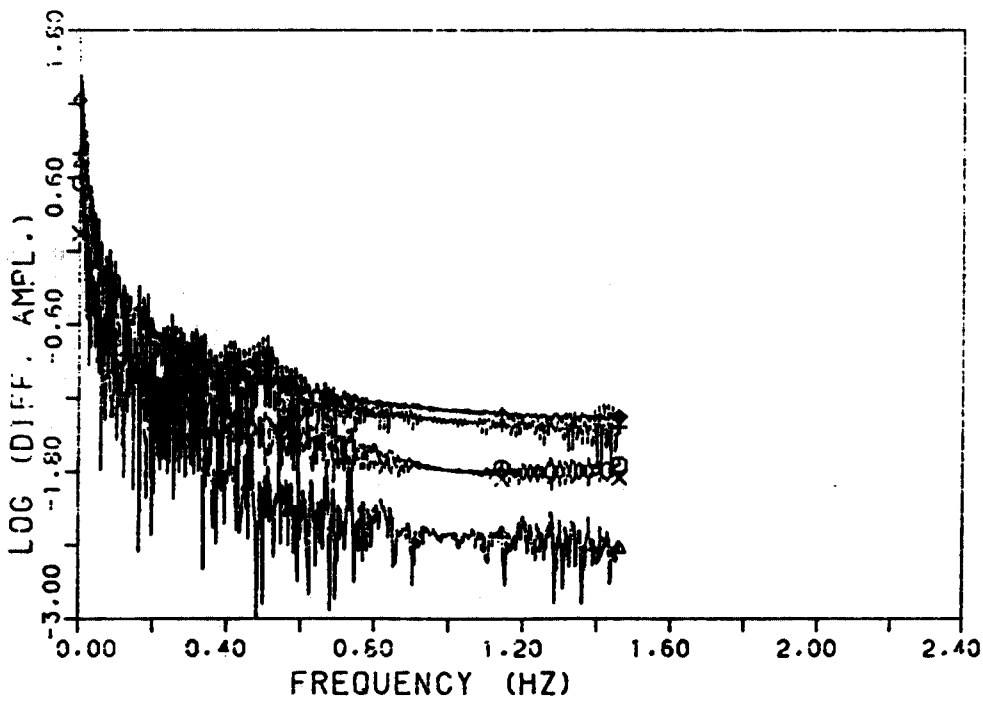


Fig. A.27 - Variable TR50 : amplitude of the FFT of the experimental trend



LEGENDA

- ⊙ ABS GOBLIN-EM
- △ ANSALDO RELAP5/MOD2
- + ENEL RELAP4/MOD6
- × JAERI THYDE-B1/MOD2
- ◇ VTT SMABRE (1)
- ‡ VTT SMABRE (1)

Fig. A.28 - Variable TR50 : amplitude of the FFT of the difference between calculated and experimental trends

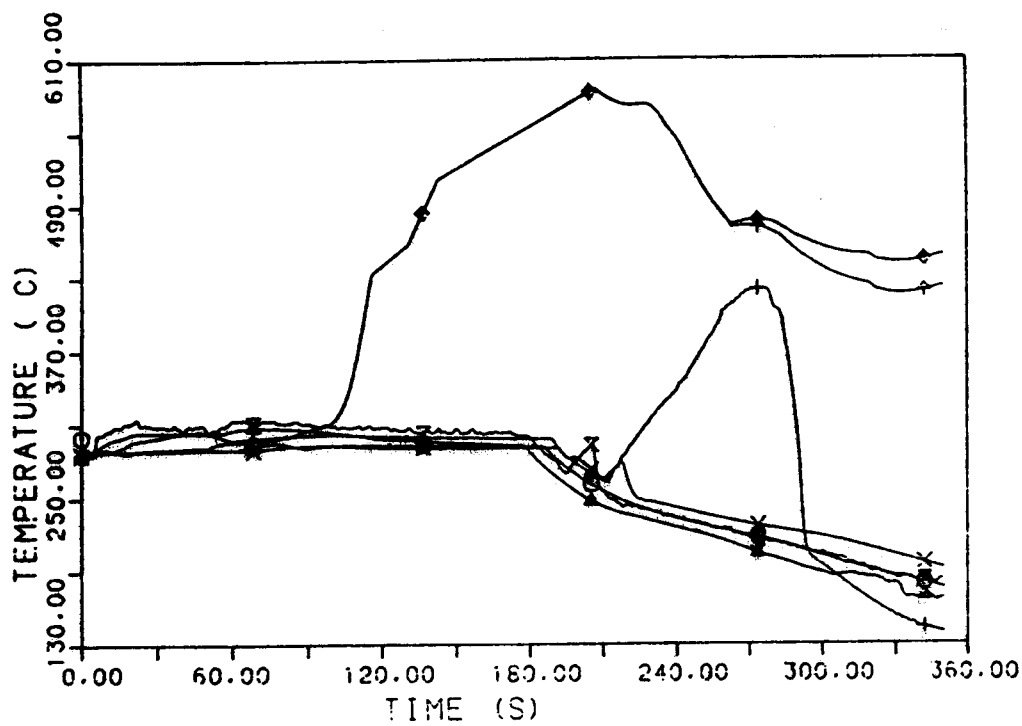


Fig. A.29 - Variable TR52 : experimental and calculated trends

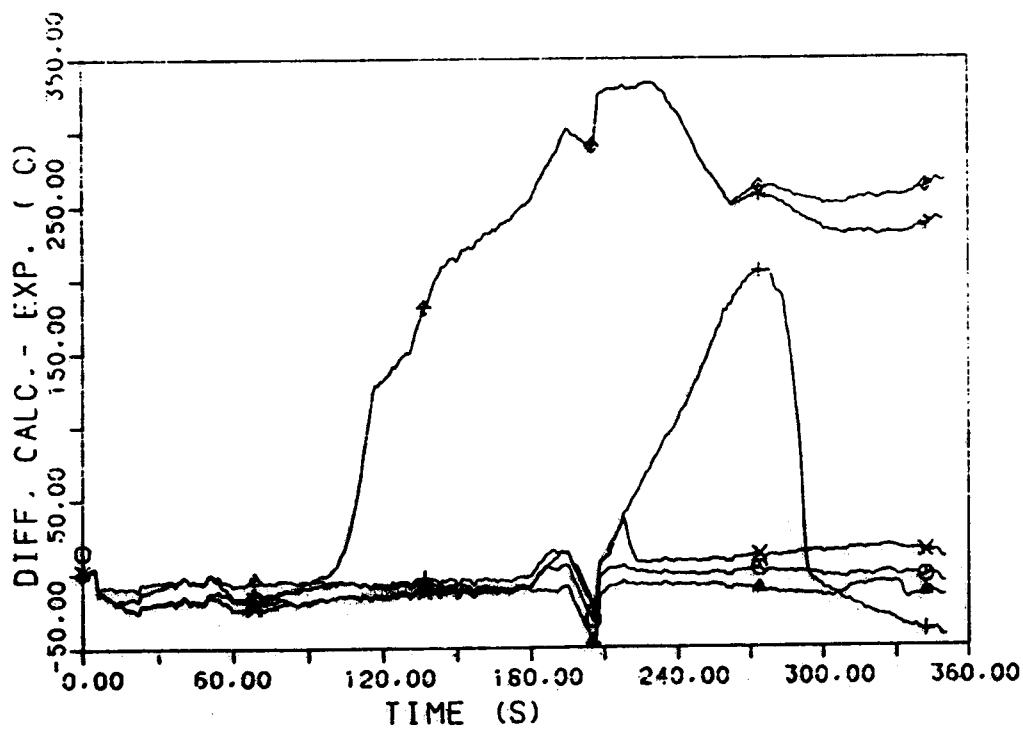


Fig. A.30 - Variable TR52 : difference between calculated and experimental trends

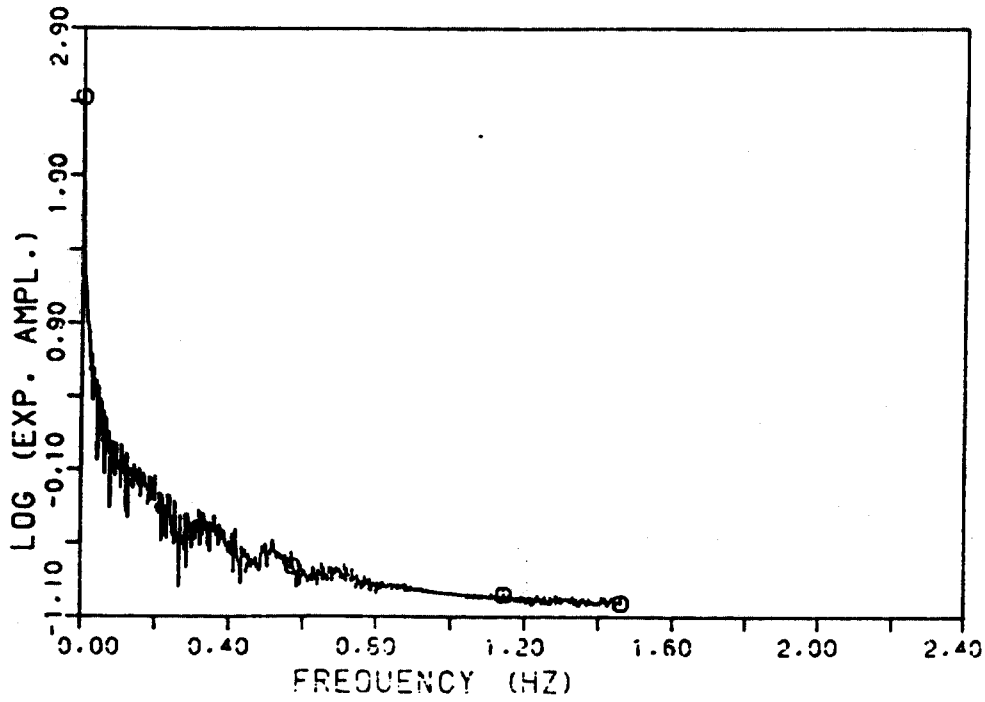
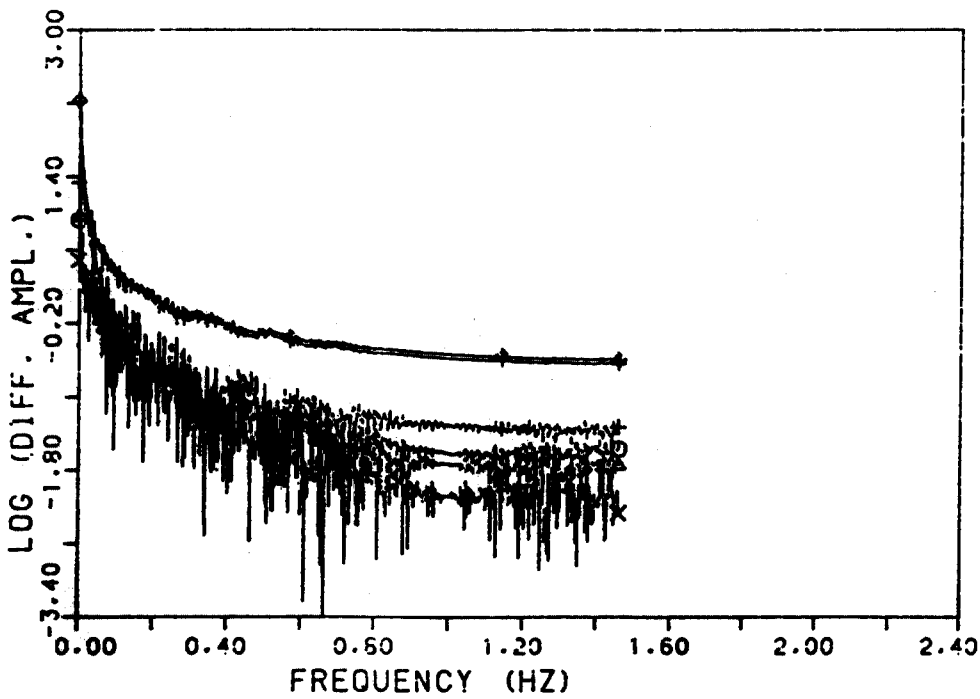


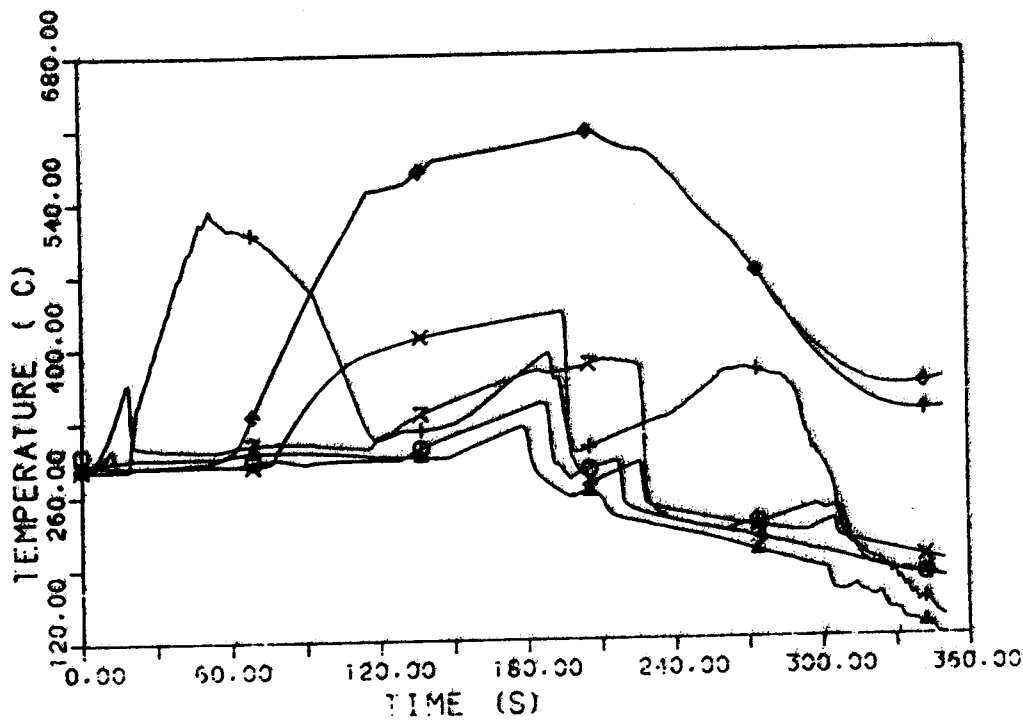
Fig. A.31 - Variable TR52 : amplitude of the FFT of the experimental trend



LEGENDA

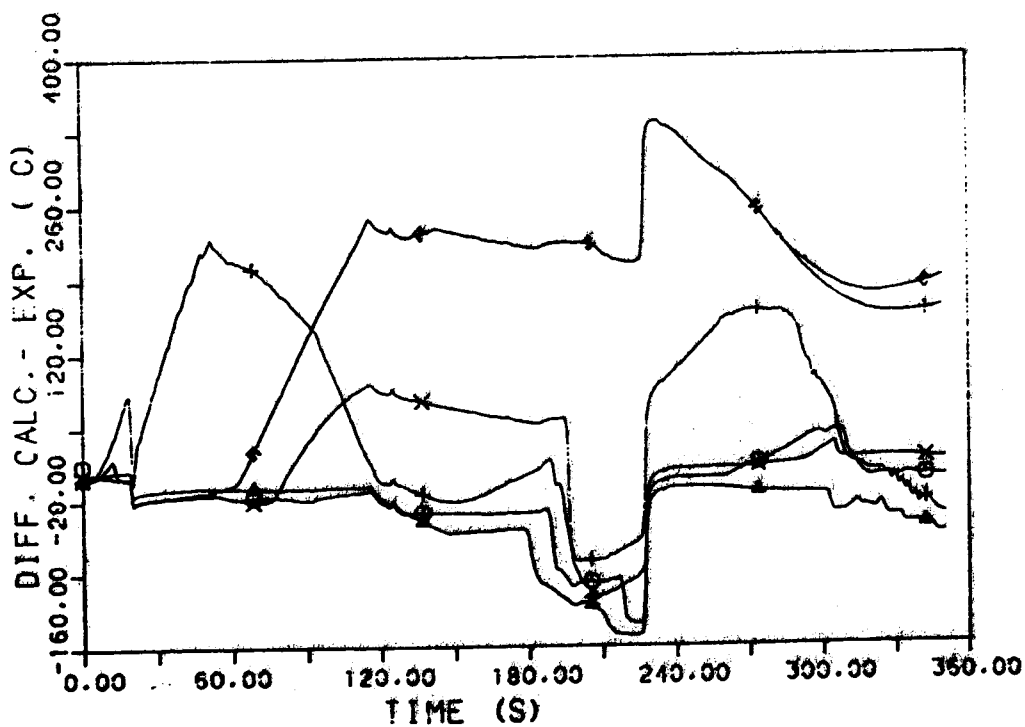
- ABB GOBLIN-EM
- △ ANSALDO RELAP5/MOD2
- + ENEL RELAP4/MOD6
- × JAERI THYDE-B1/MOD2
- ◇ VTT SMABRE (1)
- ♠ VTT SMABRE (1)

Fig. A.32 - Variable TR52 : amplitude of the FFT of the difference between calculated and experimental trends



- LEGENDA
- ABB GOBLIN-EM
 - △ ANSALDO RELAP5/MOD2
 - + ENEL RELAP4/MOD6
 - × JAERI THYDE-B1/MOD2
 - ◇ VTT SMABRE (1)
 - + VTT SMABRE (2)
 - z EXP.

Fig. A.33 - Variable TR55 : experimental and calculated trends

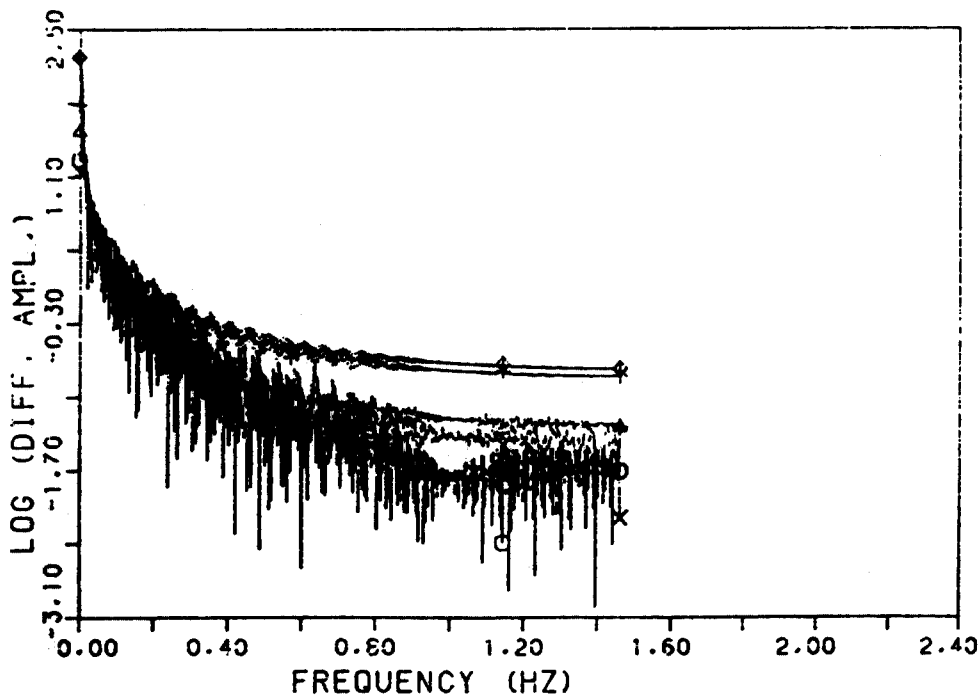


- LEGENDA
- ABB GOBLIN-EM
 - △ ANSALDO RELAP5/MOD2
 - + ENEL RELAP4/MOD6
 - × JAERI THYDE-B1/MOD2
 - ◇ VTT SMABRE (1)
 - + VTT SMABRE (2)

Fig. A.34 - Variable TR55 : difference between calculated and experimental trends



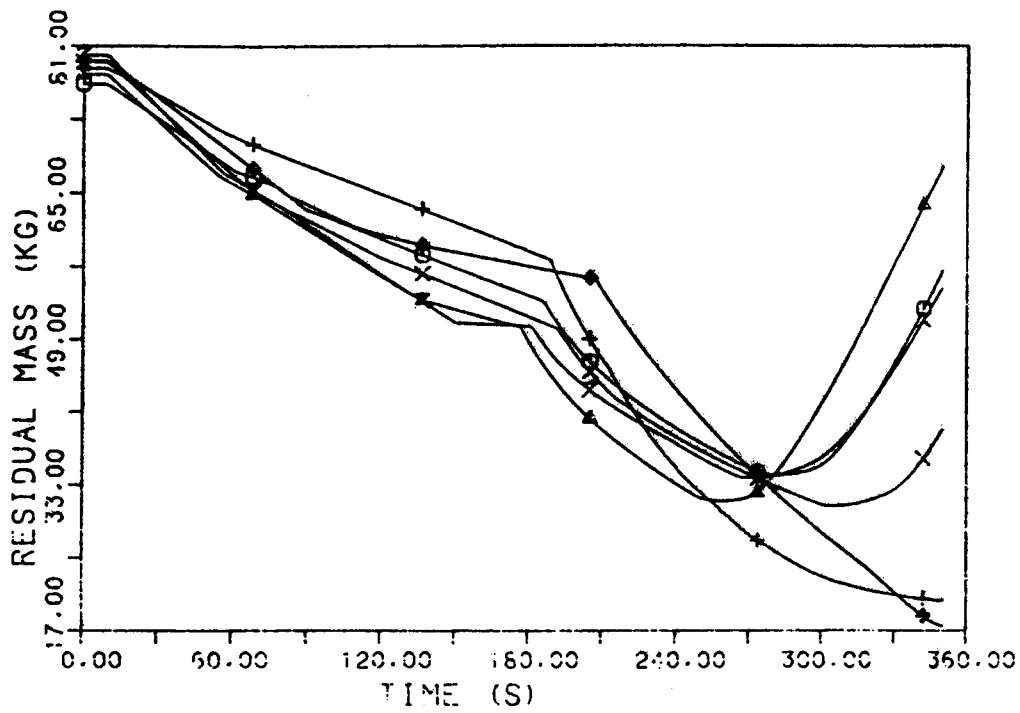
Fig. A.35 - Variable TR55 : amplitude of the FFT of the experimental trend



LEGENDA

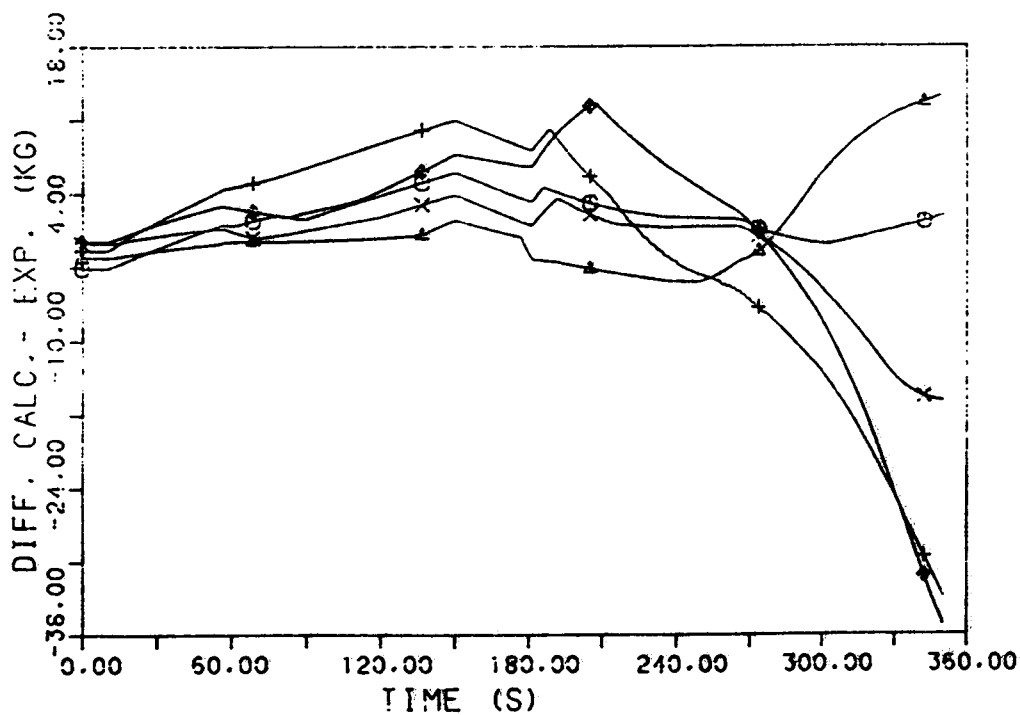
- ABB COBLIN-EM
- △ ANSALDO RELAP5/MOD2
- + ENEL RELAP4/MOD6
- × JAERI THYDE-B1/MOD2
- ◊ VTT SMABRE (1)
- ⊕ VTT SMABRE (1)

Fig. A.38 - Variable TR55 : amplitude of the FFT of the difference between calculated and experimental trends



- LEGENDA
- ABB GOBLIN-EM
 - △ ANGALDO RELAP5/MOD2
 - + ENEL RELAP4/MOD5
 - × JAERI THYDE-B1/MOD2
 - ◇ VTT SMABRE (1)
 - ↑ VTT SMABRE (2)
 - × EXP.

Fig. A.37 - Variable RM65 : experimental and calculated trends



- LEGENDA
- ABB GOBLIN-EM
 - △ ANGALDO RELAP5/MOD2
 - + ENEL RELAP4/MOD5
 - × JAERI THYDE-B1/MOD2
 - ◇ VTT SMABRE (1)
 - ↑ VTT SMABRE (2)

Fig. A.38 - Variable RM65 : difference between calculated and experimental trends

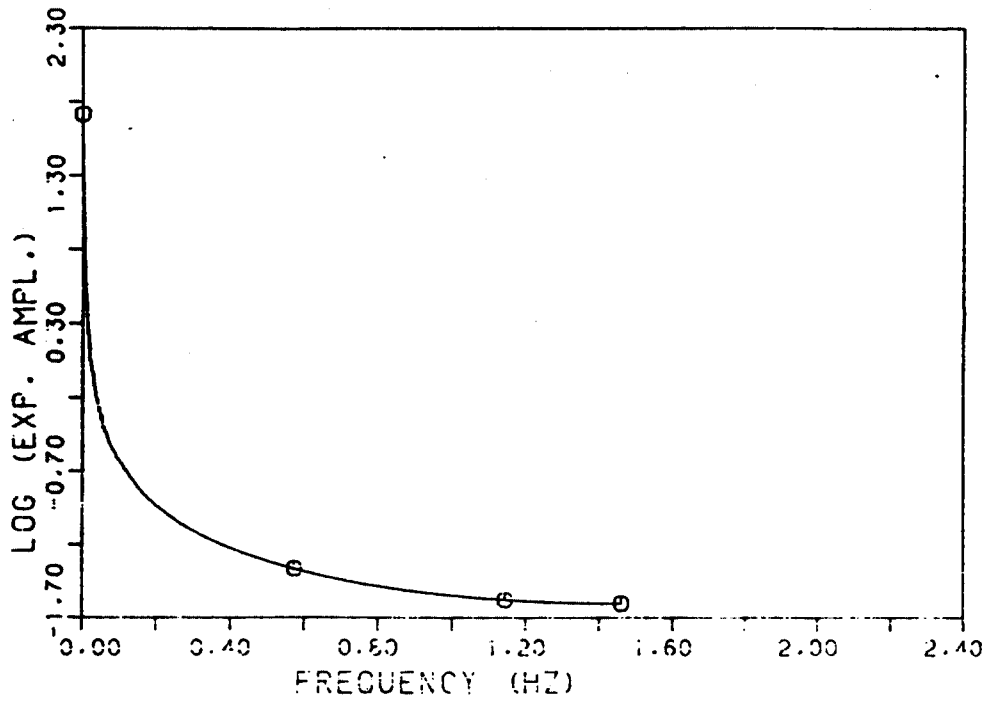
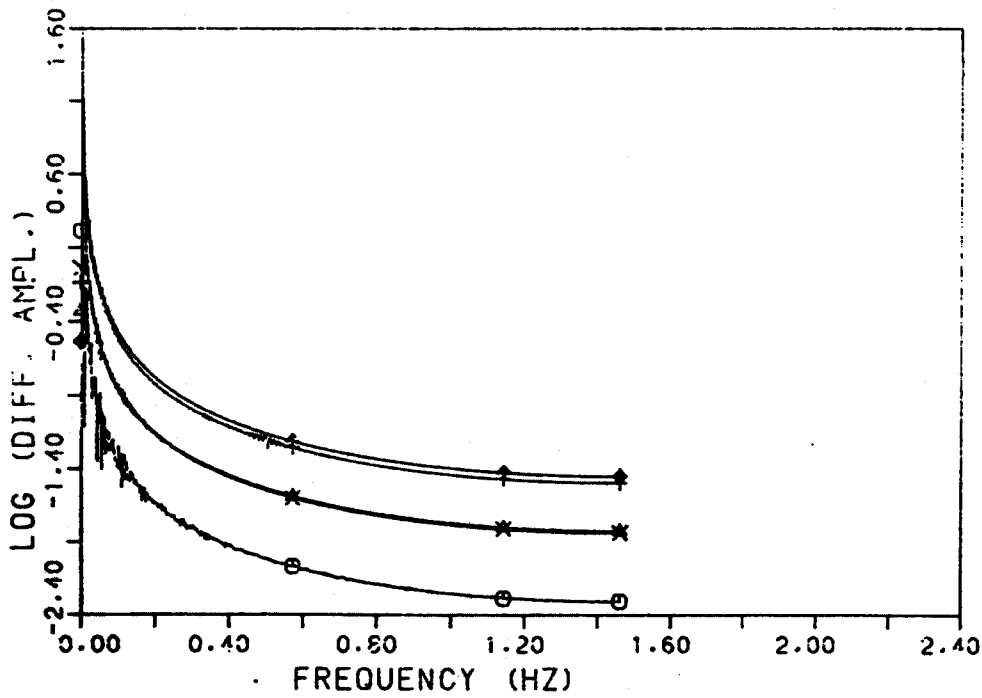


Fig. A.39 - Variable RM65 : amplitude of the FFT of the experimental trend



LEGENDA

- ABB COBLIN-EM
- △ ANSALDO RELAP5/MOD2
- + ENEL RELAP4/MOD6
- × JAERI THYDE-B1/MOD2
- ◇ VTT SMABRE (1)
- † VTT SMABRE (2)

Fig. A.40 - Variable RM65 : amplitude of the FFT of the difference between calculated and experimental trends

APPENDIX B - Figures concerning DCMN post-test calculation

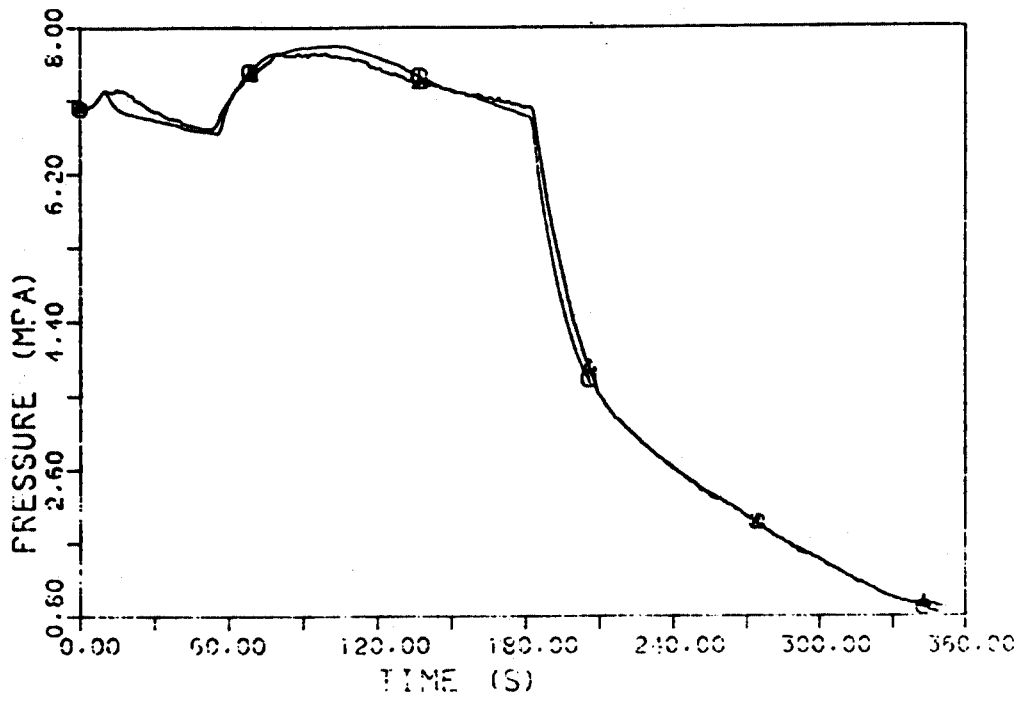


Fig. B.1 - Variable PA01 : experimental and calculated trends

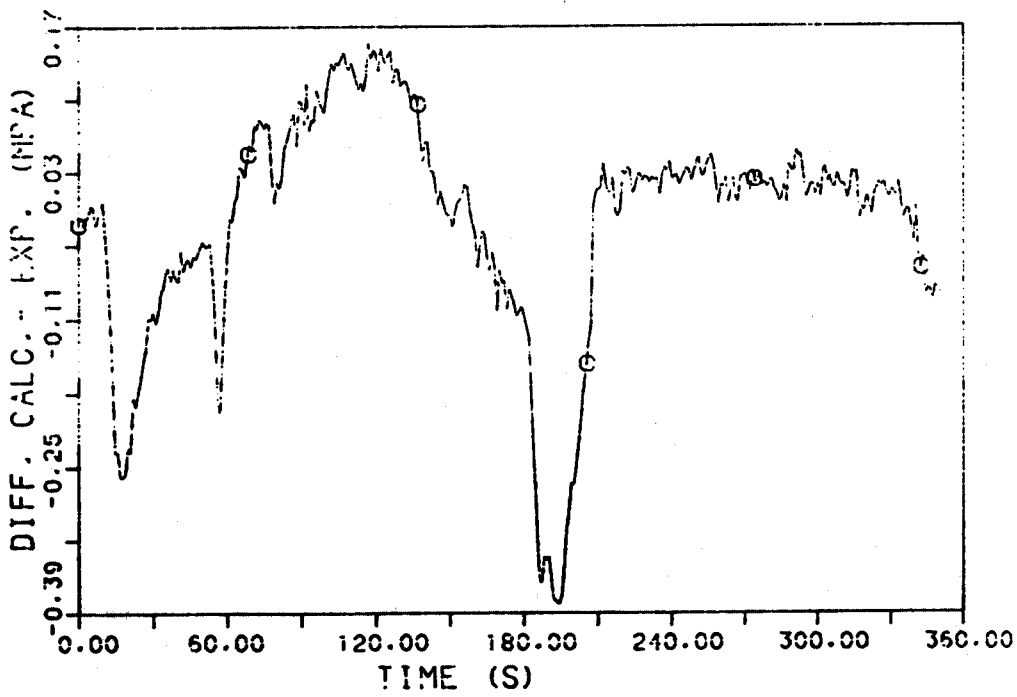


Fig. B.2 - Variable PA01 : difference between calculated and experimental trends

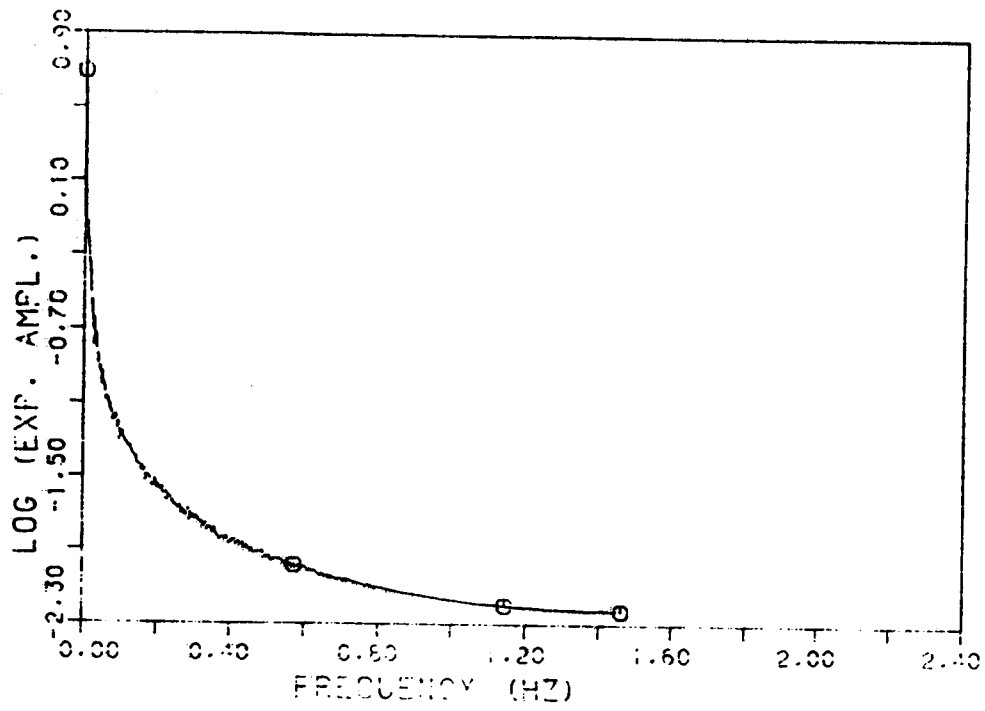


Fig. B.3 - Variable PA01 : amplitude of the FFT of the experimental trend

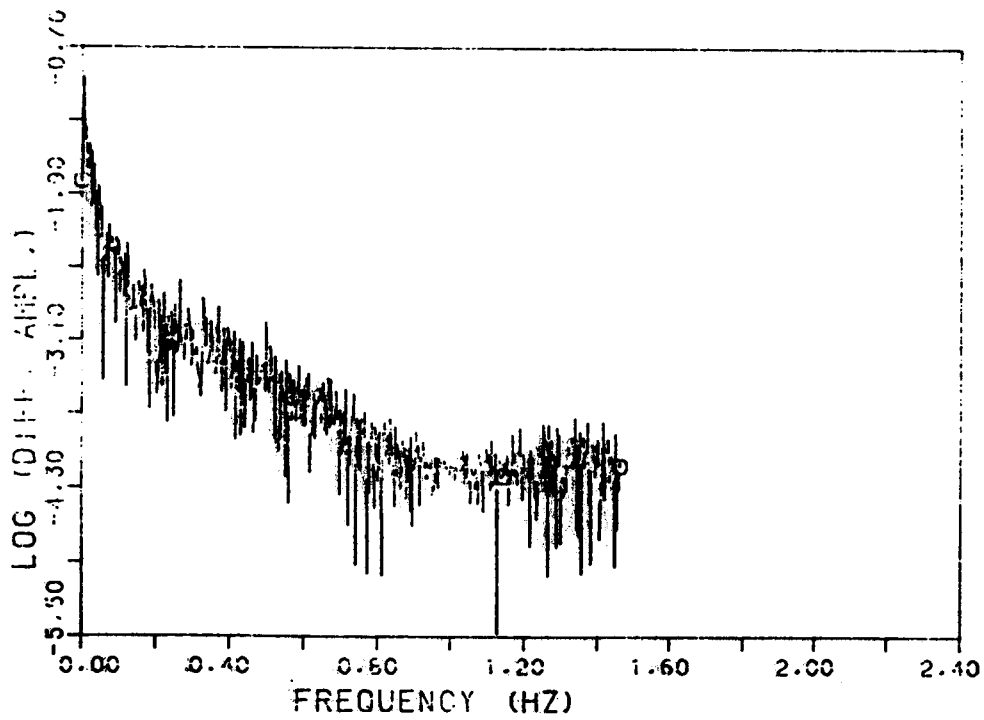
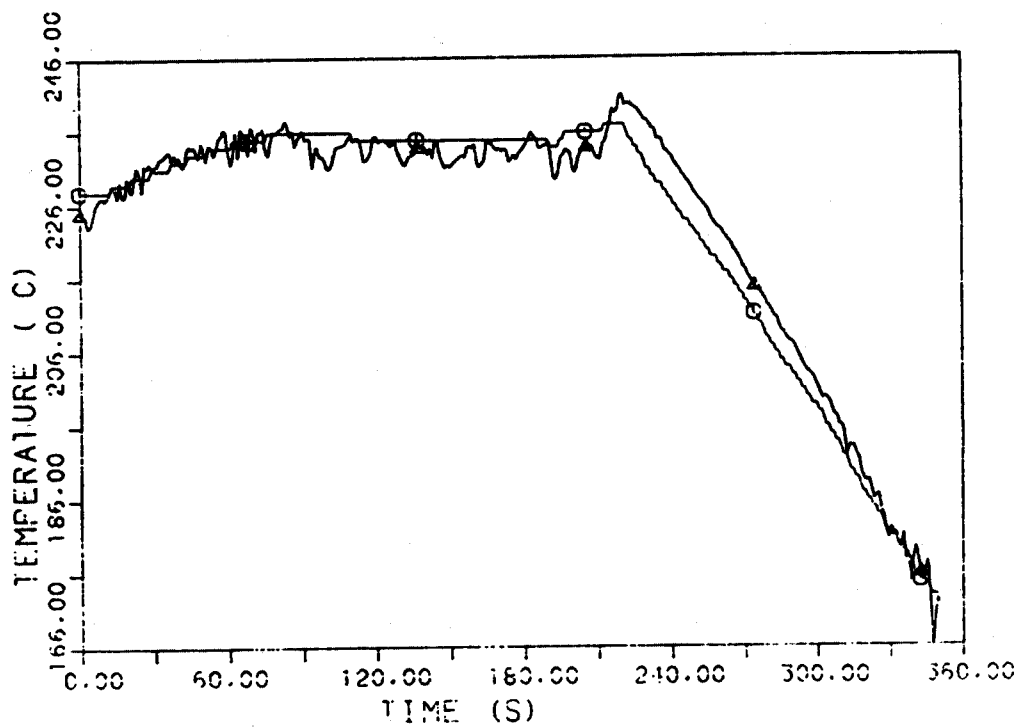


Fig. B.4 - Variable PA01 : amplitude of the FFT of the difference between calculated and experimental trends



LEGENDA
 ○ DGMN RELAP5/MOD2 (P.T.)
 ▲ EXP.

Fig. B.5 - Variable TF03 : experimental and calculated trends

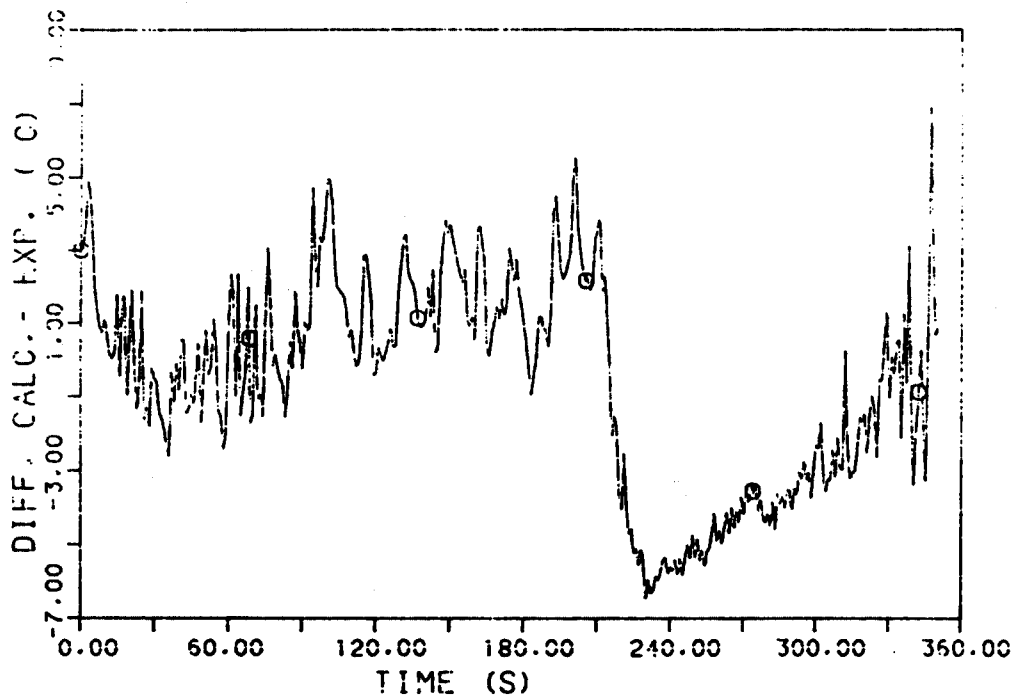


Fig. B.6 - Variable TF03 : difference between calculated and experimental trends

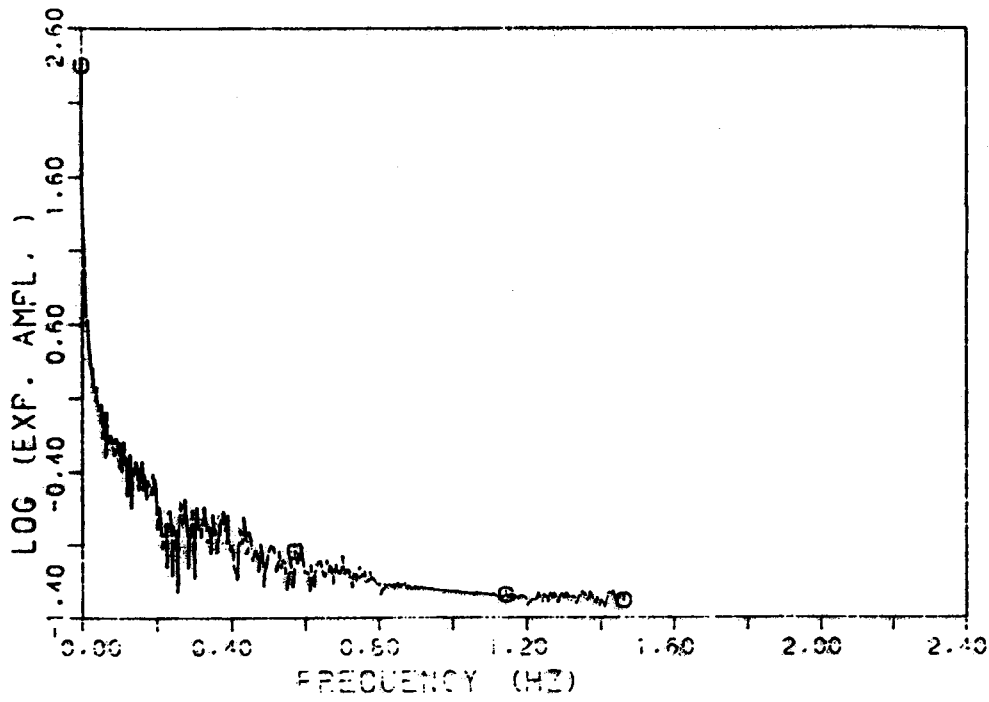


Fig. B.7 - Variable TF03 : amplitude of the FFT of the experimental trend

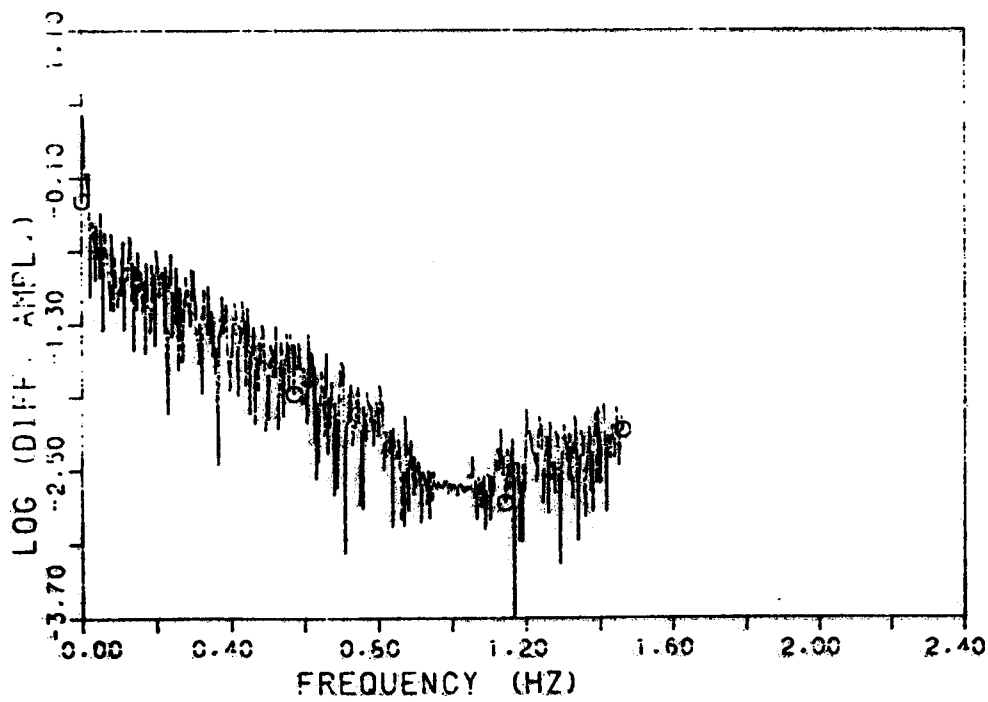
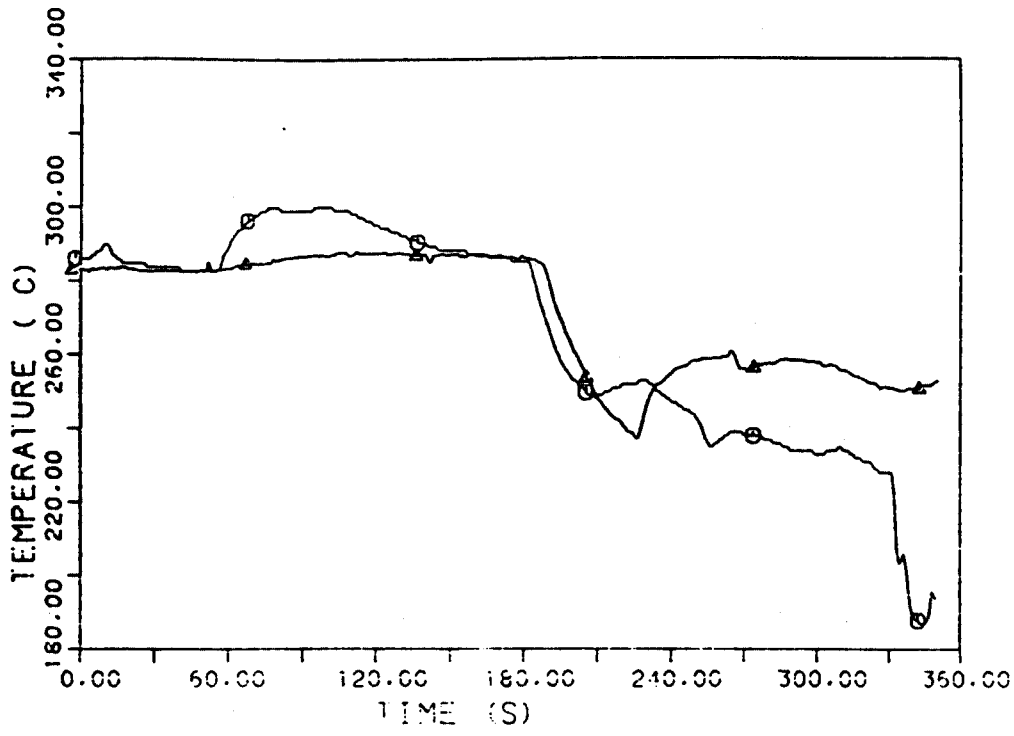


Fig. B.8 - Variable TF03 : amplitude of the FFT of the difference between calculated and experimental trends



LEGENDA
 ○DCMN RELAP5/MCS2 (P.T.)
 △EXP.

Fig. B.9 - Variable TF17 : experimental and calculated trends

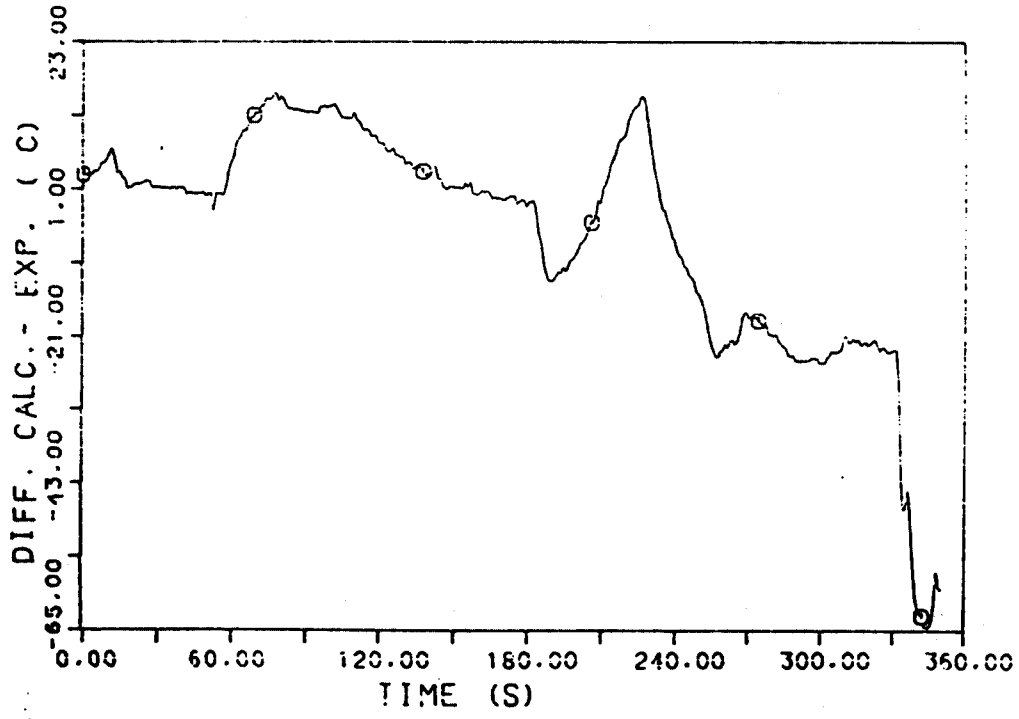


Fig. B.10 - Variable TF17 : difference between calculated and experimental trends

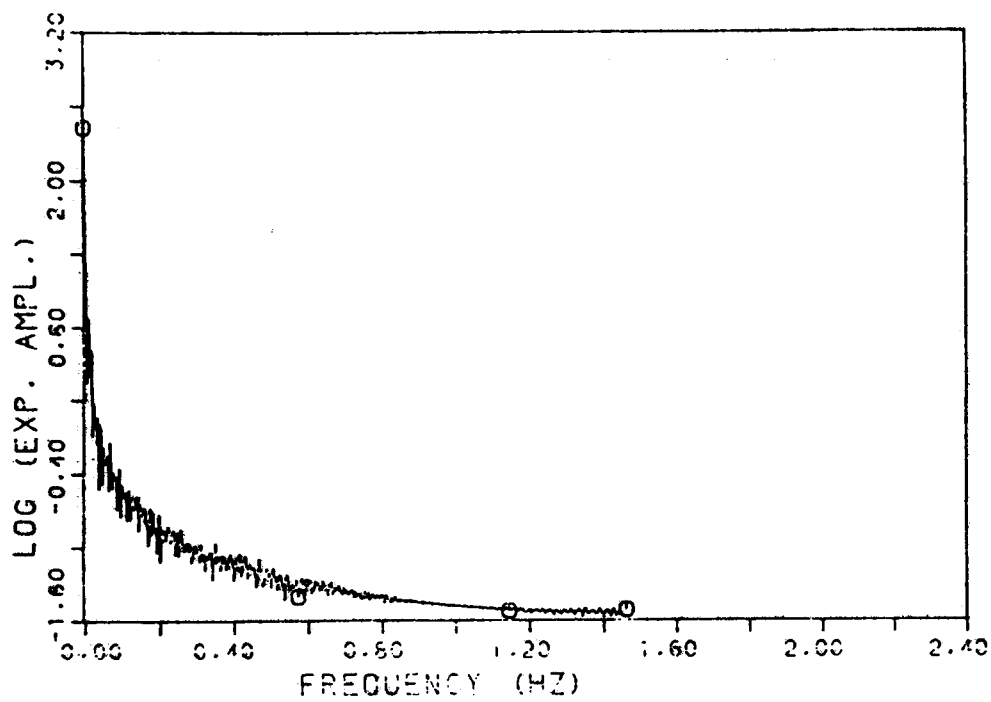


Fig. B.11 - Variable TF17 : amplitude of the FFT of the experimental trend

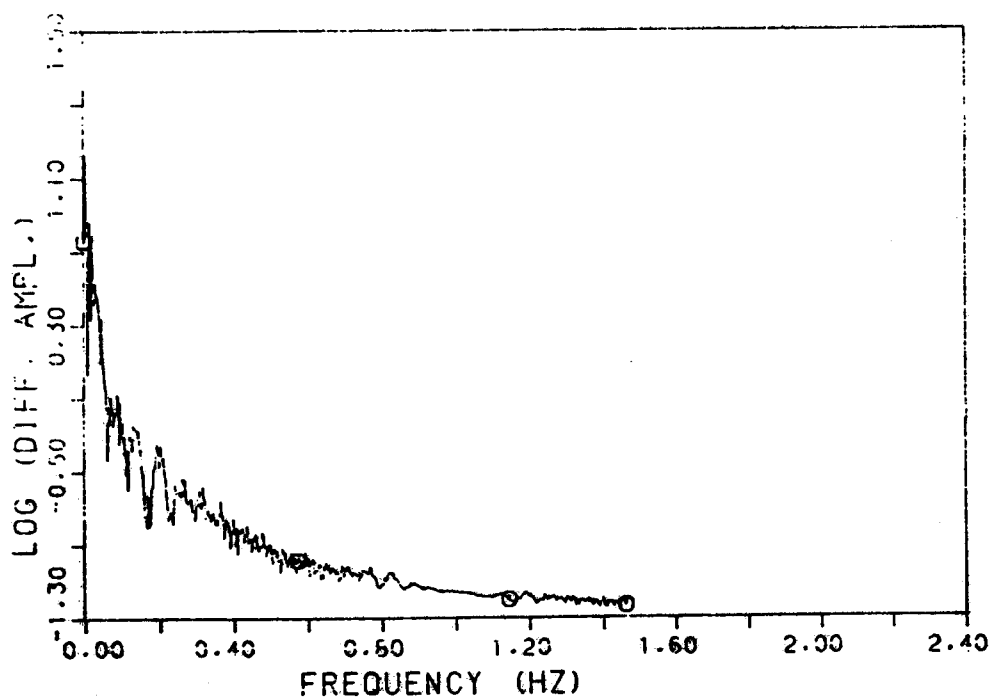


Fig. B.12 - Variable TF17 : amplitude of the FFT of the difference between calculated and experimental trends

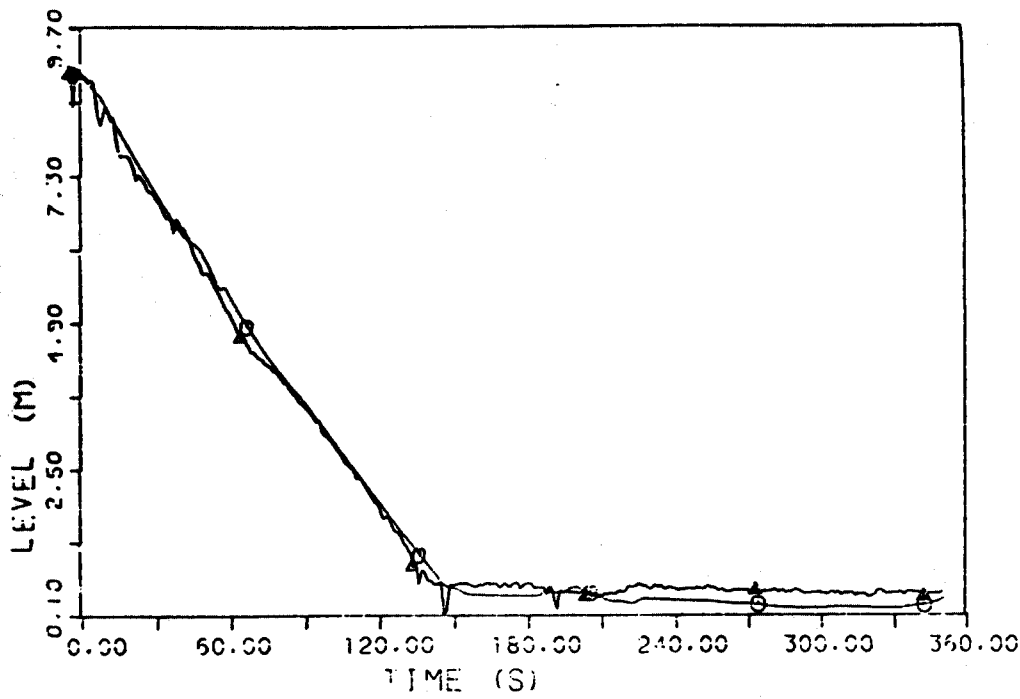


Fig. B.13 - Variable CL70 : experimental and calculated trends

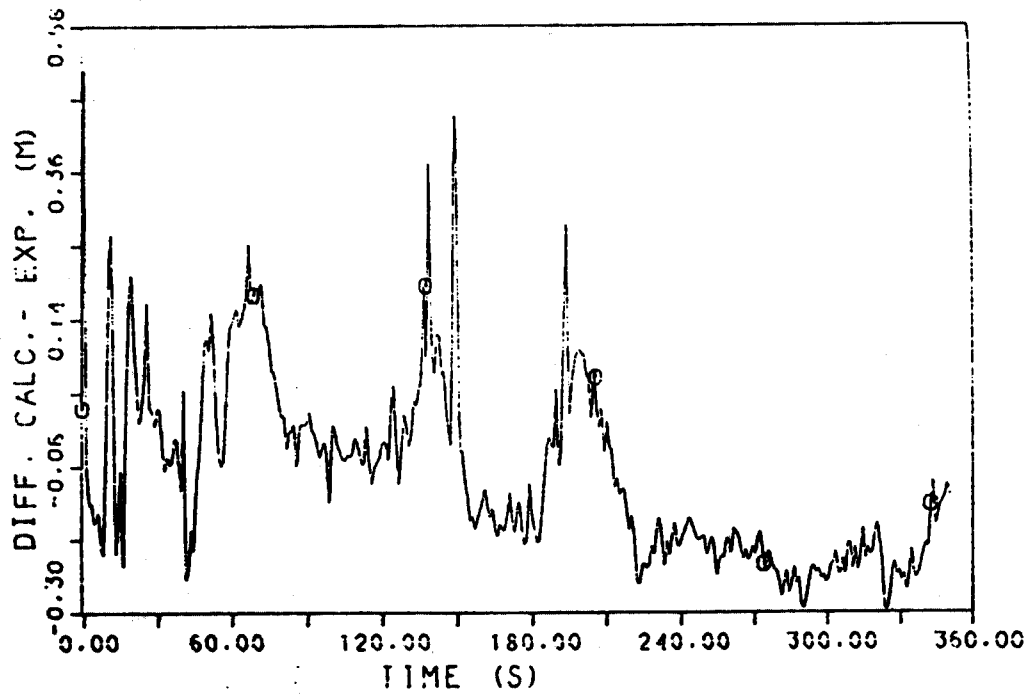


Fig. B.14 - Variable CL70 : difference between calculated and experimental trends

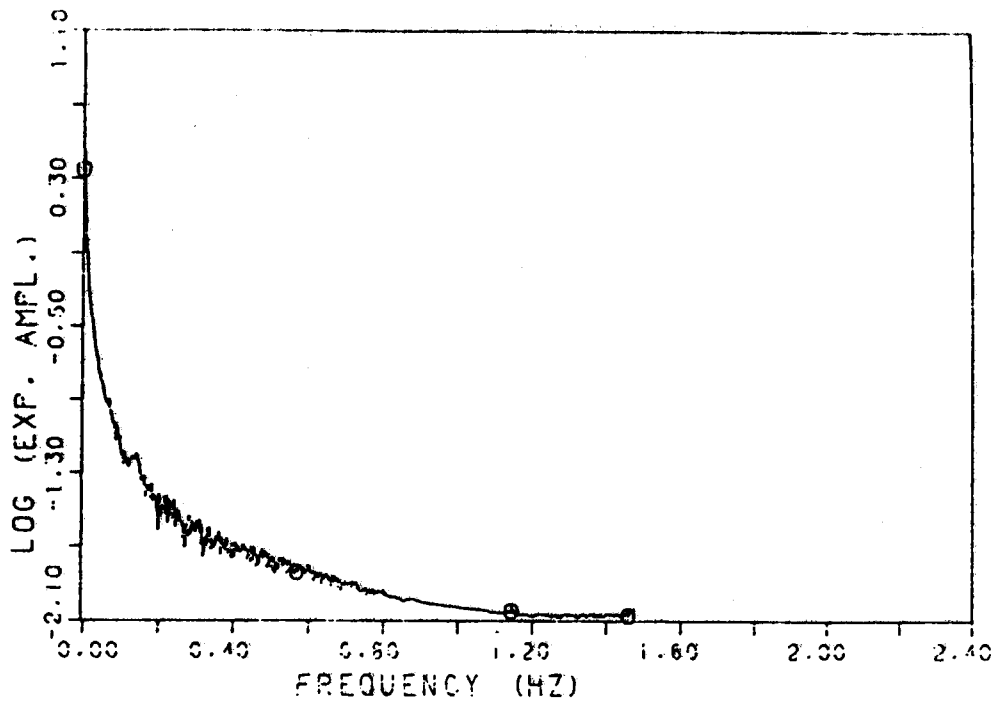


Fig. B.15 - Variable CL70 : amplitude of the FFT of the experimental trend

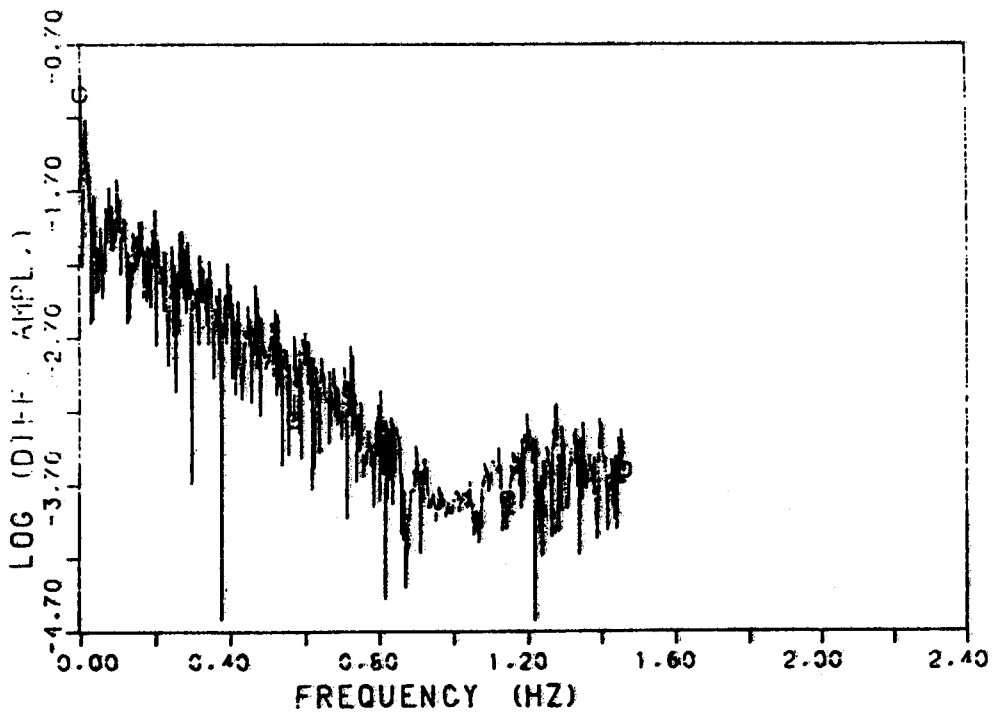
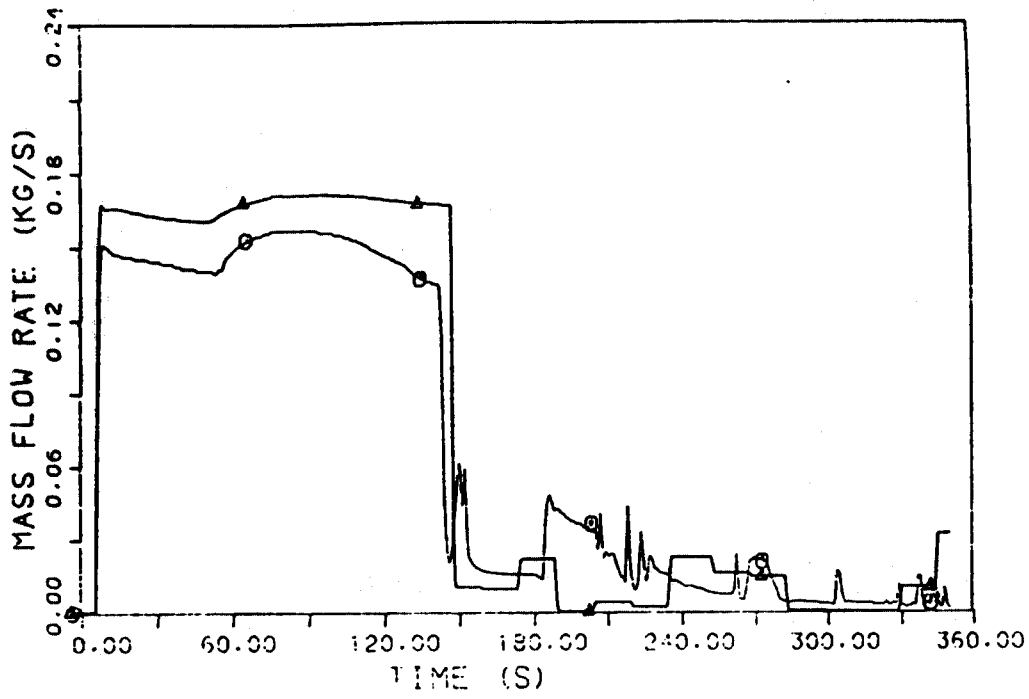


Fig. B.16 - Variable CL70 : amplitude of the FFT of the difference between calculated and experimental trends



LEGENDA
 ○DCMN RELAP5/M3D2 (P.T.)
 △EXP.

Fig. B.17 - Variable MF43 : experimental and calculated trends

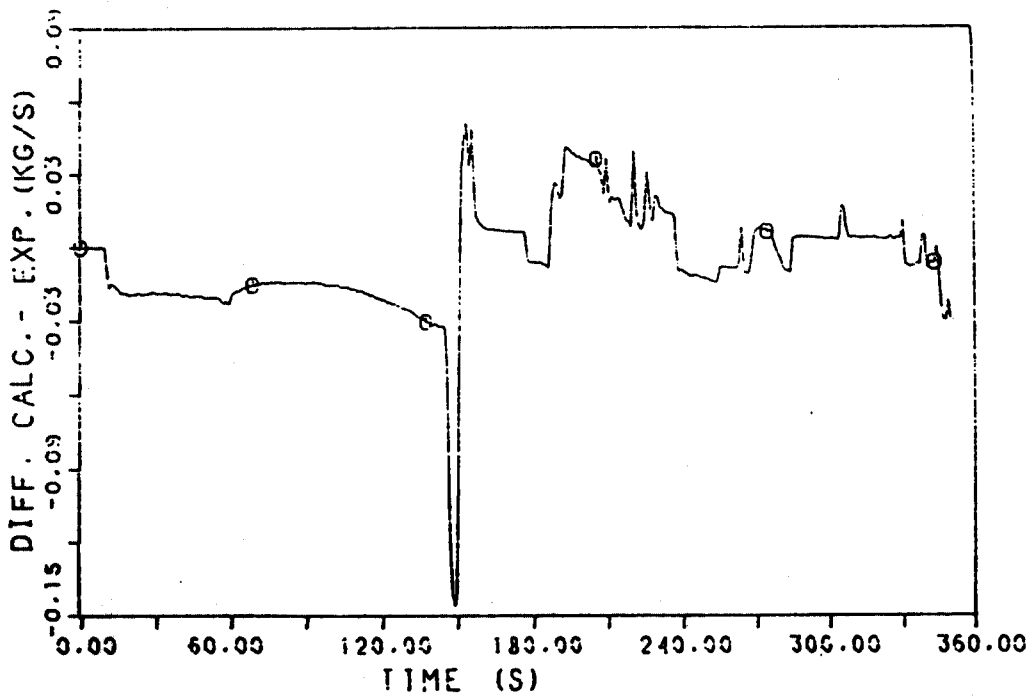


Fig. B.18 - Variable MF43 : difference between calculated and experimental trends

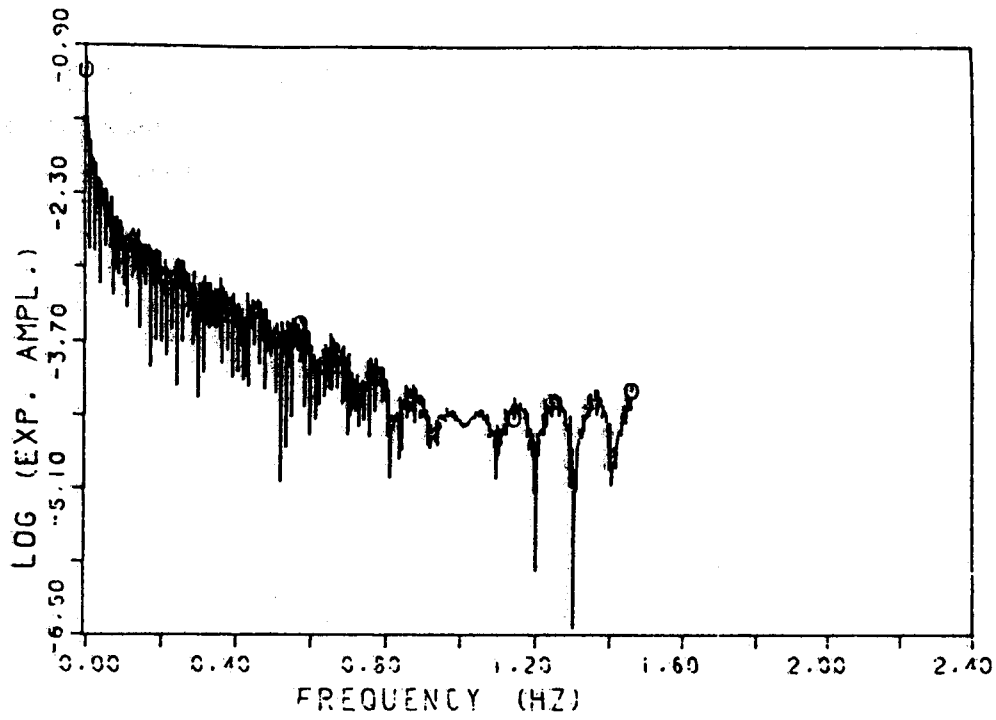


Fig. B.19 - Variable MF43 : amplitude of the FFT of the experimental trend

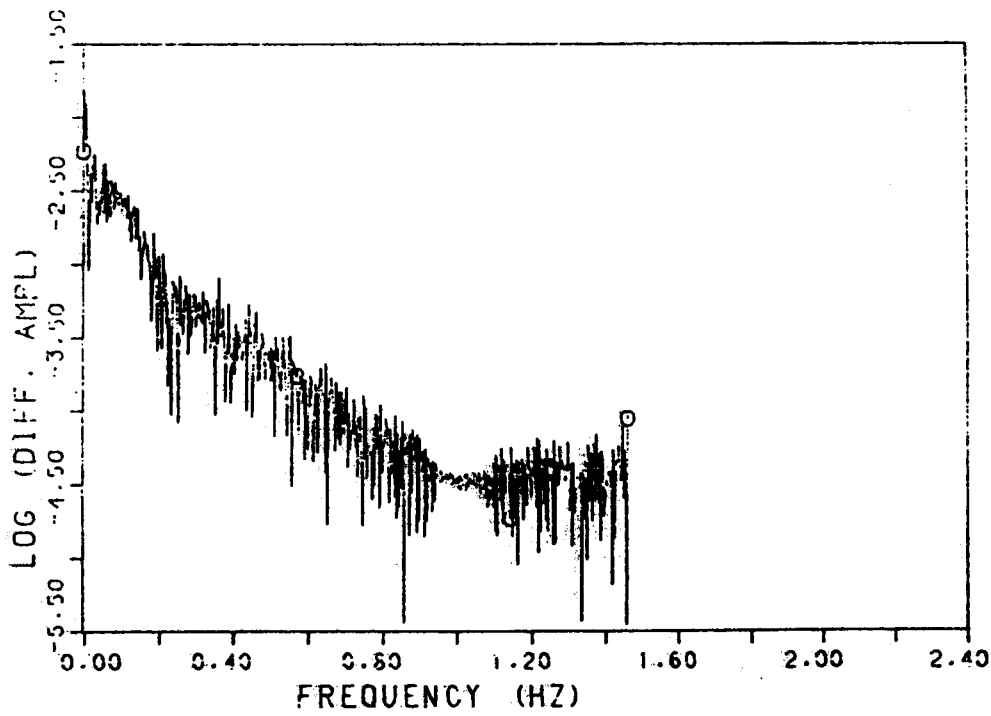


Fig. B.20 - Variable MF43 : amplitude of the FFT of the difference between calculated and experimental trends

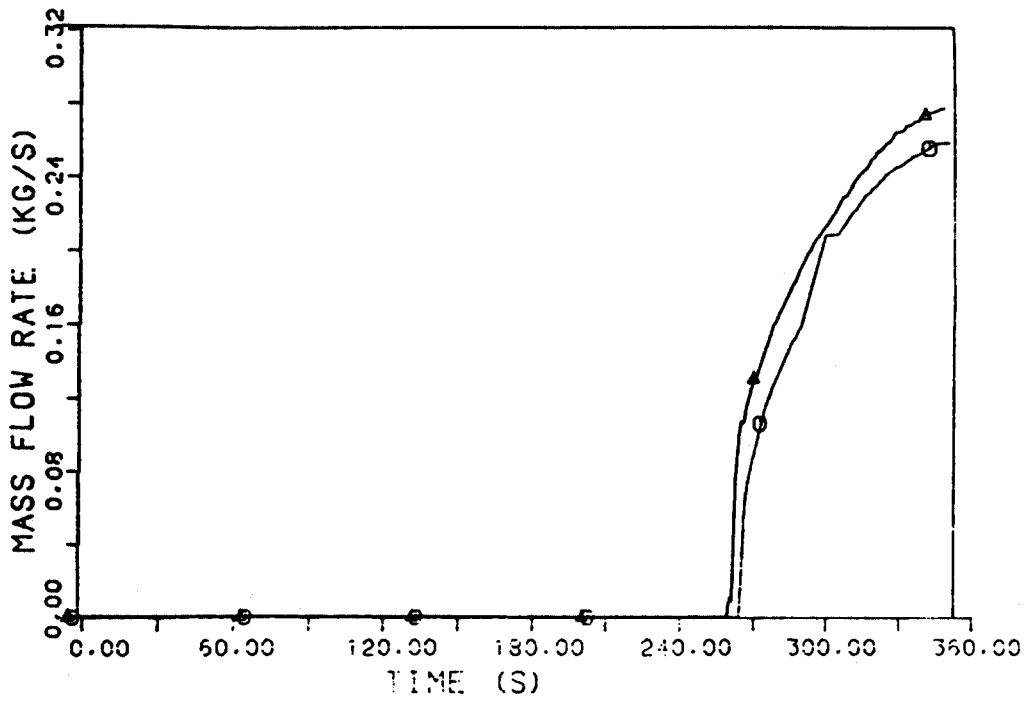


Fig. B.21 - Variable MF48 : experimental and calculated trends

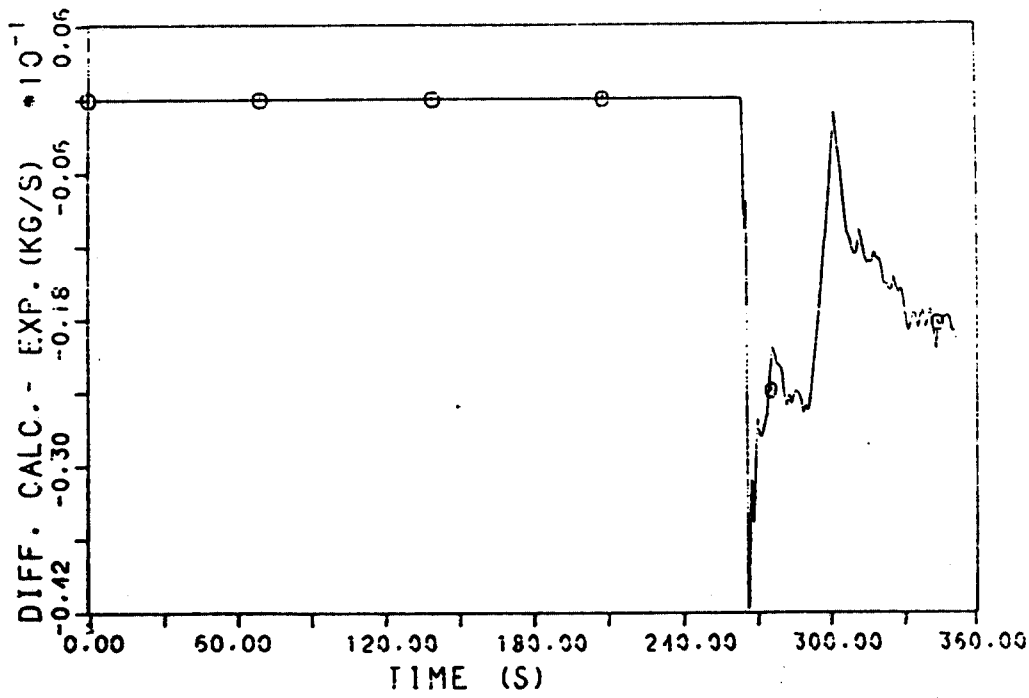


Fig. B.22 - Variable MF48 : difference between calculated and experimental trends

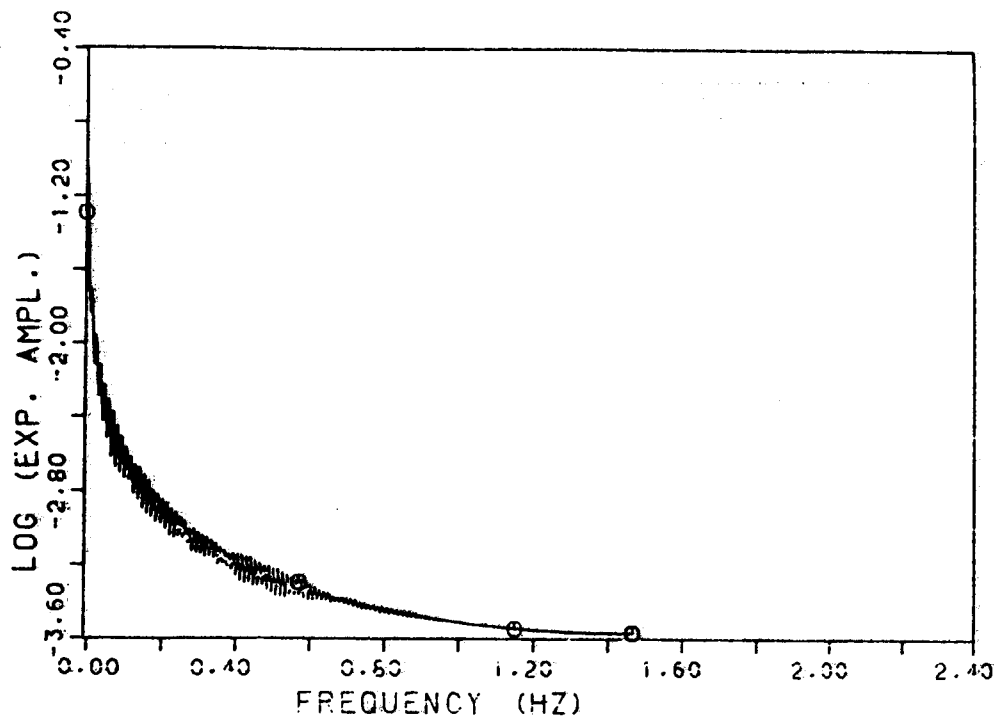


Fig. B.23 - Variable MF48 : amplitude of the FFT of the experimental trend

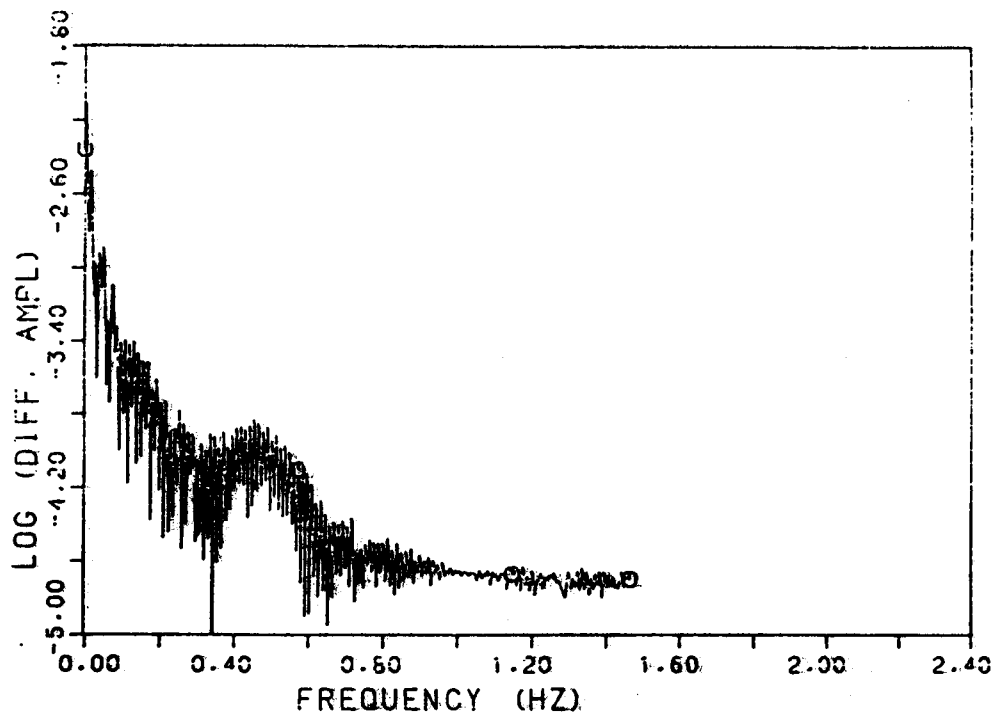
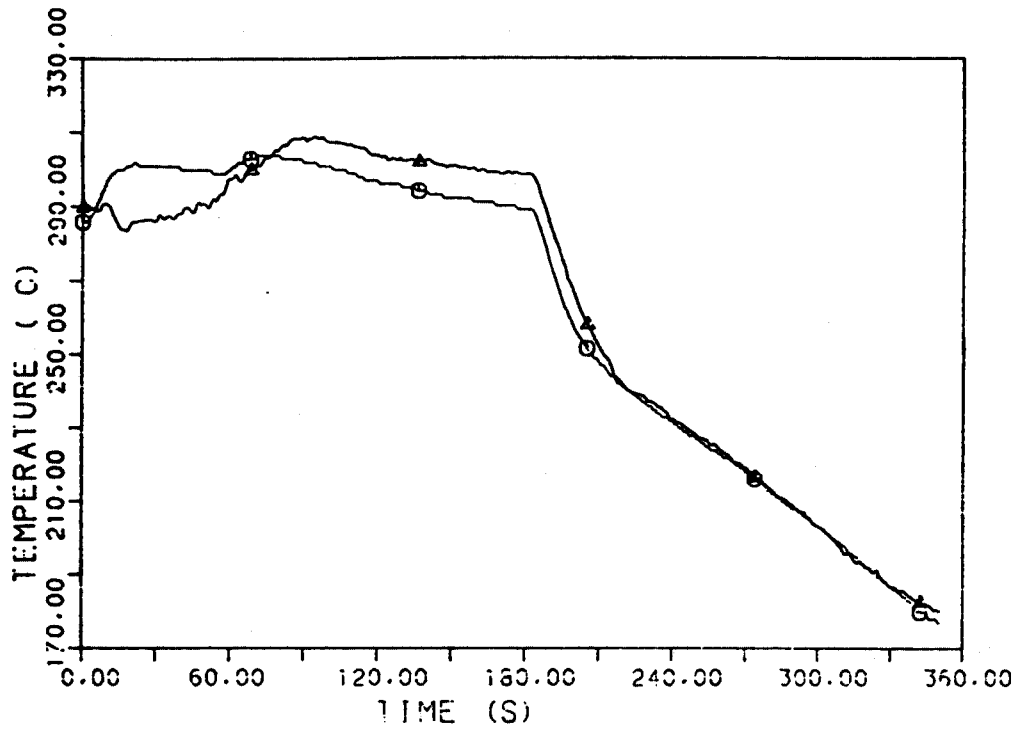


Fig. B.24 - Variable MF48 : amplitude of the FFT of the difference between calculated and experimental trends



LEGENDA
 ○DCMN RELAP5/MOD2 (P.T.)
 △EXP.

Fig. B.25 - Variable TR50 : experimental and calculated trends

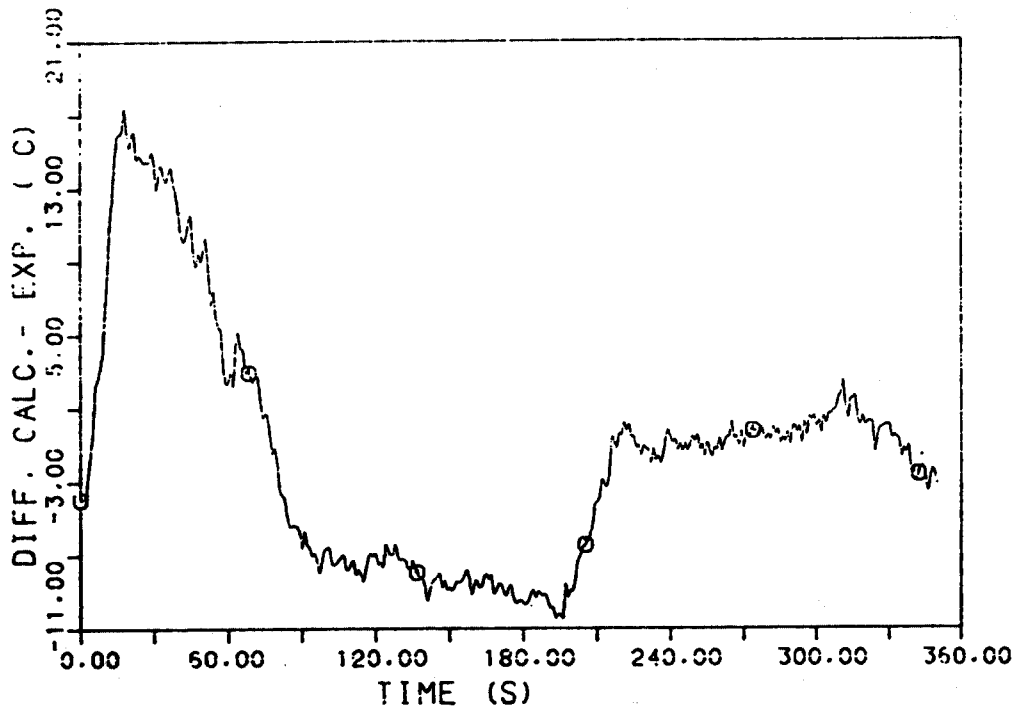


Fig. B.26 - Variable TR50 : difference between calculated and experimental trends

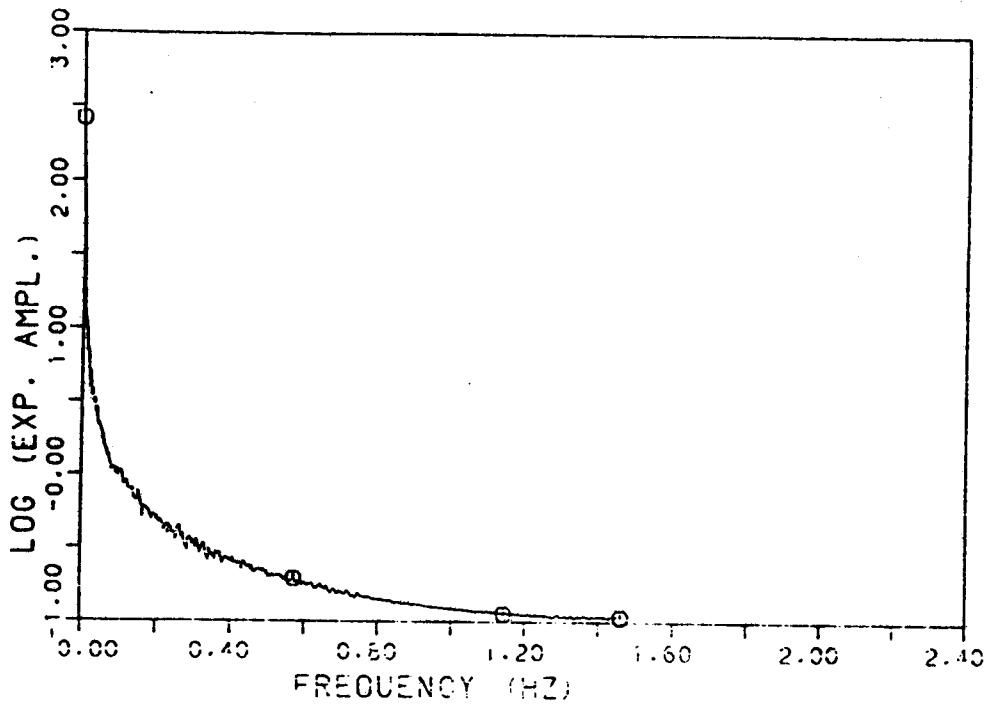


Fig. B.27 - Variable TR50 : amplitude of the FFT of the experimental trend

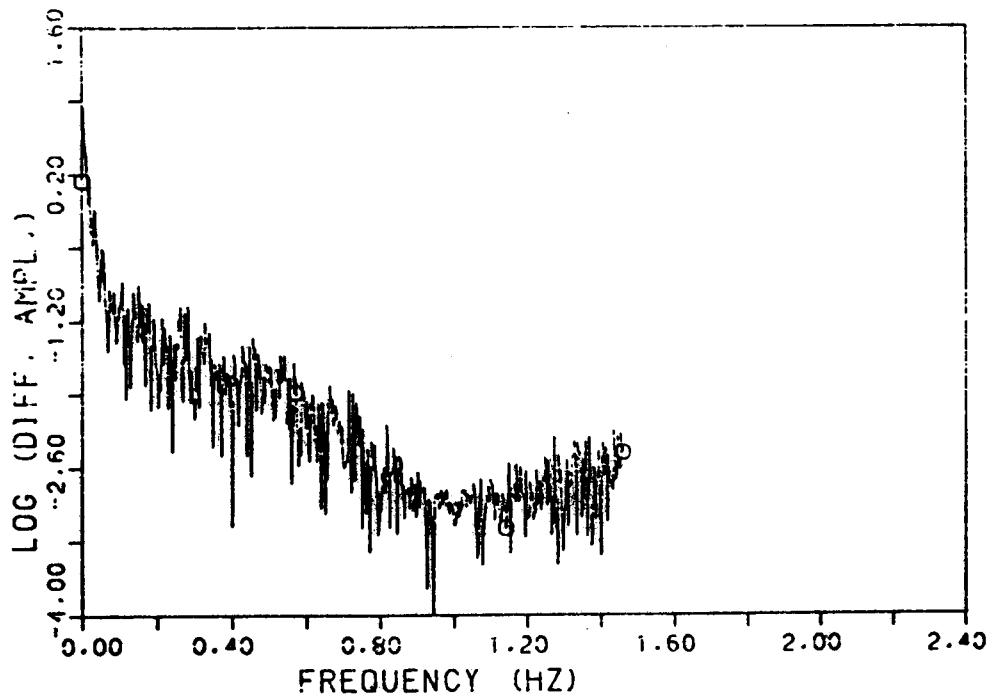
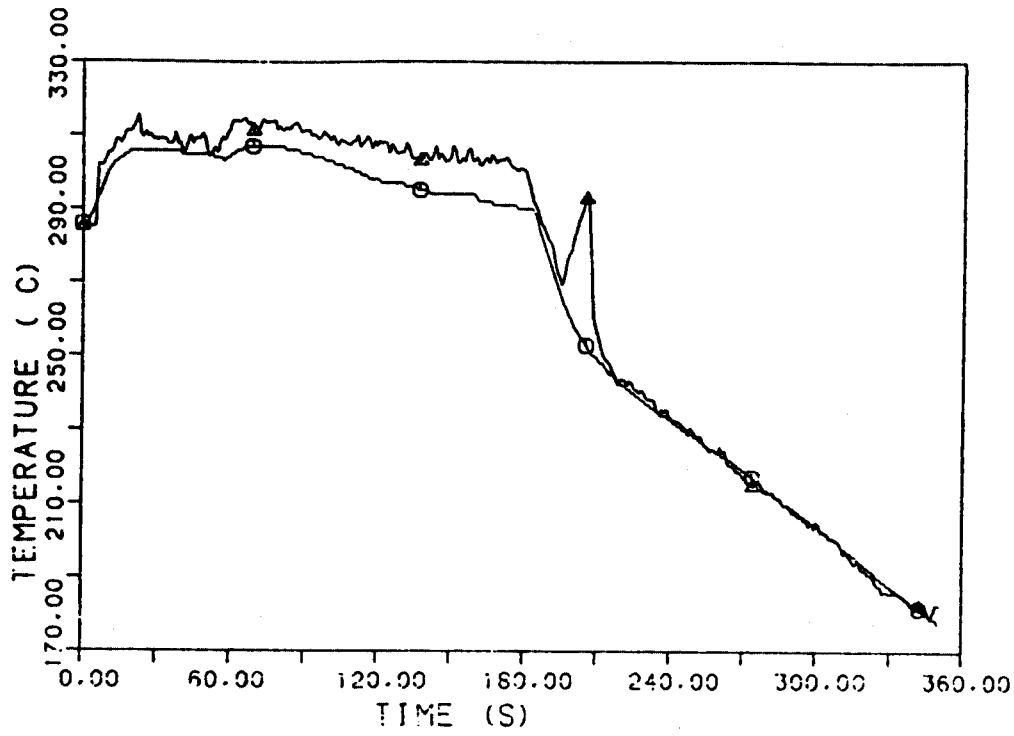


Fig. B.28 - Variable TR50 : amplitude of the FFT of the difference between calculated and experimental trends



LEGENDA
 ○ DCMN RELAP5/MOD2 (P.T.)
 △ EXP.

Fig. B.29 - Variable TR52 : experimental and calculated trends

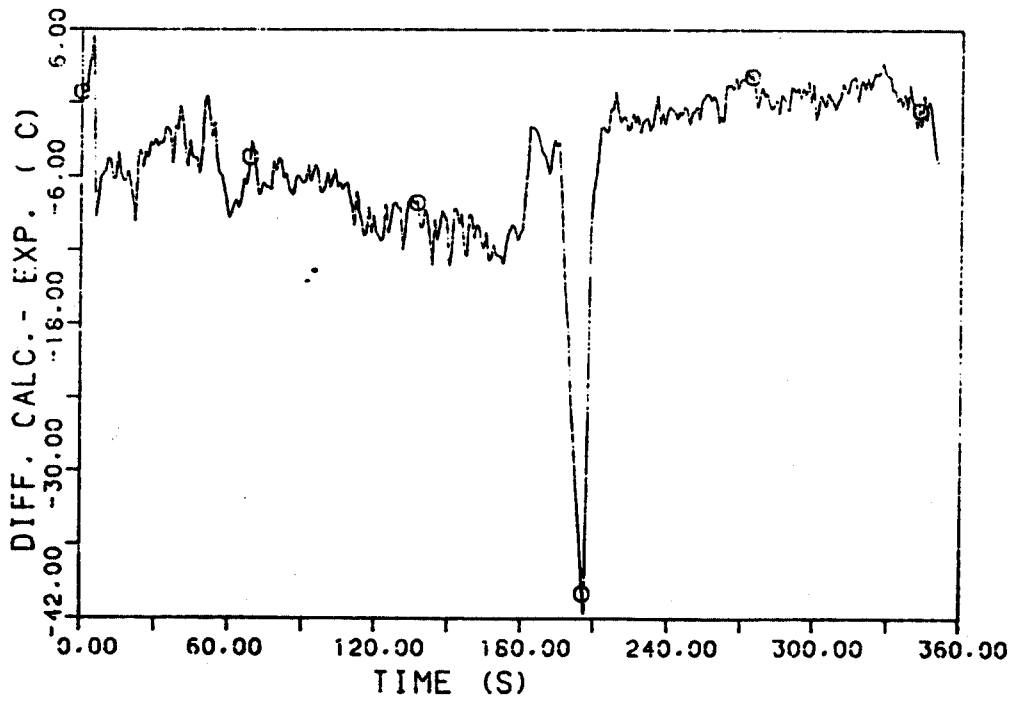


Fig. B.30 - Variable TR52 : difference between calculated and experimental trends

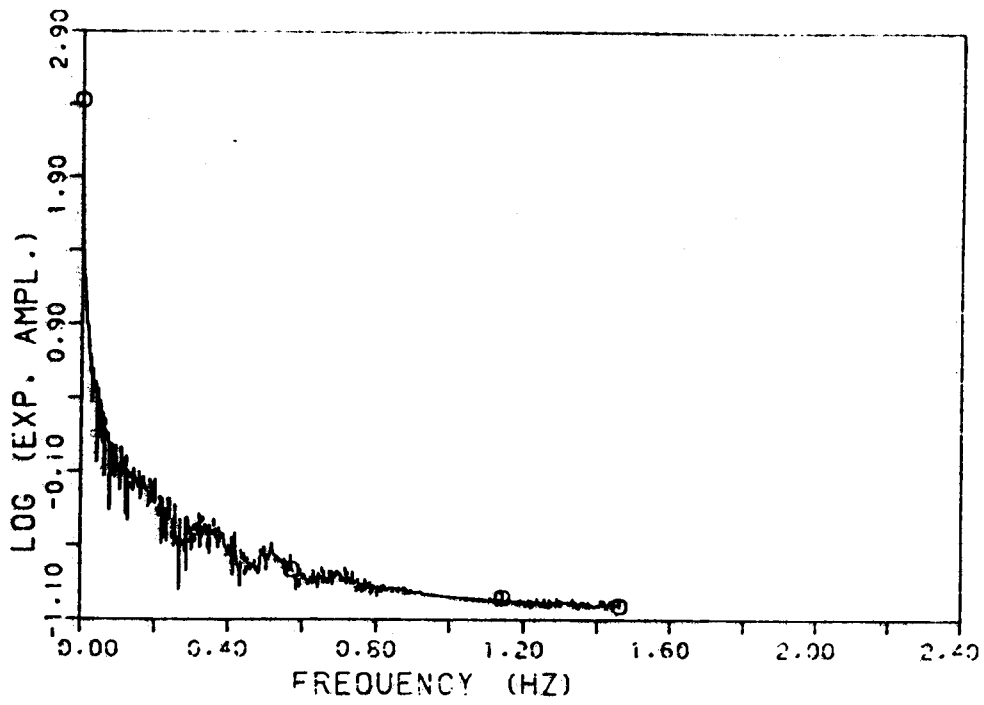


Fig. B.31 - Variable TR52 : amplitude of the FFT of the experimental trend

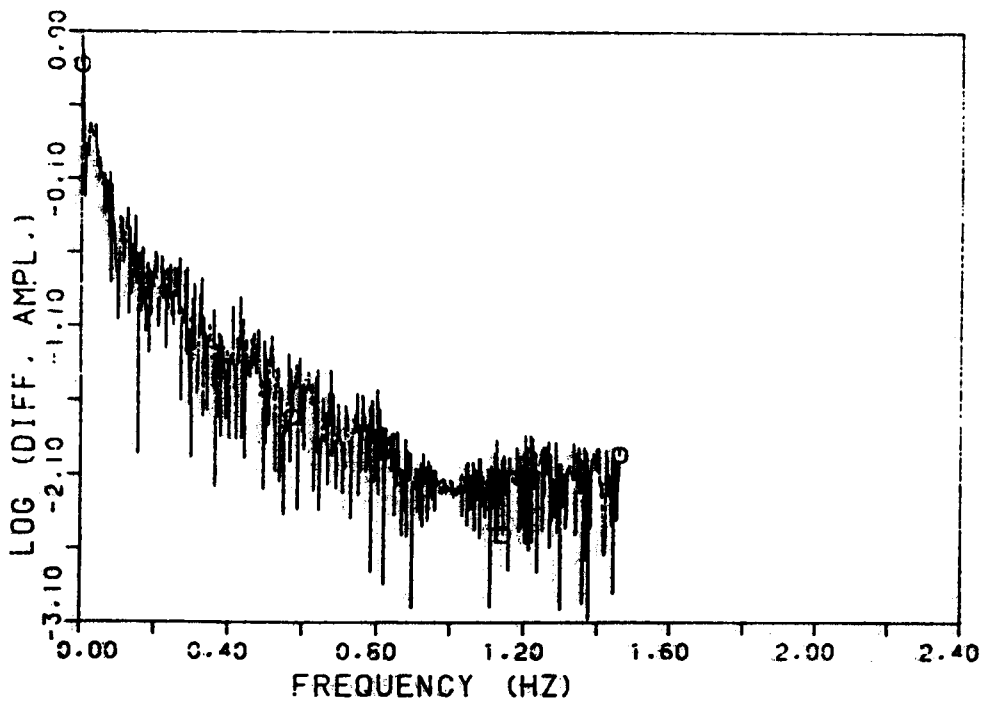
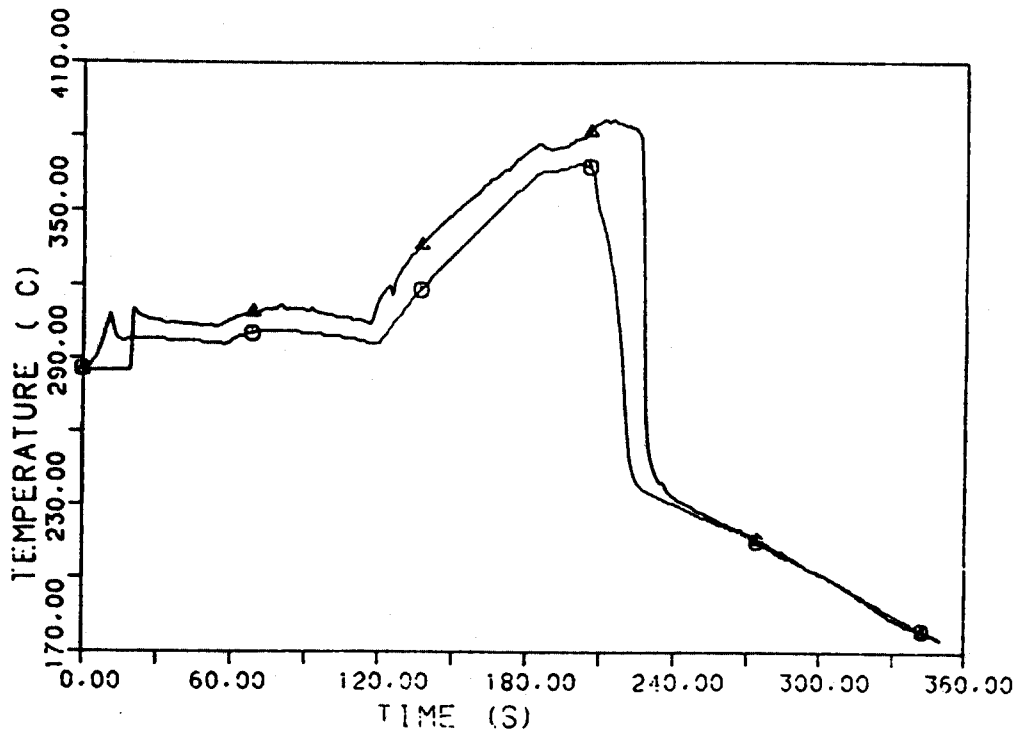


Fig. B.32 - Variable TR52 : amplitude of the FFT of the difference between calculated and experimental trends



LEGENDA
 ○DCMN RELAP5/MOD2 (P.T.)
 △EXP.

Fig. B.33 - Variable TR55 : experimental and calculated trends

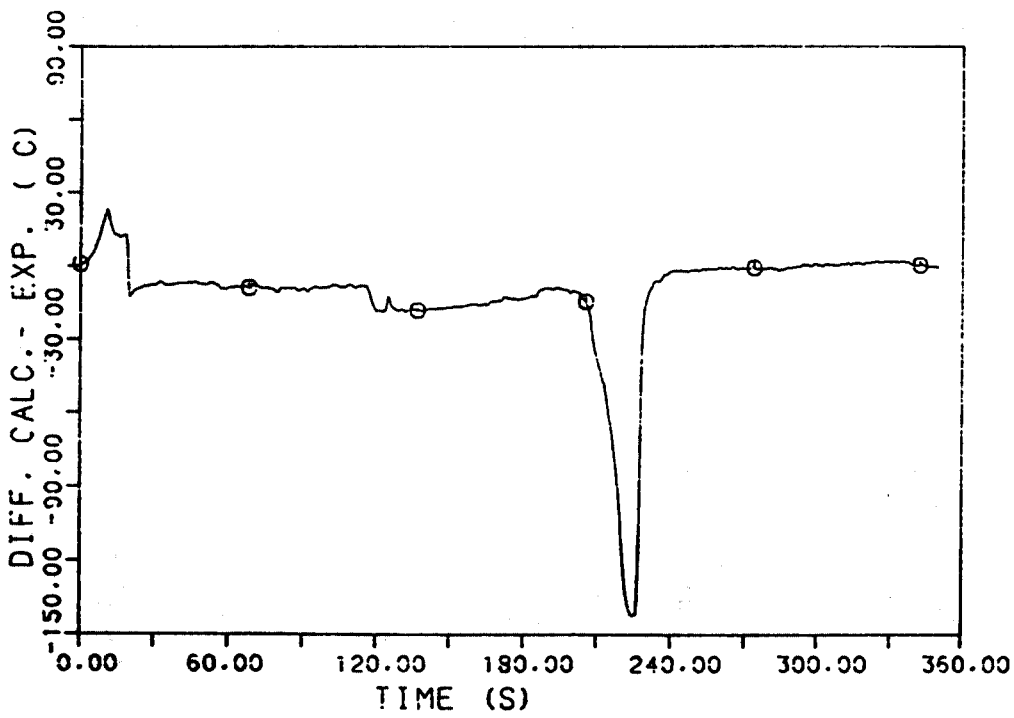


Fig. B.34 - Variable TR55 : difference between calculated and experimental trends

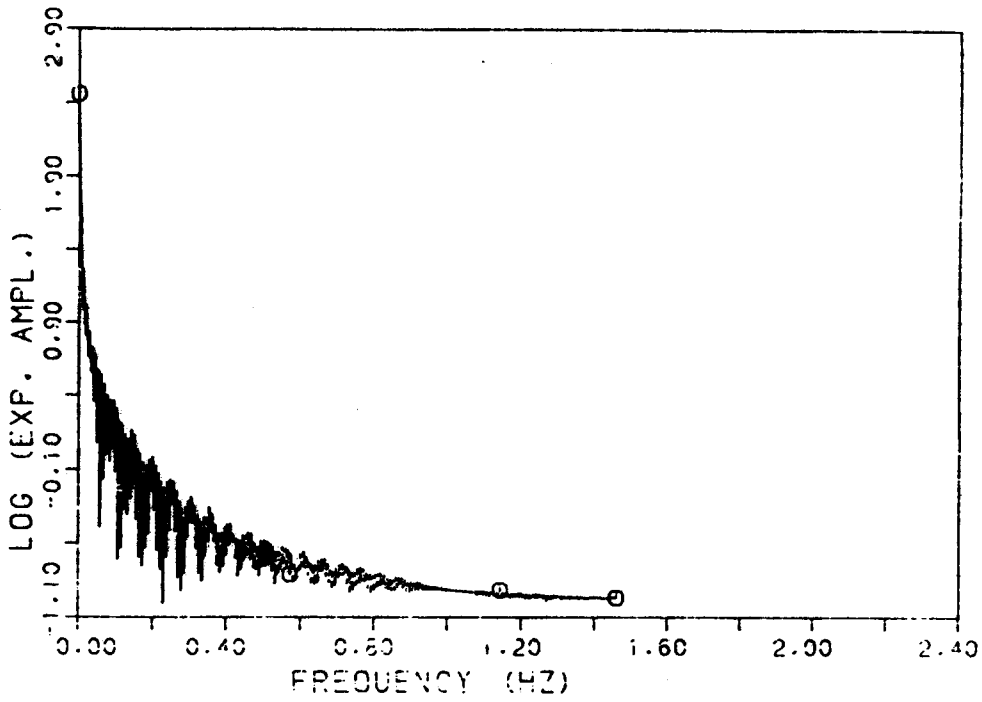


Fig. B.35 - Variable TR55 : amplitude of the FFT of the experimental trend

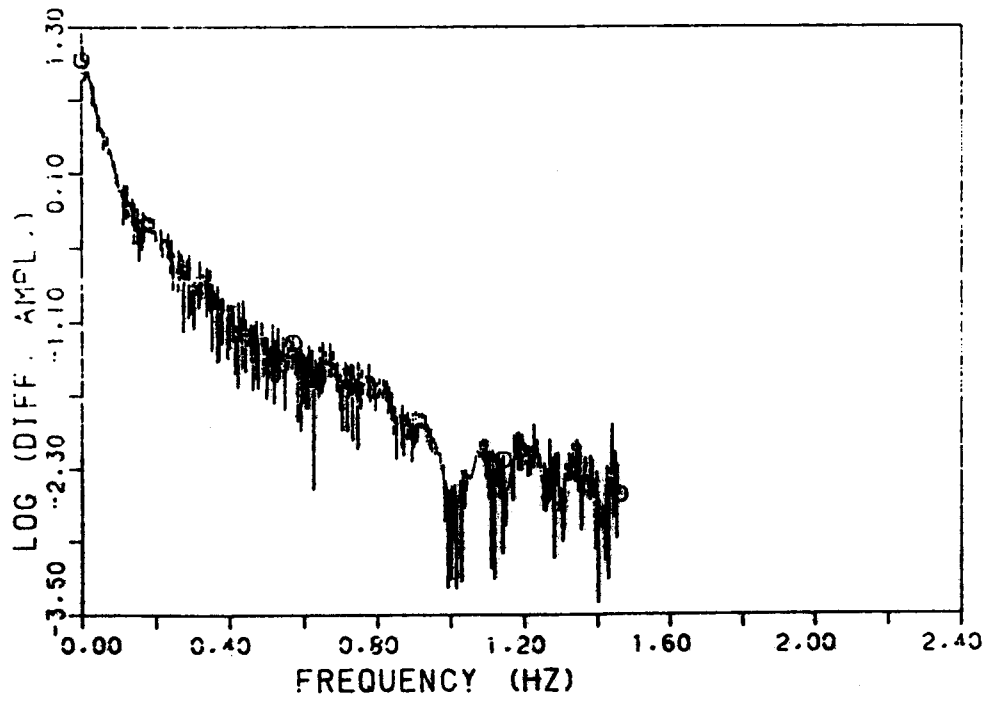
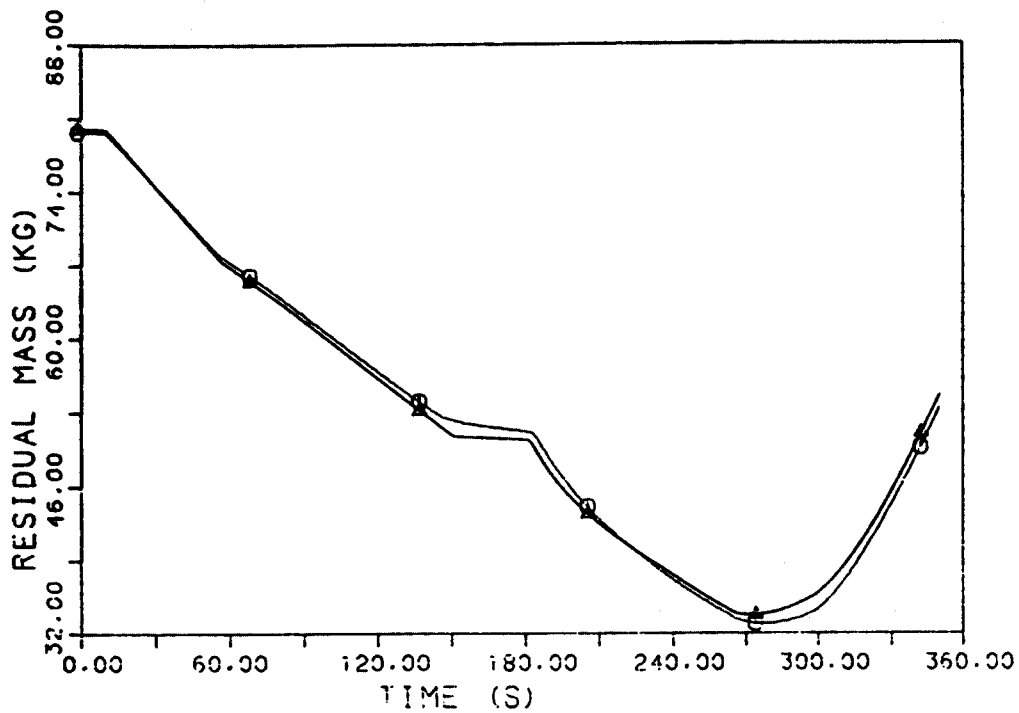


Fig. B.36 - Variable TR55 : amplitude of the FFT of the difference between calculated and experimental trends



LEGENDA
 ○DCMN RELAP5/MJD2 (P.T.)
 ▲EXP.

Fig. B.37 - Variable RM65 : experimental and calculated trends

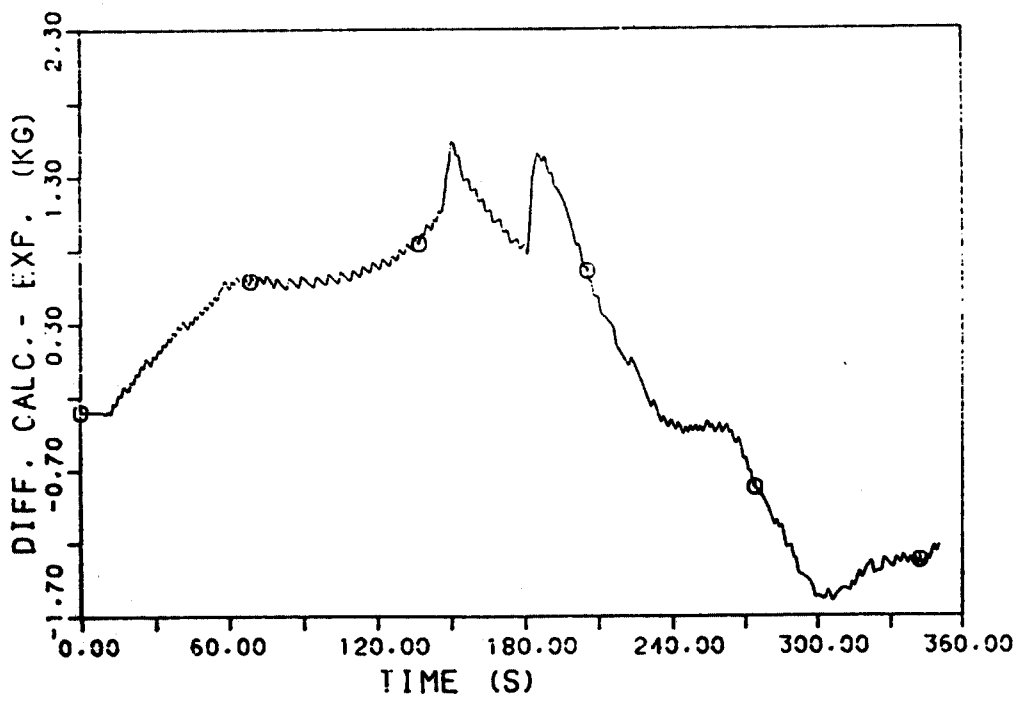


Fig. B.38 - Variable RM65 : difference between calculated and experimental trends

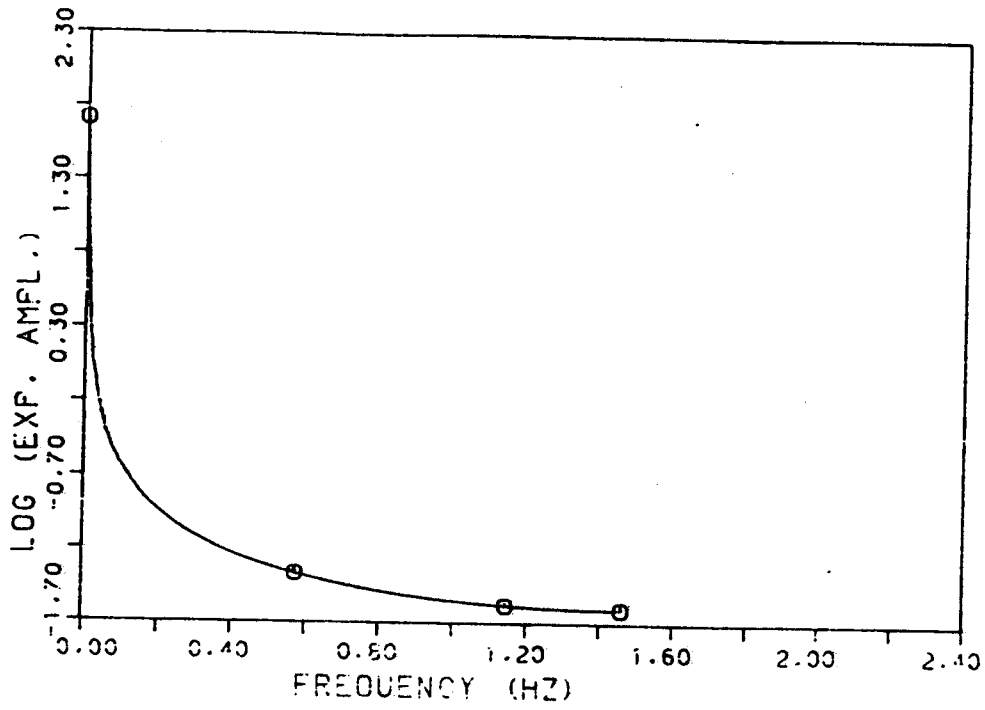


Fig. B.39 - Variable RM65 : amplitude of the FFT of the experimental trend

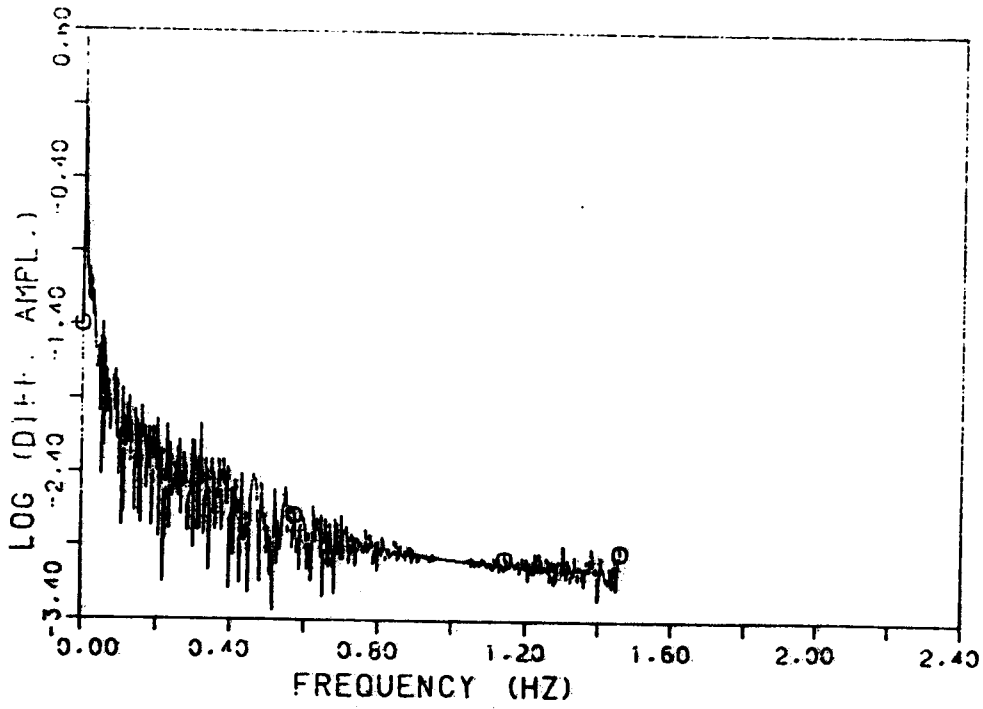


Fig. B.40 - Variable RM65 : amplitude of the FFT of the difference between calculated and experimental trends

